

ULTRAFAST DYNAMICS OF EXCITED MOLECULES PROBED USING NONLINEAR SPECTROSCOPY

by

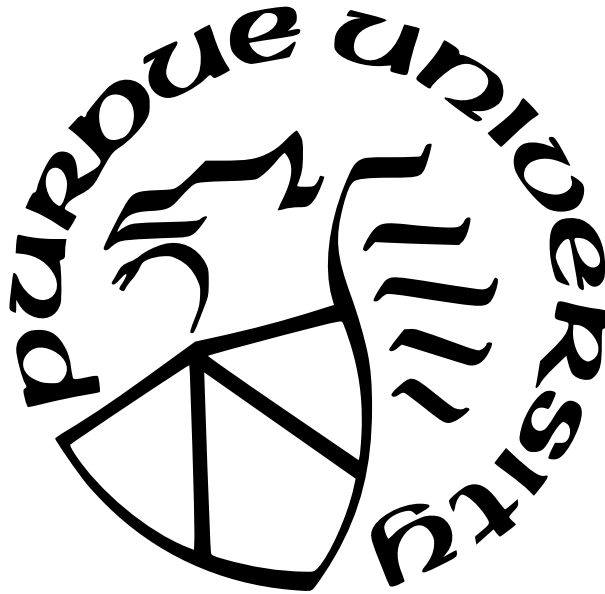
Siddhant Pandey

A Dissertation

Submitted to the Faculty of Purdue University

In Partial Fulfillment of the Requirements for the degree of

Doctor of Philosophy



Department of Physics and Astronomy

West Lafayette, Indiana

May 2024

**THE PURDUE UNIVERSITY GRADUATE SCHOOL
STATEMENT OF COMMITTEE APPROVAL**

Dr. Niranjan Shivaram

Department of Physics and Astronomy

Dr. Chris Greene

Department of Physics and Astronomy

Dr. David Koltick

Department of Physics and Astronomy

Dr. Tongcang Li

Department of Physics and Astronomy

Approved by:

Dr. Gabor Csathy

To Pushpa, Pradyumna, Sanjana & Annie

ACKNOWLEDGMENTS

This work was possible through fruitful discussions and collaborations with Francis Walz, Eric Han Liu, Joseph McGuire, Varun Makhija, Liang Tan, Loren Greenman, Xingyu Gao, Yimeng Wang, Tongcang Li, Chris Greene, David Koltick and Niranjana Shivaram.

Also, a huge shout-out to Kristin Deweese and James Corwin, for their help over the years.

I would be remiss not to acknowledge the valuable friendships of my peers Ranadeep Ghosh Dastidar, Guga Khundzakishvili, Francis Walz, C. W. Robertson, Mridul Gupta, Dimitrios Krommydas, Zachary Davis, Sameep Shah, Akhilesh Venkatesh, Kiranmayi Dixit, Soumik Chandra, Irakli Giorgadze, Sambit Banerjee, Jared Bland, Raghav Subramanian, Akhil Sheoran, Abhishek Bhaumick, Sathwik Bharadwaj, and many more.

TABLE OF CONTENTS

LIST OF TABLES	7
LIST OF FIGURES	8
ABSTRACT	13
1 ULTRAFAST TEMPORAL PHASE-RESOLVED NONLINEAR OPTICAL SPEC-	
TROSCOPY IN THE MOLECULAR FRAME	15
1.1 Introduction	15
1.2 Theoretical Background	15
1.2.1 Nonlinear Optical Response	15
1.2.2 Extraction of Molecular-Frame Response	21
1.3 Experimental Methods	28
1.3.1 Phase-resolved Nonlinear Spectroscopy	28
1.3.2 Lock-in Enabled Interferometry	30
1.4 Results and Discussion	39
1.5 Conclusions	47
2 MEASURING ULTRAFAST DYNAMICS OF VUV-EXCITED MOLECULES . .	49
2.1 Introduction	49
2.2 Theory of High-Harmonic Generation	50
2.3 Design of High-Harmonic Generation Beamline	52
2.4 Results and Discussion	60
2.4.1 VUV Transient Absorption Spectroscopy	65
2.4.2 VUV-NIR Four-Wave Mixing	70
2.5 Conclusions	74
3 ATTOSECOND SCIENCE WITH EUV ENTANGLED PHOTONS	76
3.1 Introduction	76
3.2 Generating bi-photons using $1s2s\ ^1S_0$ metastable helium	78

3.3	Excitation rates for the helium $1s2s\ ^1S_0$ state	83
3.3.1	Four-photon excitation using a 240 nm broad-band laser	85
3.3.2	Sequential excitation using helium lamp and 2059 nm laser	86
3.3.3	Four-photon excitation using SCRAP	87
3.4	Detecting attosecond entangled bi-photons	88
3.5	Conclusions	90
REFERENCES		92
A THEORETICAL CALCULATION OF EMITTED NONLINEAR E-FIELD		105
B NUMERICAL CALCULATION OF SECOND-HYPERPOLARIZABILITIES . . .		108

LIST OF TABLES

- 2.1 Magnitude of the $\gamma_{xxyy}^{(2)}$ in CO₂ for the ground and excited states, calculated using DALTON software package [94]. The values are tabulated as a function of one of the C-O bond lengths, while the other C-O bond length is kept fixed at 2.2 a.u. This corresponds to an asymmetric stretch of the molecule, with $C_{\infty v}$ symmetry. Blank cells indicate that the calculation did not converge. 63
- B.1 Calculated second-hyperpolarizability $\gamma_{zzzz}^{(2)}$ for the potassium atom [$1s^2 2s^2 2p^6 3s^2 3p^6 4s^1$], for various complete active spaces (CAS). Note how the calculated values can change drastically for different CAS. 109

LIST OF FIGURES

1.1	Magnitude of $\gamma_{xxx}^{(2)}$ as a function of the relative angle between the laser polarization and the molecules' symmetry-axis, for CO ₂ and N ₂ molecules. Their highest occupied molecular orbitals are also shown.	19
1.2	Folded BOXCARS and planar geometries of degenerate four-wave mixing (DFWM) are shown. Phase-matching dictates the direction of the emitted four-wave mixing signal. Folded BOXCARS geometry has the advantage that the emitted signal can be spatially separated from the incident laser beams.	20
1.3	Qualitative description of multiphoton Raman excitation of the ground state rotational manifold in a prototypical molecule.	22
1.4	The degree of alignment for a quantum rigid rotor is plotted for the case of a coherent excitation (orange), and an incoherent excitation (blue), when the first 10 states are excited with equal probability. Magnitude of the wavefunction corresponding to density matrix Even in this simplified toy model, only a coherent superposition of rotational states can lead to alignment. Scaling of the x-axis to physical units of time depend on the moment of inertia of the rigid rotor.	25
1.5	Transient birefringence induced by a strong NIR pump pulse, probed by a weaker NIR pulse. The amount of induced birefringence is proportional to the amount of probe light that passes through a crossed polarizer placed after the interaction.	26
1.6	A DFWM measurement in the folded BOXCARS geometry, where two of the excitation pulses are co-timed and co-polarized. The third excitation pulse is time-delayed, with a relative polarization of either 45° or 54.7° (magic angle). The intensity of the emitted signal for 45° (dashed blue) shows a slows rotational response, while for 54.7° (dashed red) the rotational nonlinearity is suppressed, and only the electronic nonlinearity is observed (see text). However, the temporal chirp of the emitted E-field (solid red/blue) is higher than its nominal value only when the bound electronic nonlinearity is non-zero, in both the cases. The chirp of the emitted signal E-field drops back to its nominal value at later times once the rotational response becomes dominant (solid blue).	28
1.7	Schematic plot, inspired by experimental data, showing (a) the total light intensity detected on the spectrometer as a function of the modulation frequency and the Fourier transform variable (ω^* canonical to angular frequency ω). Incoherent background and other 1/f noise sources form the low-frequency noise depicted near 0 Hz modulation frequency. The lineout at 200 Hz represents the LI, AC terms of equation 1.31. (a) Terms without any interference fringes ($\omega^* = 0$) are shown for 0 Hz (blue) and 200 Hz (red) modulation frequency. (b) Interference terms ($\omega^* \neq 0$) between the signal and reference (red), and the background and reference (blue). (d) Schematic of lock-in enabled imaging.	31

1.8	(a) Interference fringes between the signal and reference (red), and the background and reference (blue) are shown for two consecutive measurements. Even though the fringes drift between the two measurements, they are phase-locked relative to each other. (b) Without any drift correction, the measured heterodyne signal phase drifts between each measurement and vanishes when averaged. . . .	33
1.9	(a) Phase-locked loop (PLL) showing the chopper trace acquired by the DAQ, and the sinusoid derived from it, for subsequent phase-sensitive lock-in detection. Note how the phase of chopper drifts over time, and the PLL accounts for it. (b) Comparison between lock-in measurements, with and without information about the phase of the signal relative to the chopper. (c) Noise power spectrum of the CMOS camera, with and without balancing. The noise floor of the balanced detection is 30% lower than that of the unbalanced detection.	34
1.10	The alignment Pump, Probe and Gate beams are focused into a gas cell, and the emitted N-DFWM signal is spatially isolated after the interaction. It is combined with the external reference in a lock-in detection enabled spectrometer. The Reference is separately characterized using a FROG device (not shown here). . .	35
1.11	Measured signal E-field (amplitude and phase) at three different pump-probe time delays. (a) At negative time delay, the pulse is positively chirped. (b) At pump-probe overlap, the intense pump pulse causes ionization, leading to a negatively chirped signal pulse. (c) At $\tau = 4.26$ ps, when the molecule is anti-aligned, the chirp is lowered.	37
1.12	Schematic of the experimental setup. The alignment Pump and the time-delayed DFWM Probe beams are focused into a gas cell containing the target gas at room temperature and a pressure of 4 bar. The emitted nonlinear signal is spatially isolated, cleaned with a polarizer, and combined with the external reference in a lock-in detection enabled spectrometer. The Reference is separately characterized using a FROG device (not shown).	40
1.13	Calculated $\langle \cos^2(\theta) \rangle$ of the rotational wavepacket for CO ₂ and N ₂ molecules. The calculation is done using experimentally determined parameters, and the rotational constants of the molecules available in the literature.	41
1.14	(a) Temporal phase of the nonlinear signal E-field from pre-aligned N ₂ molecules and (b) from pre-aligned CO ₂ molecules, as a function of pulse time (t) and time delay (T). (c) A representative plot of E-field amplitude and phase along with a polynomial fit of the phase. (d) For each pump-probe time delay T, the measured E-field phase is fit with a polynomial in pulse time t. The second-order fit coefficient (chirp) is plotted as a function of T for N ₂ and CO ₂ . The error band represents standard error. The chirp of the input probe pulses is 0.00017 fs^{-2}	42

1.15	(a) Alignment angle-dependent molecular-frame nonlinear signal E-field chirp retrieved from the experimental data, for N ₂ and CO ₂ . (b) Theoretical calculations of the alignment angle-dependent E-field chirp for N ₂ and CO ₂ . (c) alignment angle-dependent molecular-frame E-field amplitude (pulse time-integrated). (d) same as (c) from theoretical calculations. Highest occupied molecular orbitals (HOMO) for N ₂ and CO ₂ molecules, showing their distinct σ and π bonding character, respectively, are shown in the bottom panel for reference. While the molecular frame chirp does not directly correspond to the shape of the HOMOs, the chirp is seen to be distinctly different for the two molecules.	43
1.16	Representation of the Monte Carlo uncertainty analysis: For each delay step, the mean and standard error of the experimental data (chirp or integrated amplitude) is used to generate random noisy instances of the T-dependent data. These instances are fit individually, and the retrieved angle-dependence from all these fits are used to generate the mean and uncertainty of the angle-dependence. . .	45
2.1	UV/Visible spectra showing the resonant wavelengths for a few molecular transitions. Note how some of the most common molecules need vacuum-ultraviolet light for optical excitation.	49
2.2	Trajectories of electrons after tunneling out of the parent atom. Dotted curves represent trajectories that result in recombination with the parent ion and subsequent HHG, while solid curves show trajectories that do not. A full cycle of the drive laser electric field (red) is superposed.	51
2.3	Schematic of an attosecond pulse train generated during high-harmonic generation. The radiation is emitted when the accelerated electron recombines with the parent ion, which happens near a zero-crossing of the drive laser electric field. .	52
2.4	(a) Schematic of the HHG beamline. 35 fs wide pulses at a wavelength of 810 nm are derived from a Ti:Sapphire laser amplifier system and focused into an argon gas cell in the first vacuum chamber. The design of the gas cell is shown in (b). In the second vacuum chamber the generated HHG radiation is isolated from the NIR drive using an aperture and special mirrors. Additional NIR beams are combined with the HHG beam, and focused onto the target in the third vacuum chamber. After interaction the HHG beam travels to the last vacuum chamber, where it is dispersed on an X-ray CCD camera using a diffraction grating. The NIR beams are out-coupled from vacuum, and measured using a spectrometer. .	53
2.5	Intensity profile of the annular drive beam at the image plane (black) and 200 mm before/after the image plane (red). As a result of diffraction, the central part of the beam starts to gain intensity away from the image plane, making it essential to place the aperture close to the image plane, for optimally rejecting the drive laser.	54
2.6	Pictures of the argon gas cell, with 0.002" Kapton windows, that are drilled through by the drive beam. Rubber o-rings are used to seal the Kapton windows. The cell is 1" long, and can hold gas at up to 150 torr of differential pressure. .	54

2.7	VUV and UV harmonic yield as a function of backing pressure in the argon gas cell. The yield reaches a maximum value, after which propagation effects start to affect yield.	55
2.8	VUV and UV harmonic yield as a function of the position of the argon gas cell, relative to the focus of the drive beam. There are two distinct maxima, for when the focus of the drive is either upstream or downstream of the gas cell centre. We use the -25 mm position, to avoid possible drive pulse distortion before harmonic generation occurs.	56
2.9	Multilayer dielectric mirror that selectively reflects 5 th -harmonic, and transmits other frequencies, showing damage from prolonged UV/IR irradiation.	57
2.10	Frequency-dependent reflectivity of bare Nickel for 5° angle of incidence. The reflectivity is even higher for smaller incidence angles.	58
2.11	Frosted YAG crystal used for spatially overlapping the VUV and NIR beams in the focus. Inset shows fluorescence from the focal spot of the 5 th -harmonic beam.	58
2.12	(a) Target gas cell with thin Kapton windows. (b) Two custom-made vacuum feed-throughs consisting of two $\frac{1}{2}$ inch quick-connect couplings welded on either side of KF flanges.	59
2.13	Calibrated 5 th -harmonic spectrum, as a function of (a) wavelength, and (b) energy. The center wavelength (energy) of the harmonic is about 162 nm (7.66 eV).	61
2.14	Schematic of a 1-dimensional conical intersection (CI) between two potential energy surfaces. When a wavepacket traveling on the higher-lying state traverses the CI, part of the wavepacket can disperse onto the lower-lying state, leading to radiation-less decay.	64
2.15	Timing diagram of transient absorption spectroscopy (TAS). The NIR beam is blocked/unblocked using an optical chopper, and consecutive NIR ON and NIR OFF frames are recorded using an X-ray CCD triggered by the chopper edge.	65
2.16	(b) VUV transient absorption (TA) spectrum, in CO ₂ , around VUV-NIR temporal overlap. About zero time delay, the absorption maximum shifts from 7.6 eV to 7.73 eV. (a) Time delay-dependent cuts at 7.6 eV and 7.73 eV.	67
2.17	(c) VUV transient absorption (TA) spectrum around the half revival in CO ₂ . (a) Calculated degree of alignment. The molecule is aligned along the VUV polarization when $\langle \cos^2\theta \rangle > 0.33$, and anti-aligned when $\langle \cos^2\theta \rangle < 0.33$. (b) Time delay-dependent cut at 7.73 eV showing that the absorption is maximized (minimized) when the molecule is aligned (anti-aligned) to VUV polarization. The cut at 7.6 eV shows the opposite trend.	69
2.18	(a) Measured absorption cross-section of CO ₂ from references [103], [104]. Raw data was retrieved from www.cfa.harvard.edu/amp/ampdata/co296/co2.html . (b) Schematic of a non-vertical transition from a linear to a bent CO ₂ geometry.	70

2.19	(a) Example of a possible VUV-NIR four-wave mixing scheme, where the emitted E-field is NIR. (b) Double-sided Feynman diagrams illustrating a Stokes and an Anti-Stokes pathway for signal emission. The VUV fields create a broadband coherence, which is then probed by the NIR field. (c) Energy level diagrams for the quantum pathways shown in (b). To emit signal in the NIR, the target molecule must be left in an excited state, making such an experiment non-parametric.	72
2.20	Four-wave mixing experiment in bulk MgO crystal (500 um thick). The harmonic pump beam consists of 810 nm + 270 nm + 162 nm, and the probe is NIR (810 nm). The measured signal intensity shows distinct features near the expected arrival times of the 3 rd - and 5 th -harmonic. The dominant peak at zero time delay is attributed to an interaction between the probe and the residual NIR leakage of the drive.	73
3.1	One-photon decay rates for the DC Stark-shifted $2S_{1/2}$ state with $m_F = 0, \pm 1$, as a function of the applied electric field. The Stark-shifted states are labelled using the $\left \left[(L S) J I \right] F m_F \right\rangle$ convention. The two-photon decay rate of the unperturbed $2S_{1/2}$ state is also shown for comparison. Since the one-photon decay rate of the $2P_{1/2}$ and $2P_{3/2}$ states is $6 \times 10^8 s^{-1}$, even a small amount of mixing quenches the metastable $2S_{1/2}$ state.	82
3.2	(a) Generation of bi-photons in the EUV via two-photon decay of the $1s2s \ ^1S_0$ state excited by four-photon excitation using a broad band 240 nm laser. (b) Two-step sequential excitation of the $1s2s$ state via the $1s2p$ state using a high photon flux helium lamp and a 2059 nm coupling laser. (c) The SCRAP technique to populate the $1s2s$ state using a multiphoton pump pulse and a Stark shifting pulse which enable rapid adiabatic passage and ionization suppression by LICS (LICS not shown). The estimated bi-photon generation rate is also shown for each scheme in (a) - (c). (d) Proposed experimental scheme to generate EUV entangled photons and utilize them in an attosecond pump-probe photoionization experiment. (e) An attosecond pump-probe photoionization scheme in molecules using bi-photons.	84
3.3	Coincidence-to-accidental ratio (CAR), as a function of detection window τ , for various bi-photon excitation rates. CAR measures the number of true coincidence counts, compared to the number of background coincidence counts, and is a form of SNR.	90
B.1	Flowchart showing the order of steps for calculating excited-state properties in DALTON, using MCSCF.	109

ABSTRACT

Some of the simplest molecules that are found in abundance in nature, like oxygen, nitrogen, carbon dioxide and water can be playgrounds for complex quantum mechanical phenomenon. Although we can calculate their static properties, like binding energies, equilibrium geometries and ionization/decay rates with extraordinary precision, their dynamics offer new avenues for exploration. Although analytical techniques have been successfully applied in studying single-particle and many-particle systems, few-particle systems like simple molecules are still best understood through a combination of numerical calculations and experimental work [1]. However, the small size of these molecules endows them with dynamics that occur on timescales of a few picoseconds to a few attoseconds, making their experimental study challenging. The overarching goal of this work is the study of such ultrafast dynamics in excited state molecules/atoms, by developing and demonstrating novel optical probes of quantum dynamics.

One way to probe ultrafast dynamics in molecules is by measuring their nonlinear optical response. Such a measurement can potentially track the evolution of the symmetries of excited molecules, shedding light on their transient dynamics. We start chapter 1 with a brief discussion of the formalism behind nonlinear optical spectroscopy. Direct measurement of ultrafast (and ultraweak) optical pulses is discussed as a useful probe of nonlinear processes. After presenting preliminary results on direct electric field reconstruction, experimental work on measuring emitted nonlinear electric fields from impulsively aligned molecules is discussed. In such an experiment, however, contributions from both aligned and unaligned molecules are present, and new experimental capabilities had to be developed to disentangle and measure the ultraweak signal from aligned molecules. Following a detailed discussion of the developed measurement capabilities, results from experiments done on aligned carbon dioxide and nitrogen molecules are discussed.

Unlike solids, where electronic states can be excited with visible/UV light, binding energies in isolated atoms/molecules are on the order of electron-volts (eVs), and they need vacuum-ultraviolet (VUV) extreme-ultraviolet (EUV) light to excite electronically. Polyatomic molecules, like ethylene, when excited to an electronic state with VUV light, often

relax back to the ground state by redistributing energy to their internal degrees of freedom non-adiabatically. These relaxation pathways are important in many chemical and biological systems, and control the yield of chemical reactions ranging from elementary reactions involving few atoms to large biomolecules such as DNA and proteins. For instance, in the photochemical reaction of the protein Rhodopsin, considered to be the primary event in human vision. In chapter 2 we discuss progress made towards extending nonlinear response measurements to study ultrafast dynamics in electronically excited molecules, using a high-harmonic VUV source. Details about the design of the high-harmonic generation beamline, and preliminary experimental data are presented. In chapter 3 we discuss preliminary theoretical work on the development of an EUV entangled-photon source, using two-photon emission from the metastable 2s state in neutral Helium. Such a source, if demonstrated, can possibly even be extended to the zeptosecond regime in the future.

Following is a list of published manuscripts that have resulted from the research work undertaken in pursuance of the requirements for this degree:

- Gao, X., **Pandey, S.**, Kianinia, M., Ahn, J., Ju, P., Aharonovich, I., ... & Li, T. (2021). Femtosecond laser writing of spin defects in hexagonal boron nitride. *ACS Photonics*, 8(4), 994-1000.
- Wang, Y., **Pandey, S.**, Greene, C. H., & Shivaram, N. (2022). Attosecond entangled photons from two-photon decay of metastable atoms: A source for attosecond experiments and beyond. *Physical Review Research*, 4(3), L032038.
- Walz, F., **Pandey, S.**, Tan, L. Z., & Shivaram, N. (2022). Electric field measurement of femtosecond time-resolved four-wave mixing signals in molecules. *Optics Express*, 30(20), 36065-36072.
- **Pandey, S.**, Tan, L. Z., Walz, F., Makhija, V., & Shivaram, N. (2023). Ultrafast Field-Resolved Nonlinear Optical Spectroscopy in the Molecular Frame. *arXiv preprint arXiv:2311.18230*.
- **Pandey, S.**, Walz, F., & Shivaram, N. (2023). Electric Field-Resolved Nonlinear Optical Spectroscopy in Molecules with Lock-in Enabled Phase Tracking. In Preparation.

1. ULTRAFAST TEMPORAL PHASE-RESOLVED NONLINEAR OPTICAL SPECTROSCOPY IN THE MOLECULAR FRAME

1.1 Introduction

Ultrafast dynamics in molecules occur on time scales ranging from attoseconds to picoseconds. These dynamics are routinely studied using photoionization based spectroscopies, ultrafast electron diffraction, and all-optical spectroscopies [2]–[5]. Due to the multidimensional nature of the problem, the study of ultrafast dynamics in molecules typically requires a number of complimentary measurements to disentangle the dynamics for any given system. An all-optical experimental observable that is sensitive to electronic symmetry could offer important insight into ultrafast electron and electron-nuclear dynamics. Ultrafast optical measurements, including transient absorption spectroscopy, rely on the nonlinear optical response of the target molecule. A measurement that probes higher-order nonlinear response of molecules can provide detailed information on the symmetry of the involved electronic states. Further, in an all-optical measurement, completely resolving the emitted electric field (E-field) provides direct access to the induced polarization which is intricately related to the ultrafast evolution of the system being studied. Combining ultrafast field-resolved spectroscopy with nonlinear optical response measurements will thus enable tracking of transient electronic symmetries in excited molecules. Recently, field-resolved ultrafast measurements using attosecond streaking [6]–[8], direct field sampling [9]–[17] and spectral interferometry [18] have emerged as sensitive methods to probe ultrafast dynamics. Applying field-resolved nonlinear optical spectroscopy to laser excited molecules is an important step towards realizing the full potential of nonlinear optical spectroscopy in probing ultrafast dynamics.

1.2 Theoretical Background

1.2.1 Nonlinear Optical Response

The state of a quantum mechanical system can be readily described in terms of its density matrix. The diagonal elements of the density matrix contain the populations of the

various energy eigenstates, and the off-diagonal elements contain the coherences between the corresponding levels. Let us assume that we have a quantum mechanical system, say a molecule, represented by the density matrix $\rho(t)$. In the interaction picture, its time-dependence can be calculated using the relation

$$\dot{\rho}_I = -i[H'_I, \rho_I] \quad (1.1)$$

where H'_I is some perturbation Hamiltonian in the interaction picture. For the purposes of this work, this perturbation will always be provided by the laser fields that interact with the system, i.e., $H' = \mu \cdot E$. This equation has a formal Dyson series solution

$$\begin{aligned} \rho_I(t) = \rho_I(t_0) + \sum_{n=1} (-i)^n \int_{t_0}^t dt_n \int_{t_0}^{t_n} dt_{n-1} \dots \int_{t_0}^{t_2} dt_1 \\ [H'_I(t_n), [H'_I(t_{n-1}), \dots, [H'_I(t_1), \rho_I(t_0)] \dots]] \end{aligned} \quad (1.2)$$

Denoting $U_0(t) = e^{-iH_0 t}$, we can convert back into the Schrodinger picture

$$\begin{aligned} \rho(t) = \rho(t_0) + \sum_{n=1} (-i)^n \int_{t_0}^t dt_n \int_{t_0}^{t_n} dt_{n-1} \dots \int_{t_0}^{t_2} dt_1 E(t_n) E(t_{n-1}) \dots E(t_1) \\ U_0(t, t_0) [\mu_I(t_n), [\mu_I(t_{n-1}), \dots, [\mu_I(t_1), \rho_I(t_0)] \dots]] U_0^\dagger(t, t_0) \end{aligned} \quad (1.3)$$

We are interested in the induced polarization of the system, when perturbed by the incident light fields. In the density matrix formulation, this is defined as the expectation value of the dipole moment operator with the density matrix $P = \langle \mu \rho \rangle$. We obtain the following expression by suppressing the interaction subscript and ignoring the constant term

$$\begin{aligned} P(t) = \sum_{n=1} (-i)^n \int_{t_0}^t dt_n \int_{t_0}^{t_n} dt_{n-1} \dots \int_{t_0}^{t_2} dt_1 E(t_n) E(t_{n-1}) \dots E(t_1) \\ \langle U_0(t, t_0) \mu(t) [\mu(t_n), [\mu(t_{n-1}), \dots, [\mu(t_1), \rho(t_0)] \dots]] U_0^\dagger(t, t_0) \rangle \end{aligned} \quad (1.4)$$

If we let $t_0 \rightarrow -\infty$, then $U_0^\dagger(t, t_0)|\Psi\rangle = |\Psi_I\rangle$, and the expectation value is to be taken in the interaction picture. We can now decompose the induced polarization as $P(t) = \sum_{n=1} P^{(n)}$, and using a different set of time variables

$$\tau_1 = t_2 - t_1, \tau_2 = t_3 - t_2 \dots \tau_n = t - t_n \quad (1.5)$$

we obtain the n^{th} order induced polarization (for $t_1 = 0$)

$$P^{(n)} = (-i)^n \int_0^\infty d\tau_n \dots \int_0^\infty d\tau_1 E(t - \tau_n) \dots E(t - \tau_n - \tau_{n-1} \dots - \tau_1) \langle \mu(\tau_n + \tau_{n-1} \dots + \tau_1) [\mu(\tau_{n-1} \dots + \tau_1), \dots, [\mu(0), \rho(-\infty)] \dots] \rangle \quad (1.6)$$

This is nothing but the convolution of all fields with a response function

$$S^{(n)}(\tau_n, \dots, \tau_1) = (-i)^n \langle \mu(\tau_n + \tau_{n-1} \dots + \tau_1) [\mu(\tau_{n-1} \dots + \tau_1), \dots, [\mu(0), \rho(-\infty)] \dots] \rangle \quad (1.7)$$

This response function, in the frequency domain is known as the nonlinear susceptibility, and is a tensor. Taking the Fourier transform of the above equation gives

$$P^{(n)}(\omega) = \alpha^{(n)}(\omega) E(\omega_n) E(\omega_{n-1}) \dots E(\omega_1) \quad (1.8)$$

For instance, $\alpha_{ij}^{(1)}$ is the usual polarizability matrix, while $\alpha_{ijk}^{(2)}$ and $\alpha_{ijkl}^{(3)}$ are commonly referred to as the hyperpolarizability and the second-hyperpolarizability. In the rest of this thesis, we will denote the third-order response $\alpha_{ijkl}^{(3)}$ using the symbol $\gamma_{ijkl}^{(2)}$, which is a rank 4 tensor. For molecules, the (hyper-)polarizabilities are defined in some coordinate system fixed with respect to the molecules' symmetry axis. However, in an experiment, we can usually only measure an effective nonlinear response, which is a function of a few of these components. This is both due to experimental constraints, and because many of the molecular-frame components either vanish or are identical. This nonlinear response, denoted $\chi^{(n)}$, is a bulk quantity usually measured in some given lab frame. The lab-frame and molecular-frame quantities are related by a symmetry transformation. Let's consider the

second-hyperpolarizability $\gamma_{ijkl}^{(2)}$, which transforms like a tensor when the molecule is rotated with respect to the polarization axis of the incoming probe beam, as

$$\chi_{k'j'i'h'}^{(3)} = \frac{\partial x_k}{\partial x_{k'}} \frac{\partial x_j}{\partial x_{j'}} \frac{\partial x_i}{\partial x_{i'}} \frac{\partial x_h}{\partial x_{h'}} \gamma_{kjih}^{(2)} = A_{kk'}^{-1} A_{jj'}^{-1} A_{ii'}^{-1} A_{hh'}^{-1} \gamma_{kjih}^{(2)} \quad (1.9)$$

where A is the 2D rotation matrix in the transverse plane

$$A = \begin{bmatrix} \cos(\theta) & -\sin(\theta) \\ \sin(\theta) & \cos(\theta) \end{bmatrix} \quad (1.10)$$

In nonlinear optical spectroscopy, a set of laser beams are focused onto the target system, which induces a transient polarization, as described by equation 1.8. This induced polarization, which can be thought of as an oscillating charge distribution, then re-emits radiation $E^{(n)} = iP^{(n)}$ which forms the signal that forms the observable. The emitted signal thus has a real component that is in phase with the incident radiation, and an imaginary component, that is out of phase with it. Knowledge of the real and imaginary components of the emitted signal are required to fully measure the response tensor, which can be complex-valued. Note that when the direction of time is reversed in a nonlinear optical experiment, all involved electric fields change sign. For an isotropic system, say a gas at room temperature, the induced dipole should also change direction. When equation 1.8 is applied to isotropic systems, time reversal changes the sign of the left-hand side for all orders, but on the right-hand side, only odd orders change sign. Thus, for an isotropic system all even-ordered nonlinear response vanishes, and the third-order response is the first non-vanishing nonlinear response.

In symmetric top molecules, the two unique components of the (linear) polarizability tensor, α_{\parallel} and α_{\perp} , contain limited information compared to the multiple non-zero tensor components of higher-order hyperpolarizability tensors. It is, therefore, conceivable that measuring the third-order response can provide detailed information on the symmetry of the involved electronic states. We can go one step further and calculate, for a few small molecules, the lab frame third-order response using 1.9. For N_2 and CO_2 molecules, the third-order response as a function of the relative angle between the laser polarization and the molecules' symmetry-axis is shown in figure 1.1. Details about the ab initio calculation of

the second-hyperpolarizabilities are given in Appendix B. The alignment angle-dependence of the third-order response shows remarkable similarity to the highest occupied molecular orbital (HOMO) in both the molecules.

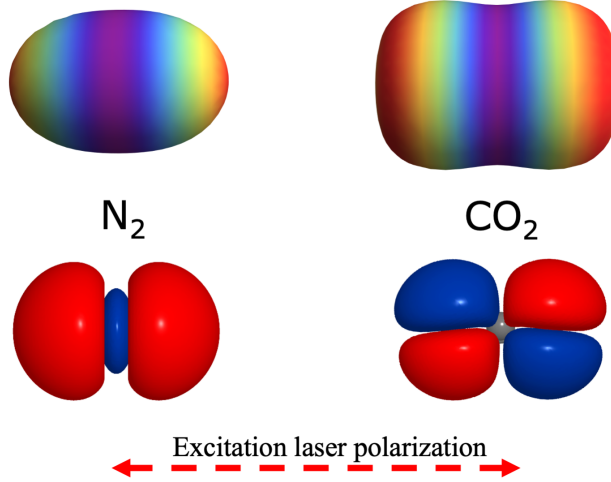


Figure 1.1. Magnitude of $\gamma_{xxxx}^{(2)}$ as a function of the relative angle between the laser polarization and the molecules' symmetry-axis, for CO_2 and N_2 molecules. Their highest occupied molecular orbitals are also shown.

One of the most common experimental techniques to study third-order optical response [19]–[22] is four-wave mixing (FWM). In FWM, three coherent electromagnetic fields excite a third-order transient dipole in a sample, which then emits a fourth coherent electromagnetic field. It is classified as degenerate four-wave mixing (DFWM) or non-degenerate four-wave mixing (N-DFWM), depending on whether the excitation pulses have the same frequency or not. The direction of propagation of the emitted radiation (signal) depends on the propagation direction of the incident fields. If we make the paraxial approximation for the laser fields, and set $E(\omega_i) \propto (e^{k_i r - \omega_i t} + e^{-k_i r + \omega_i t})$, then equation 1.8 dictates that the induced dipole emits radiation in a direction allowed by the following phase-matching condition

$$E^{(3)} = iP^{(3)} \propto e^{(k_1+k_2+k_3)r - (\omega_1+\omega_2+\omega_3)t} + e^{(k_1+k_2-k_3)r - (\omega_1+\omega_2-\omega_3)t} + \dots \quad (1.11)$$

The different terms in the above expression not only result in emission in different spatial directions, but also probe different electronic states. This becomes clear when these terms are represented in terms of double-sided Feynman diagrams, the details of which can be

found in any standard reference. We are only interested in the second term of the above expansion. The emitted radiation corresponding to this phase-matching condition has the same frequency (when $\omega_2 = \omega_3$) as one of the incident fields, \vec{E}_1 , and travels in a direction offset from \vec{k}_1 by $\Delta\vec{k} = \vec{k}_2 - \vec{k}_3$. Two common FWM geometries are shown in figure 1.2, (a) one where $\vec{k}_2 \neq \vec{k}_3$, and one where (b) $\vec{k}_2 = \vec{k}_3$.

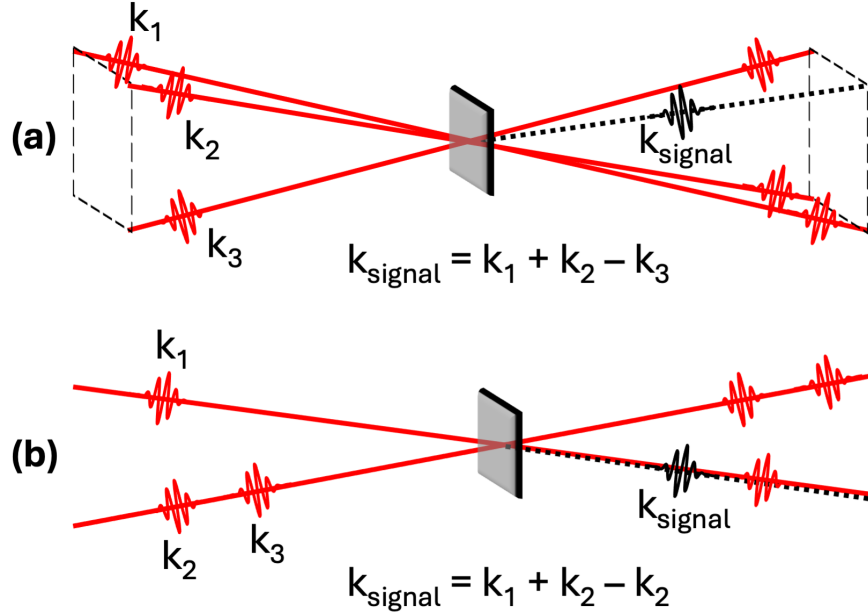


Figure 1.2. Folded BOXCARS and planar geometries of degenerate four-wave mixing (DFWM) are shown. Phase-matching dictates the direction of the emitted four-wave mixing signal. Folded BOXCARS geometry has the advantage that the emitted signal can be spatially separated from the incident laser beams.

The third-order nonlinear optical response of a molecule has three dominant sources - bound electronic, plasma, and rotational nonlinearity [23]. Vibrational nonlinearities are not observed in our experiments due to the limited bandwidth of typical femtosecond laser pulses. Rotational nonlinearity, which arises from nuclear motion, is slower compared to the (near-instantaneous) electronic nonlinearity, which arises from the distortion of the molecular electron cloud by the intense laser field [24]. For low enough laser intensities, the plasma nonlinearity can be ignored. When all the DFWM laser pulses have polarization along a fixed

axis in the lab frame, say z , the emitted third-order signal (in folded BOXCARS geometry), from a single molecule can be written as

$$E_{signal,z}(\omega, \theta) = i\chi_{zzzz}^{(3)}(\omega, \theta)E_{1,z}(\omega)E_{2,z}^*(\omega)E_{3,z}(\omega) \quad (1.12)$$

where θ is the relative angle between the laser polarization along \hat{z} and the molecules' symmetry-axis, ω is the angular frequency, the subscripts 1, 2 and 3 correspond to the three DFWM pulses which are assumed to be temporally overlapped with zero time delay. For linear molecules, which will be the focus of this work, the lab frame third-order susceptibility can be related to the molecular-frame second-hyperpolarizabilities as

$$\chi_{zzzz}^{(3)}(\omega, \theta) = \gamma_{zzzz}^{(2)}(\omega) \cos^4(\theta) + \frac{3}{2}\gamma_{zzxx}^{(2)}(\omega) \sin^2(2\theta) + \gamma_{xxxx}^{(2)}(\omega) \sin^4(\theta) \quad (1.13)$$

It is well known that molecules can be excited rotationally with intense non-resonant laser pulses, leading to periodic rotational revivals on the time scale of tens of picoseconds [25]–[28]. Electron dynamics, on the other hand, occur on femtosecond and attosecond time scales after interaction with the excitation laser pulse. This separation of time scales allows probing of femtosecond electronic response by first exciting a rotational wavepacket, and then probing using DFWM. Once the DFWM input pulses are characterized, a measurement of $E_{signal}(t)$ from a rotational wavepacket can give direct access to molecular-frame second-hyperpolarizability. This is essentially similar to measuring the lab-frame nonlinear response in equation 1.13 for multiple θ to get the molecular-frame response tensor components.

1.2.2 Extraction of Molecular-Frame Response

Nonlinear spectroscopy of gas-phase molecules inevitably suffers from rotational averaging. The emitted FWM signal, measured in the laboratory frame, is integrated over all the different orientations of the molecules that interact with the FWM pulses. To be able to measure nonlinear response in the molecule's own frame of reference, we need to align all the molecules in a particular orientation. In the Born-Oppenheimer approximation, linear molecules are well represented as a quantum rigid rotor, with a slower rotational response

due to the rotation of the entire molecule, and a faster electronic response due to dynamics of the electronic states of the molecule [23]. For instance, field-free alignment [25], [26], [29] in CO_2 molecule occurs after tens of picoseconds after laser excitation [30]. But electronic response due to non-resonant excitation lasts for only the duration of the probe pulse. This separation of timescales makes it possible to first align the molecules impulsively, and then measure the electronic response around a rotational revival.

A large body of work has been done in the field of impulsive alignment of gas-phase molecules, and the characterization of their degree of alignment. Here, we first review the theory of impulsive alignment for the special case of linear molecules, before discussing the technique of Orientation Resolution through Rotational Coherence Spectroscopy (ORRCS) to extract molecular-frame quantities directly from pump-probe time delay-dependent signals.

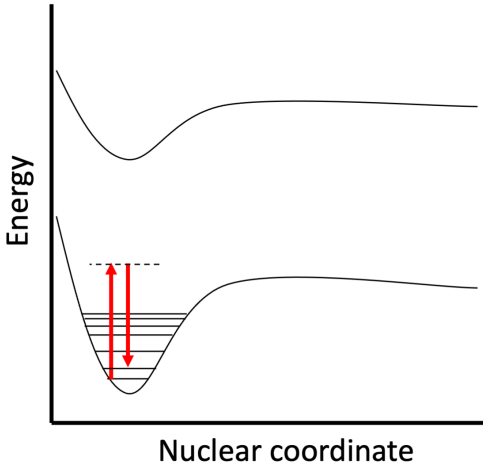


Figure 1.3. Qualitative description of multiphoton Raman excitation of the ground state rotational manifold in a prototypical molecule.

When an intense non-resonant laser field is incident on a molecule, it can excite the ground rotational states of the molecule through a Raman transition, as depicted in figure 1.3. For most simple molecules, the quantum rigid rotor, with an additional centrifugal term,

accurately describes the rotational degrees of freedom accessible. The quantum rigid rotor Hamiltonian is [31]

$$H_{rot} = \frac{1}{2}(I_{aa}\omega_a^2 + I_{bb}\omega_b^2 + I_{cc}\omega_c^2) = \frac{J_a^2}{2I_{aa}} + \frac{J_b^2}{2I_{bb}} + \frac{J_c^2}{2I_{cc}} \quad (1.14)$$

where a, b and c are the principal axes of the molecule. For linear molecules, like CO₂, $I_{aa} = 0, I_{bb} = I_{cc} = I$, and the Hamiltonian simplifies to

$$H_{rot} = \frac{\hat{J}^2}{2I} \quad (1.15)$$

with energy eigenvalues

$$E_{rot} = \frac{\hbar^2}{2I}J(J+1) \quad (1.16)$$

Since the operators \hat{J}^2 and \hat{J}_Z (Z is the lab-frame z-axis) commute with H_{rot} , the eigenstates are the familiar scalar spherical harmonics

$$\begin{aligned} \hat{J}^2|J, M\rangle &= \hbar^2 J(J+1)|J, M\rangle \\ \hat{J}_Z|J, M\rangle &= \hbar M|J, M\rangle \end{aligned} \quad (1.17)$$

The treatment of a linear molecule is enough to illustrate how a coherent source of radiation, like a laser pulse, can align molecules. The degree of alignment of a molecule is often measured with the expectation value of $\cos^2 \theta$, taken with respect to the rotational wavefunction of the molecule. Here θ is the angle between the molecule's symmetry axis and the lab-frame z-axis. Suppose that an incident laser pulse excites a coherent superposition of the rigid rotor states in the molecule given by

$$|\Psi\rangle = \sum_{J,M} a_{JM}(t)|J, M\rangle \quad (1.18)$$

For simplicity we will ignore the two-photon dipole selection rules ($\Delta J = 0, \pm 2$ and $\Delta M = 0$), and assume that the first N rigid rotor states are excited with equal probability.

Then the expansion coefficients $a_{JM}(t) = e^{iBJ(J+1)t}/\sqrt{N}$. The corresponding density matrix is

$$\rho(t) = \sum_{J,M,J',M'} a_{JM}(t) a_{J'M'}^*(t) |J, M\rangle \langle J', M'| \quad (1.19)$$

The alignment parameter can be calculated as

$$Tr(\rho \cos^2 \theta) = \frac{1}{N} \sum_{J,M,J',M'} e^{iB(J(J+1)-J'(J'+1))t} \langle J', M' | \cos^2 \theta | J, M \rangle \quad (1.20)$$

On the other hand, if we had an ensemble of incoherently excited rotational states, the corresponding density matrix would be

$$\rho(t) = \sum_{J,M} p_{J,M} |J, M\rangle \langle J, M| \quad (1.21)$$

where $p_{J,M}$ are the classical probabilities for the eigenstates to be populated. As is evident, this density matrix corresponds to a mixed state. For simplicity, again assume that the first N states are equally probable, giving $p_{J,M} = 1/N$. The alignment parameter can be calculated as

$$Tr(\rho \cos^2 \theta) = \frac{1}{N} \sum_{J,M} \langle J, M | \cos^2 \theta | J, M \rangle \quad (1.22)$$

Sample calculations, comparing the time-dependent degree of alignment $\langle \cos^2 \theta \rangle$ in equation 1.20 and equation 1.22 are shown in figure 1.4. For incoherent excitation, $\langle \cos^2 \theta \rangle = 1/3$, which represents an isotropic angular distribution across all θ . But for a coherent excitation the molecular alignment parameter suddenly increases during small windows of time, known as rotational revivals. Near a rotational revival the rotational states add constructively and cause the molecule to be strongly aligned in a particular direction (see figure 1.4). The summation in equation 1.22 is a subset of the summation in equation 1.20. Indeed, it is the off-diagonal elements of the matrix $\langle J', M' | \cos^2 \theta | J, M \rangle$ that lead to the phenomena of impulsive alignment. These 'coherences' are created only with coherent excitation (i.e., a fixed phase relationship exists between the various excited states), and have no classical analog. Interactions due to the environment, such as collisions, can cause the various states to dephase, and suppress impulsive alignment.

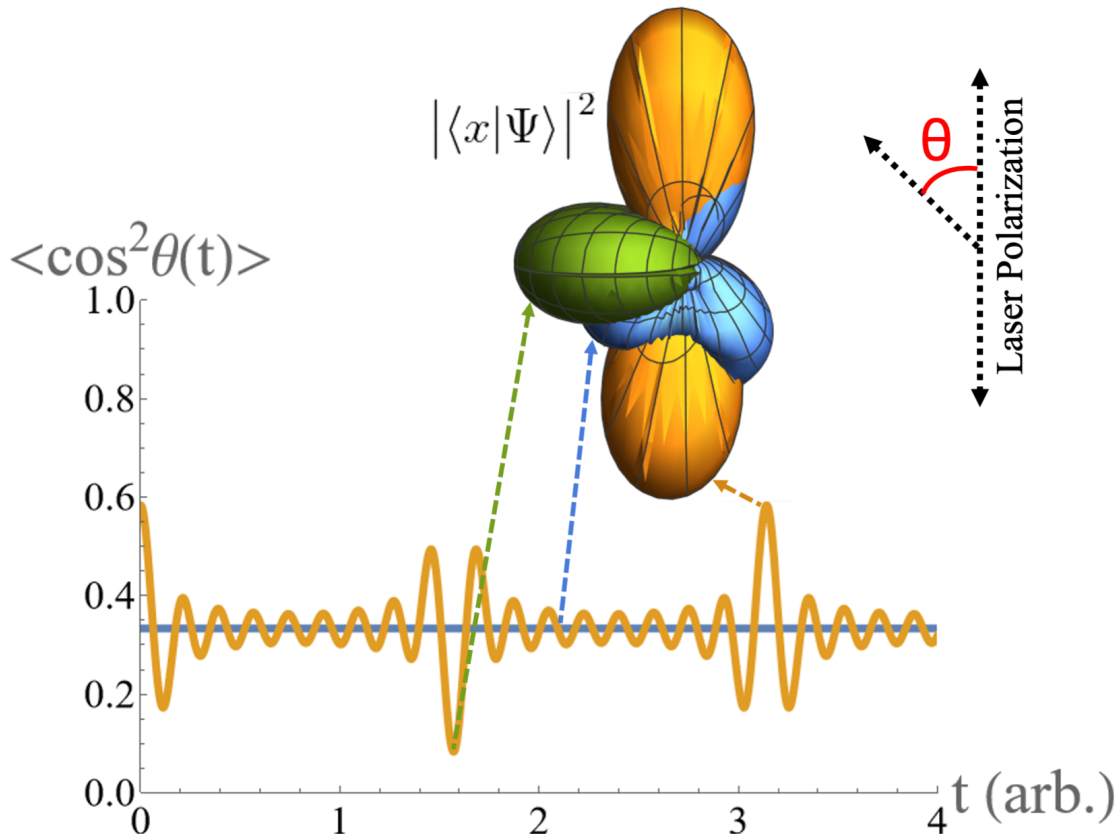


Figure 1.4. The degree of alignment for a quantum rigid rotor is plotted for the case of a coherent excitation (orange), and an incoherent excitation (blue), when the first 10 states are excited with equal probability. Magnitude of the wavefunction corresponding to density matrix Even in this simplified toy model, only a coherent superposition of rotational states can lead to alignment. Scaling of the x-axis to physical units of time depend on the moment of inertia of the rigid rotor.

Figure 1.5 shows the transient birefringence experienced by a probe pulse (proportional to $\langle \cos^2 \theta \rangle$ [27], [28], [32]), in gas-phase CO_2 and N_2 , pumped by a strong near-infrared (NIR) pulse. Note how at larger pump-probe time delays, the revival peaks in CO_2 start to weaken due to collisional dephasing. This is most noticeable at higher temperatures and densities.

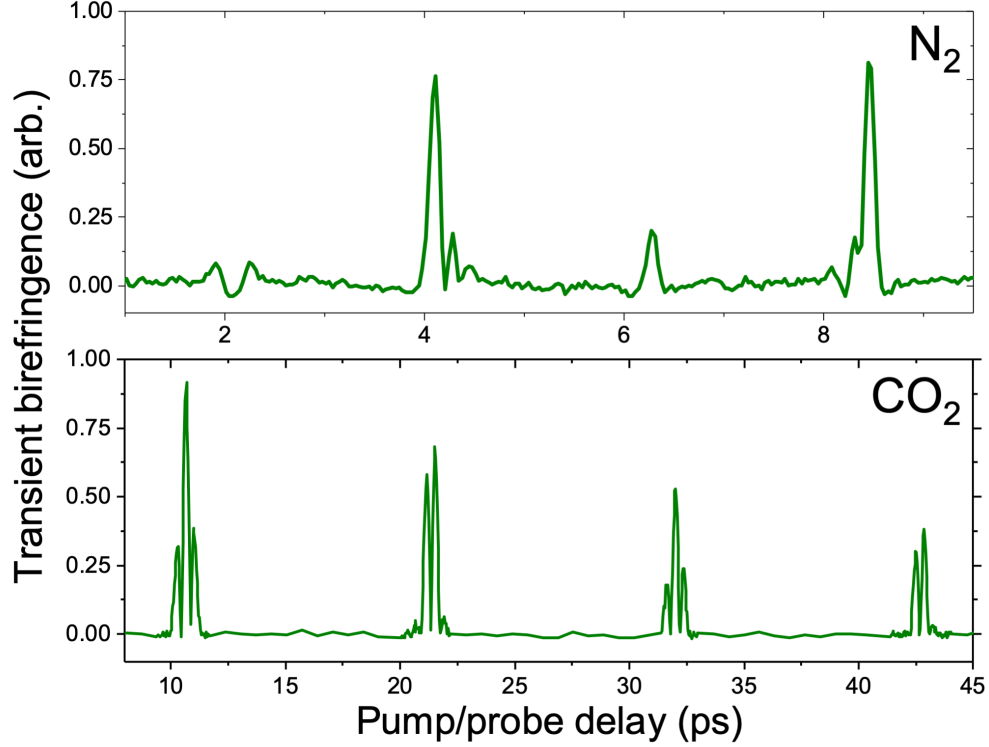


Figure 1.5. Transient birefringence induced by a strong NIR pump pulse, probed by a weaker NIR pulse. The amount of induced birefringence is proportional to the amount of probe light that passes through a crossed polarizer placed after the interaction.

One can also directly solve for the eigenfunctions of the time-dependent Hamiltonian in the presence of the intense laser field

$$\begin{aligned}
 H &= \frac{\hat{J}^2}{2I} - \vec{\mu} \cdot \vec{E}(t) \\
 \vec{E}(t) &= \vec{E}_0 e^{-t/2\tau^2} \cos(\omega t)
 \end{aligned}
 \tag{1.23}$$

and retrieve the rotational wavepacket launched by an incident laser pulse with known pulse parameters. It has been shown that after exciting a rotational wavepacket in a molecule, the time evolution of some experimental observables can be used to extract the molecular-frame angle-dependence of the observables in question [33], [34]. To see how this works consider some observable S that depends on the molecule's 3-dimensional (3D) orientation

in the laboratory frame. Equivalently, we can express this quantity in the molecular frame, as $S(\phi, \theta, \chi)$, with the Greek letters denoting the Euler angles of the incident laser polarization vector in the molecule's body-fixed axes (see [33] for more details). We can expand this function in any complete basis of $\text{SO}(3)$. A favorable choice is the set of Wigner D-matrices:

$$D_{mk}^j(\phi, \theta, \chi) = \langle jm | R(\phi, \theta, \chi) | jk \rangle \quad (1.24)$$

where $R(\phi, \theta, \chi)$ is the 3D rotation matrix. A linearly polarized pump pulse excites a cylindrically symmetric distribution of rotational states, rendering S independent of ϕ :

$$S(\theta, \chi) = \sum_{jk} C_{jk} D_{0k}^j(\phi, \theta, \chi) \quad (1.25)$$

If S is measured in the laboratory frame, for a rotational wavepacket excited by a preceding alignment Pump pulse, its expectation value as a function of time delay is

$$\begin{aligned} \langle S \rangle(t) &= \int d\Omega \rho(\theta, \chi, t) S(\theta, \chi) \\ &= \sum_{jk} C_{jk} \int d\Omega \rho(\theta, \chi, t) D_{0k}^j(\phi, \theta, \chi) \\ &= \sum_{jk} C_{jk} \langle D_{0k}^j \rangle(t) \end{aligned} \quad (1.26)$$

The determination of the angle-dependence of S reduces to finding the coefficients C_{jk} , since the expectation values of the D-matrices can be calculated by first calculating the rotational wavepacket, for a given set of experimental parameters. This technique has been used to extract molecular alignment angle-dependent photoionization probabilities, from a measurement of photoionization yields as a function of the aligning pump - ionizing probe time delay [35], [36]. The goal of the current work is to apply this technique to extract the molecular-frame nonlinear electronic response from the measured lab-frame optical response.

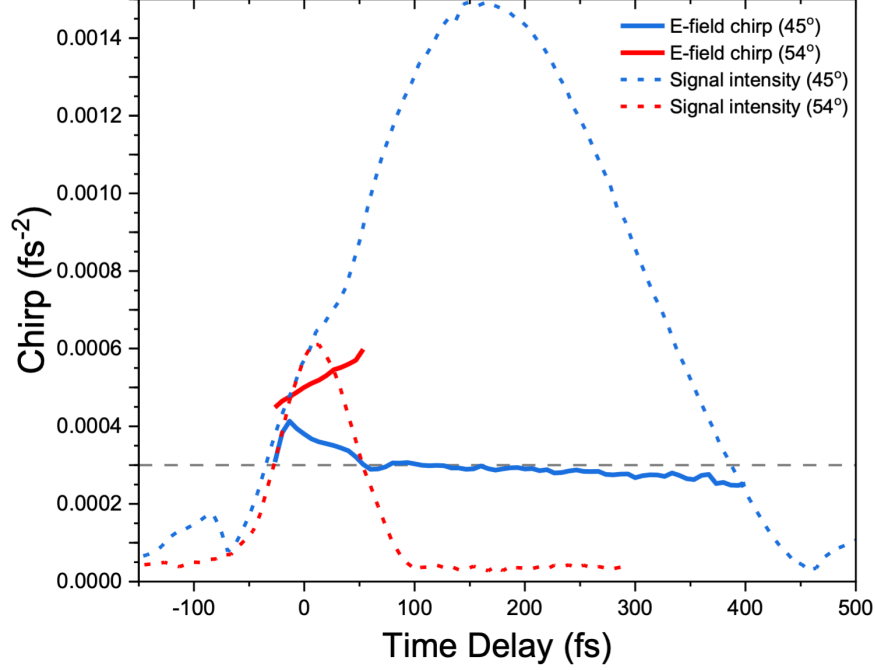


Figure 1.6. A DFWM measurement in the folded BOXCARS geometry, where two of the excitation pulses are co-timed and co-polarized. The third excitation pulse is time-delayed, with a relative polarization of either 45° or 54.7° (magic angle). The intensity of the emitted signal for 45° (dashed blue) shows a slow rotational response, while for 54.7° (dashed red) the rotational nonlinearity is suppressed, and only the electronic nonlinearity is observed (see text). However, the temporal chirp of the emitted E-field (solid red/blue) is higher than its nominal value only when the bound electronic nonlinearity is non-zero, in both the cases. The chirp of the emitted signal E-field drops back to its nominal value at later times once the rotational response becomes dominant (solid blue).

1.3 Experimental Methods

1.3.1 Phase-resolved Nonlinear Spectroscopy

Nonlinear optical response of a material results from the coherent addition of multiple excitation pathways [37]. Multidimensional spectroscopy is often used to help disentangle the dynamics resulting from different pathways [38]. Additionally, signals from different pathways can have different propagation direction, and can be further isolated spatially. All such pulse-averaged measurements, however, integrate out the information contained

in the temporal profile of the emitted signal E-field. It can be argued that time-resolved insight into light-matter interactions can be gained equally well by temporal phase-resolved measurements. In a nonlinear optical process, any emitted light contains an imprint of the nonlinear interaction involved. For instance, in four-wave mixing (FWM), the emitted signal is related to the induced third-order polarization in the medium and is determined by the third-order nonlinear response tensor $\chi_{ijkl}^{(3)}$. A measurement of the amplitude and phase of such emitted signal fields gives access to the maximum information that can be gained in an all-optical measurement. It has been demonstrated that a measurement of the full E-field of the emitted field in a degenerate four-wave mixing (DFWM) experiment can be used to distinguish between contributions from electronic and nuclear degrees of freedom [18]. The measured E-field consists of the amplitude $E(t)$ and phase $\varphi(t)$. The measured temporal phase can be expanded as a polynomial in time t as

$$\varphi(t, T) = a_0(T) + a_1(T) \cdot t + a_2(T) \cdot t^2 + a_3(T) \cdot t^3 \dots \quad (1.27)$$

where T is the time delay between the pulses that act as the pump/probe. The second-order polynomial coefficient a_2 , which is generally the dominant nonlinear fit coefficient, is called temporal chirp, and modulates as a function of T . Figure 1.6 illustrates the advantages of measuring the full E-field of the emitted nonlinear signal. When the DFWM pump/probe pulses have a relative polarization of 45° , the measured signal intensity shows a broad rotational response that lasts up to 500 fs. For linear molecules, however, $\Delta n_{\parallel} = -2\Delta n_{\perp}$ [39], and the rotational response is exactly cancelled when the relative polarization between the DFWM pump/probe pulses is $\theta = \tan^{-1}(\sqrt{2}) = 54.7^\circ$ [40]–[44]. Note how the temporal chirp ($a_2(T)$) of the emitted E-field is higher than the chirp of the excitation pulses only when the bound electronic nonlinearity is non-zero, but drops down to its nominal value at later times once the rotational response becomes dominant. This is also corroborated with theoretical simulations [18] of the bound electronic nonlinearity. Owing to its heightened sensitivity to electronic nonlinearities, temporal phase-resolved E-field measurements will be investigated further in the rest of this chapter, and applied to studying nonlinear electronic response in aligned molecules.

1.3.2 Lock-in Enabled Interferometry

The emitted nonlinear signal that travels in the phase-matched direction can be detected using a square law detector, like a CCD/CMOS sensor, that only measures the intensity of the incident light. Such a measurement does not contain any information about the phase of the emitted radiation with respect to the incident fields. Techniques like optical Kerr effect (OKE) spectroscopy [21], [45], [46] measure the pulse-averaged real and imaginary parts of the signal using optical heterodyning (OHD) with a local oscillator (LO). In our experiments we use spectral interferometry for the measurement of very weak (\sim pJ) femtosecond pulses [47], [48], using a known external reference for heterodyning. In this measurement, the signal field is combined temporally and spatially onto a spectrometer with a known reference pulse and the spectral interference fringes are recorded. If the two beams are mutually delayed by a time τ the expression for the measured spectrum is

$$S(\omega) = S_R(\omega) + S_S(\omega) + \sqrt{S_S(\omega)S_R(\omega)} \cos(\varphi_{SR}(\omega) + \omega\tau) \quad (1.28)$$

The subscripts S and R stand for signal and reference, respectively. For convenience, the slow oscillating terms in our expressions will be denoted as "DC", and the fast oscillating terms as "AC". $S(\omega)$ is the spectral intensity, ω is the angular frequency, and $\varphi(\omega)$ is the spectral phase. φ_{SR} is the difference between the spectral phases of the signal and reference. To extract the signal phase $\varphi_S(\omega)$, we first Fourier transform $S(\omega)$ with respect to ω . The first two terms on the right-hand side of equation 1.28 only have a DC component. The last term contains the fringes between the two pulses and has fast oscillations, due to the $\omega\tau$ term in the argument of the cosine. The Fourier transform of $S(\omega)$ has a distinct non-zero frequency peak corresponding to the fringe period. We filter and shift this peak to 0 Hz to remove the $\omega\tau$ term, and then inverse Fourier transform the resulting spectrum [49] from which we can extract $\varphi_{SR} = \varphi_S(\omega) - \varphi_R(\omega)$. The reference pulse is intense enough to be characterized $(S_R(\omega), \varphi_R(\omega))$ separately using a Frequency Resolved Optical Gating (FROG) device [50]. Given the reference phase $\varphi_R(\omega)$ we can extract $\varphi_S(\omega)$.

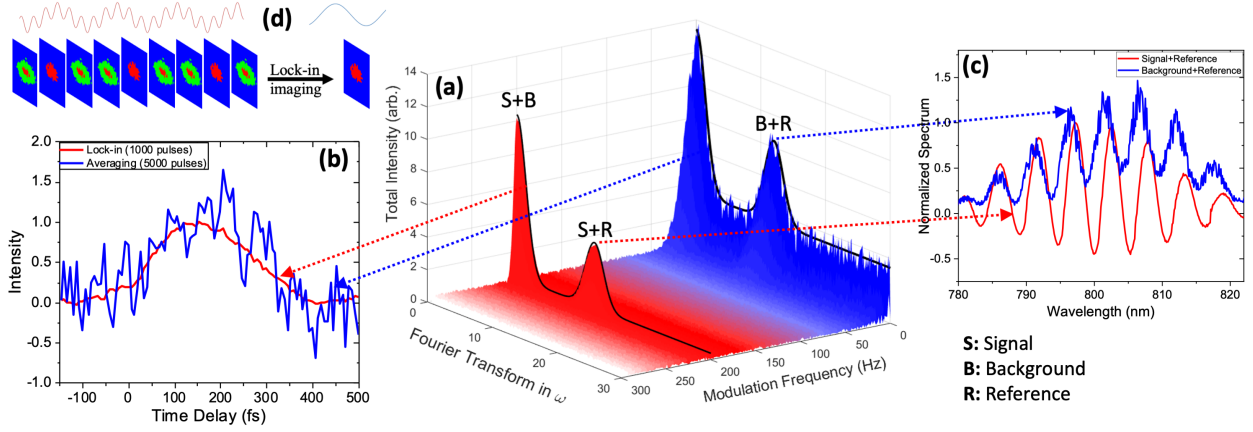


Figure 1.7. Schematic plot, inspired by experimental data, showing (a) the total light intensity detected on the spectrometer as a function of the modulation frequency and the Fourier transform variable (ω^* canonical to angular frequency ω). Incoherent background and other $1/f$ noise sources form the low-frequency noise depicted near 0 Hz modulation frequency. The lineout at 200 Hz represents the LI, AC terms of equation 1.31. (a) Terms without any interference fringes ($\omega^* = 0$) are shown for 0 Hz (blue) and 200 Hz (red) modulation frequency. (b) Interference terms ($\omega^* \neq 0$) between the signal and reference (red), and the background and reference (blue). (d) Schematic of lock-in enabled imaging.

Most nonlinear optical measurements have some form of a coherent background that co-propagates with the signal beam. With the addition of a coherent background, equation 1.28 becomes more complicated,

$$\begin{aligned}
 S(\omega) = & S_S(\omega) + S_R(\omega) + \sqrt{S_S(\omega)S_R(\omega)} \cos(\varphi_{SR}(\omega) + \omega \tau) \\
 & + S_B(\omega) + \sqrt{S_B(\omega)S_R(\omega)} \cos(\varphi_{BR}(\omega) + \omega \tau) \\
 & + \sqrt{S_S(\omega)S_B(\omega)} \cos(\varphi_{SB}(\omega))
 \end{aligned} \tag{1.29}$$

where the subscript B is used to denote the coherent background. φ_{BR} and φ_{SB} are the differences in spectral phase between background and reference, and signal and background, respectively. Presence of the coherent background and the additional interference fringes (additional terms in equation 1.29) it produces on the detector complicate the extraction of the signal spectrum and phase. Although coherent background from the excitation pulses

themselves can be spatially removed by using a non-collinear geometry, such separation is not possible between ground- and excited-state signals, which usually obey the same phase-matching.

One apparent solution to remove the coherent background is to use lock-in enabled detection. The excitation beam(s) is (are) modulated using an optical chopper, such that the signal of interest also modulates at the chopper frequency, and can be separated from any background that does not modulate. However, any coherent background light falling on the photodiode will interfere with the signal of interest, giving

$$I_{diode}(t) = |E_S(t) + E_B|^2 = I_S(t) + I_B + E_S(t) \cdot E_B \cos(\phi) \quad (1.30)$$

The interference term here modulates at the chopper frequency (because E_S is modulated by the optical chopper), and will add to the detected lock-in amplitude. This is an inescapable feature of intensity measurements in the presence of coherent background. This heterodyning of the signal due to background light is usually ignored, since the background is usually a constant. However, such interference can change the relative amplitudes of the real and imaginary parts of signal intensity in a non-trivial manner. The novel aspect of our interferometry implementation lies in the use of a home-built lock-in spectrometer that can separate the various interference terms in the spectrum. When one of the excitation laser beams is modulated at a given frequency (say 200 Hz) using an optical chopper, the emitted nonlinear signal of interest also modulates at this frequency. All other light falling on the spectrometer does not modulate at the chopper frequency. The terms in equation 1.29 can now be separated into those that modulate (denoted LI, AC) and those that do not (denoted LI, DC):

$$S_{LI,AC} = S_S(\omega) + \sqrt{S_S(\omega)S_R(\omega)} \cos(\varphi_{SR}(\omega) + \omega \tau) + \sqrt{S_S(\omega)S_B(\omega)} \cos(\varphi_{SB}(\omega)) \quad (1.31)$$

$$S_{LI,DC} = S_R(\omega) + S_B(\omega) + \sqrt{S_B(\omega)S_R(\omega)} \cos(\varphi_{BR}(\omega) + \omega \tau) \quad (1.32)$$

A lock-in imaging detection at the chopper frequency can separately measure $S_{LI,AC}$. The interference term of equation 1.30 is precisely the last term in the expression of $S_{LI,AC}$.

Since this term does not contain an $\omega\tau$ in the argument of the cosine, it does not lead to any detectable interference fringes and can be filtered out. The ideas discussed so far are succinctly represented in figure 1.7, which shows the 2D conjugate space of lock-in enabled interferometry, with the lock-in frequency on one axis, and the frequency of spectral oscillations on the other. The three labelled peaks in figure 1.7 (a) show the three interference terms from equation 1.29. Figure 1.7 (b) shows the typical improvement in SNR in a lock-in measurement, compared against simply averaging. The separation of interference fringes from different sources makes it advantageous to sample multiple points in the conjugate space to access additional information. One application of this additional information - passive stabilization of interference fringes - will be discussed later in this section. Analog lock-in amplifiers require separate phase-locked loops (PLLs), mixers etc. to do simultaneous lock-in measurements at multiple frequencies, and thus, generally only measure the signal of interest. In a digital setting, however, multiple lock-in measurements can be done in parallel to sample multiple points in the conjugate space of figure 1.7.

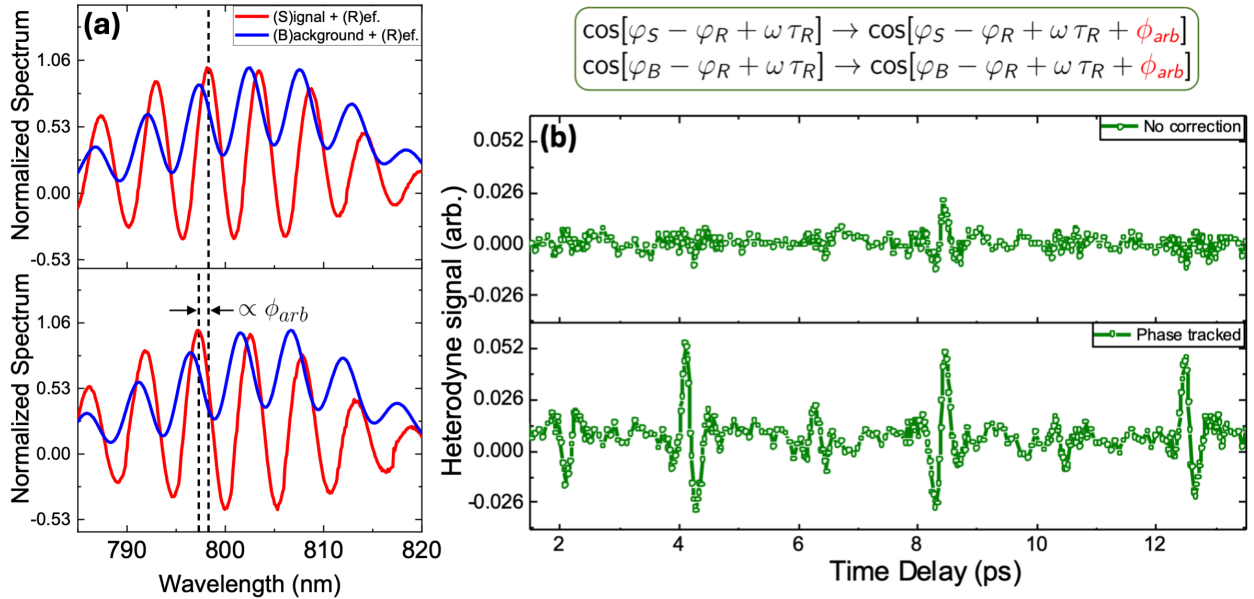


Figure 1.8. (a) Interference fringes between the signal and reference (red), and the background and reference (blue) are shown for two consecutive measurements. Even though the fringes drift between the two measurements, they are phase-locked relative to each other. (b) Without any drift correction, the measured heterodyne signal phase drifts between each measurement and vanishes when averaged.

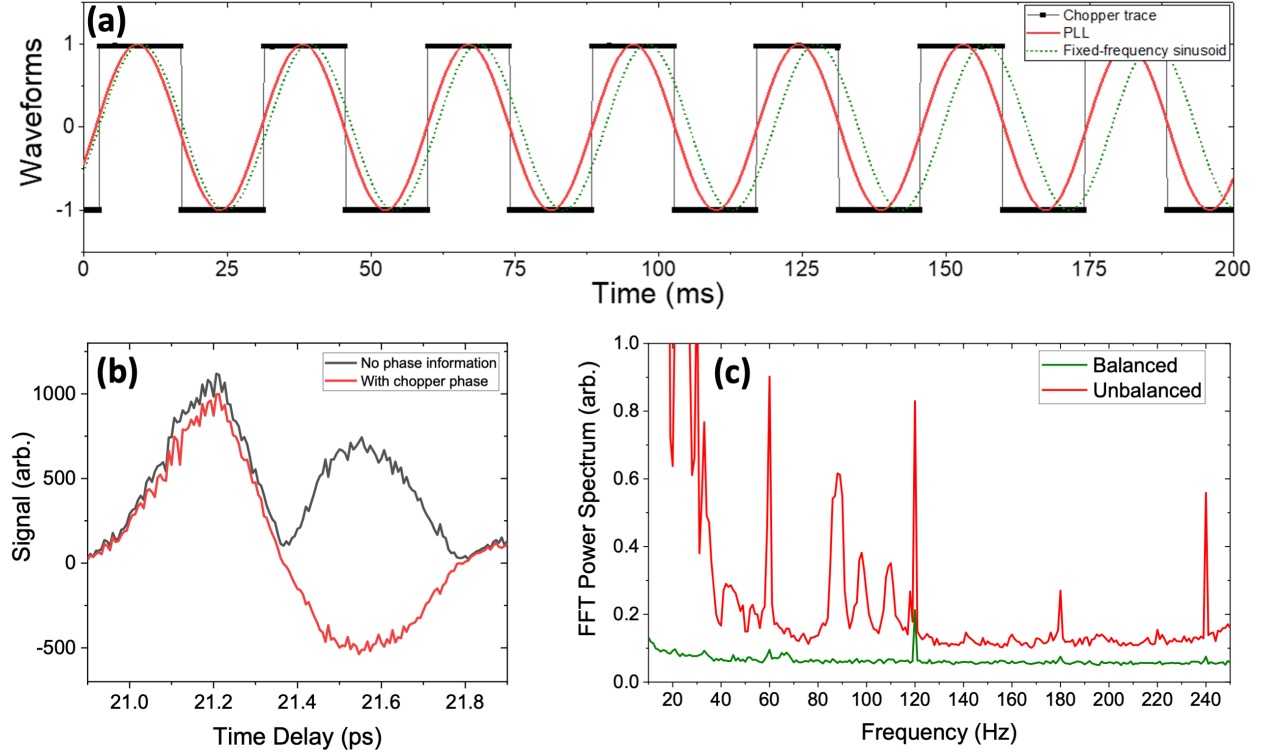


Figure 1.9. (a) Phase-locked loop (PLL) showing the chopper trace acquired by the DAQ, and the sinusoid derived from it, for subsequent phase-sensitive lock-in detection. Note how the phase of chopper drifts over time, and the PLL accounts for it. (b) Comparison between lock-in measurements, with and without information about the phase of the signal relative to the chopper. (c) Noise power spectrum of the CMOS camera, with and without balancing. The noise floor of the balanced detection is 30% lower than that of the unbalanced detection.

To implement lock-in enabled interferometry, an optical chopper is used to modulate one or more of the excitation beams. The signal light is measured on a CMOS camera, which is triggered at the laser repetition rate. Each camera frame is arranged in a time series (see figure 1.7 (d)), where each laser trigger counts as a unit increment of time. Thus, small drifts in the laser pulse arrival time become irrelevant and the modulation in the signal intensity results only from the chopping, regardless of the pulse repetition rate. The intensity of each pixel in the image time series is a 1-dimensional function of time. The chopper trace is acquired in real time using a DAQ, and fed into a software phase-locked loop (PLL). The chopper trace is a square wave, containing multiple harmonics. Inside the PLL, the acquired trace is Fourier transformed, bandpass filtered around the fundamental,

shifted to 0 Hz frequency, and inverse Fourier transformed to retrieve the phase of the fundamental [51]. From this phase, a sinusoid/cosinusoid (see figure 1.9) is constructed that are used to perform a lock-in analysis at the chopper frequency (dual-phase modulation lock-in amplification) [52]. A sinusoid/cosinusoid that is phase-locked with the laser trigger is essential for an accurate detection of the phase of the detected signal with respect to the chopper cycle. This phase contains crucial information about the sign of the signal, as seen in figure 1.9 (b). As an aside, it must be noted that since the chopper modulation follows a square wave, the signal modulates as $\sim 1 + \cos(2\pi ft)$; thus, a fraction of the signal modulating at the chopper frequency also appears at 0 Hz. The noise rejection of lock-in detection can be further improved by balancing the incident light before performing lock-in analysis [53]. This can be done by splitting the probe beam using a polarizing beamsplitter, and measuring the two beams separately, shot-to-shot, to subtract any common-mode noise. The added noise suppression is evident from figure 1.9 (c), where the noise floor of the balanced detection is 30% lower than that of the unbalanced one, at all frequencies. Similar correlation-based enhancements have been used in other schemes as well [54].

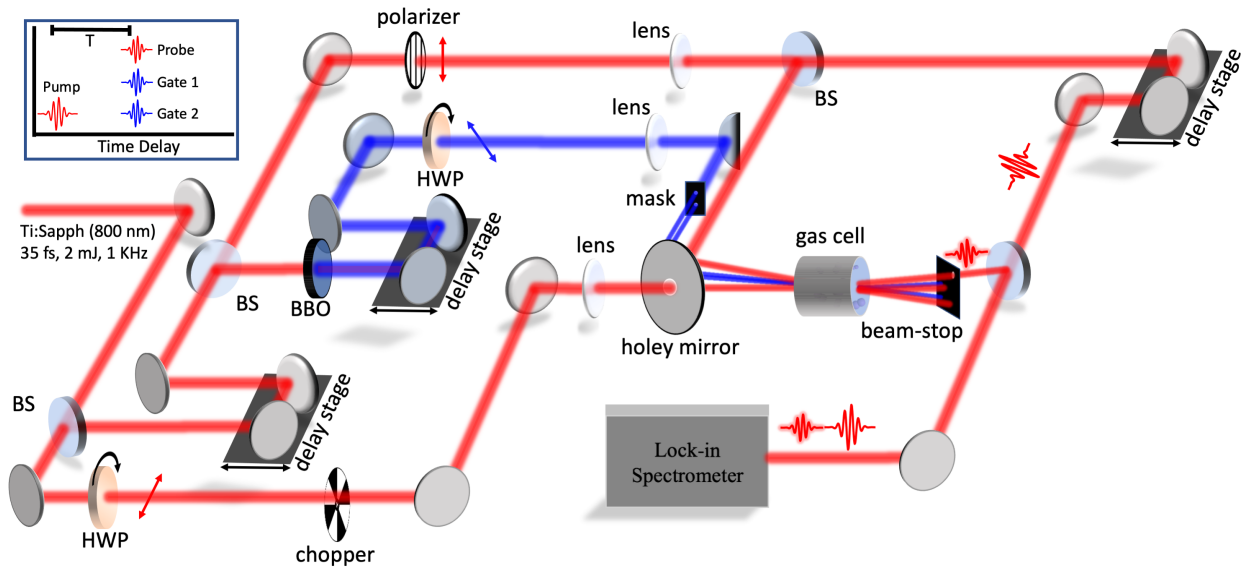


Figure 1.10. The alignment Pump, Probe and Gate beams are focused into a gas cell, and the emitted N-DFWM signal is spatially isolated after the interaction. It is combined with the external reference in a lock-in detection enabled spectrometer. The Reference is separately characterized using a FROG device (not shown here).

In contrast to single/double-channel lock-in spectrometers used with MHz repetition rate lasers [55], [56], the kHz repetition rate of high-powered lasers typically used in nonlinear optical experiments, like high-harmonic spectroscopy, makes real-time multi-channel digital lock-in analysis feasible. To demonstrate lock-in enabled interferometry, we describe a non-degenerate four-wave mixing (N-DFWM) experiment in gas-phase molecules. In the experiment, 60 fs near-infrared (NIR) pulses centered at 810 nm are split once and delayed. One arm forms the alignment Pump beam, while the other is split again to create the N-DFWM beams (see figure 1.10). The three N-DFWM beams are labelled Gate 1, Gate 2 and Probe. A single Gate beam is frequency doubled using a beta barium borate (BBO) crystal and delayed with respect to the probe beam. The Gate beam is then sent through a spatial mask to derive the co-timed Gate 1 and Gate 2 beams. Further, a fraction of the Probe is picked off and delayed, to form the external Reference beam. The time delay between the alignment Pump and the Probe is denoted by T , while the time delay between the two Gates and the Probe is denoted by τ . The polarization of the alignment Pump is set orthogonal to the Probe using a half-wave plate (HWP). The polarization of the Gate pulses can be rotated to measure different components of the nonlinear response tensor. All beams are focused into a gas cell with room temperature Nitrogen gas at a pressure of 4 bar. The gas cell is ~ 90 mm long, with 1 mm thick UV fused silica (UVFS) windows. The time delay between the alignment Pump and N-DFWM pulses (T) is scanned, while the time delay between the Gate and Probe pulses (τ) is set to zero. In this folded BOXCARS configuration [57], the emitted signal travels in a different direction compared to the other beams, due to phase-matching. The Signal and Reference beams are coupled into the home-built lock-in spectrometer. An optical chopper is placed in the path of the alignment Pump. The experimental setup is shown in figure 1.10.

Drifts in the optical path length between the Reference and the Signal arms of the interferometer lead to fringe instability. Such drifts can be caused by temperature changes, vibrations or air currents. We can model such drifts by adding an arbitrary phase offset ϕ_{arb} to the argument of all the interference terms that contain $\omega\tau$. Although faster drifts (jitter) are efficiently removed by lock-in amplification, slower drifts remain. For a lock-in sampling rate f_s , and number of acquired lock-in samples N , the spectral resolution is f_s/N . For a 1

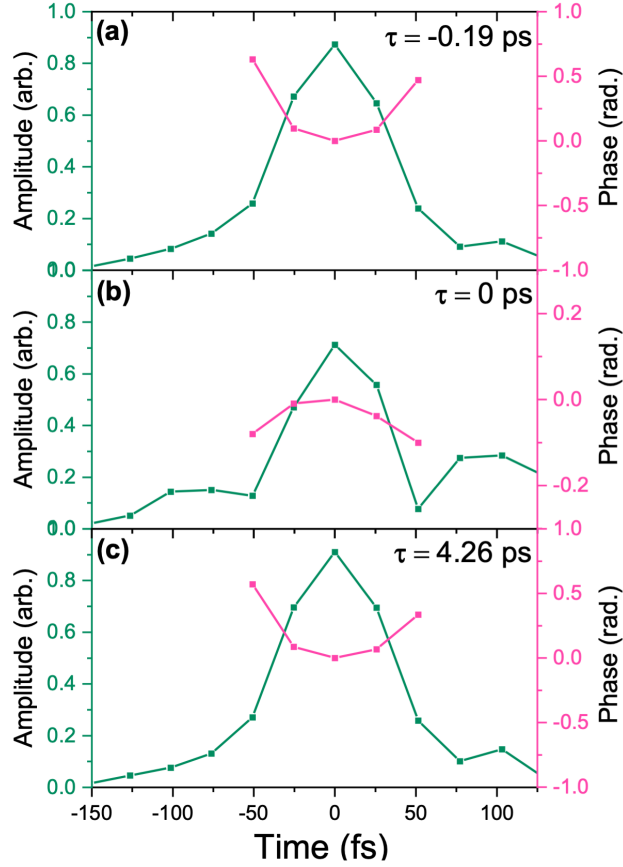


Figure 1.11. Measured signal E-field (amplitude and phase) at three different pump-probe time delays. (a) At negative time delay, the pulse is positively chirped. (b) At pump-probe overlap, the intense pump pulse causes ionization, leading to a negatively chirped signal pulse. (c) At $\tau = 4.26$ ps, when the molecule is anti-aligned, the chirp is lowered.

kHz repetition rate laser, the slowest drift that can be removed by lock-in amplification has frequency:

- 1 Hz with 1 second of data acquisition
- 0.1 Hz with 10 seconds of data acquisition

Usually, such slower drifts are corrected by sending a 'tracer' beam along the path of the interferometer to track phase drifts between the interferometer arms in real time [58]–[61]. Interferometric stability between excitation pulses has been achieved by using lock-in

detection, without introducing an additional tracer beam [62], [63]. However, this technique is not applicable when one of the pulses acts as pump, while the other acts as probe. Lock-in enabled spectral interferometry provides an alternative approach to removing phase drifts. Since the signal and background travel along the same path, any environment-dependent phase drifts will show up in both sets of fringes equally. This can be seen explicitly in figure 1.8 (a). For each delay step, the acquired spectrometer image can be lock-in amplified at both the chopper frequency and 0 Hz, and ϕ_{arb} can be removed by subtracting the phase of the background fringes from that of the signal fringes, without needing active stabilization. Without this phase tracking, the measured N-DFWM signal averages to zero (see figure 1.8 (b)). On the other hand, setting the phase of each measurement to zero at the central wavelength leads to a non-vanishing signal that contains no phase information. To accurately measure the real and imaginary parts of the signal E-field, phase tracking is necessary. In figure 1.11, we show the measured signal E-field amplitude and phase, for three different pump-probe time delays. For negative pump-probe time delays, the phase is positively chirped, while around a rotational revival the chirp modulates [30], [64]. At zero time delay, the negative dispersion caused by free electrons created by the pump leads to a negatively chirped signal pulse [65].

Further, we can estimate the temporal resolution of our spectral interferometry scheme as follows. Let the temporal sampling rate be F_s , and the number of acquired samples in the spectrum be N . Then, the following relations hold

$$\begin{aligned}\Delta\nu &= \frac{F_s}{N} \\ \Delta\tau &= \frac{1}{F_s}\end{aligned}\tag{1.33}$$

Additionally, the spectral resolution in terms of the wavelength is

$$\Delta\nu = \Delta\left(\frac{c}{\lambda}\right) = \frac{c}{\lambda_o^2} \Delta\lambda\tag{1.34}$$

where λ_o is the center frequency of the laser pulse. If the spectrometer covers the entire bandwidth of the laser pulse (λ_{BW}), then $\Delta\lambda = \lambda_{BW}/N$. Then,

$$\Delta\tau = \frac{1}{N\Delta\nu} = \frac{\lambda_o^2}{Nc\Delta\lambda} = \frac{\lambda_o^2}{c\lambda_{BW}} \quad (1.35)$$

In our experiment, $\lambda_o = 810$ nm, and $\lambda_{BW} \approx 80$ nm, giving $\Delta\tau = 27$ fs. This agrees with the experimentally determined temporal resolution.

1.4 Results and Discussion

In our temporal phase-resolved alignment pump-DFWM experiment (see figure 1.12), 60 fs near-infrared (IR) pulses centered around 800 nm are first split and delayed. One arm forms the alignment pump beam and the other is split again into three weaker DFWM probe beams (folded BOXCARS geometry) using a mask. One of the DFWM probe beams is further split to derive a reference pulse. The alignment pump excites a rotational wavepacket which is then probed using the DFWM beams. All four pulses intersect inside a gas cell containing the target gas at room temperature and a pressure of 4 bar, in a non-collinear geometry. The intensity of the pump pulse was estimated from the fitting procedure to be 8 TW cm⁻², while the average intensity of the probe pulses is estimated to be < 4 TW cm⁻². The crossing angles are small enough such that time-smearing is small in comparison to the pulse duration. Time delay (T) between the alignment pump and probe pulses is varied using an optical delay stage. The relative polarization of the pump and probe beams is set to 0°. The emitted nonlinear signal propagates along a separate direction, and is spatially isolated from all other beams using a beam-stop. The emitted signal is passed through a polarizer to remove any ellipticity and coupled into a home-built spectrometer, along with the reference pulse, for spectral interferometry [47]. In our measurements, the DFWM signal from aligned molecules is $\sim 1\%$ of the signal from unaligned molecules. Since both of these travel along the same phase-matched direction, it becomes essential to use lock-in enabled detection, to separate the weak signal from the strong background.

For each pump-probe time delay (T), the measured E-field phase is fit to a 5th order polynomial, as in equation 1.27. The second-order polynomial coefficient a_2 (also known

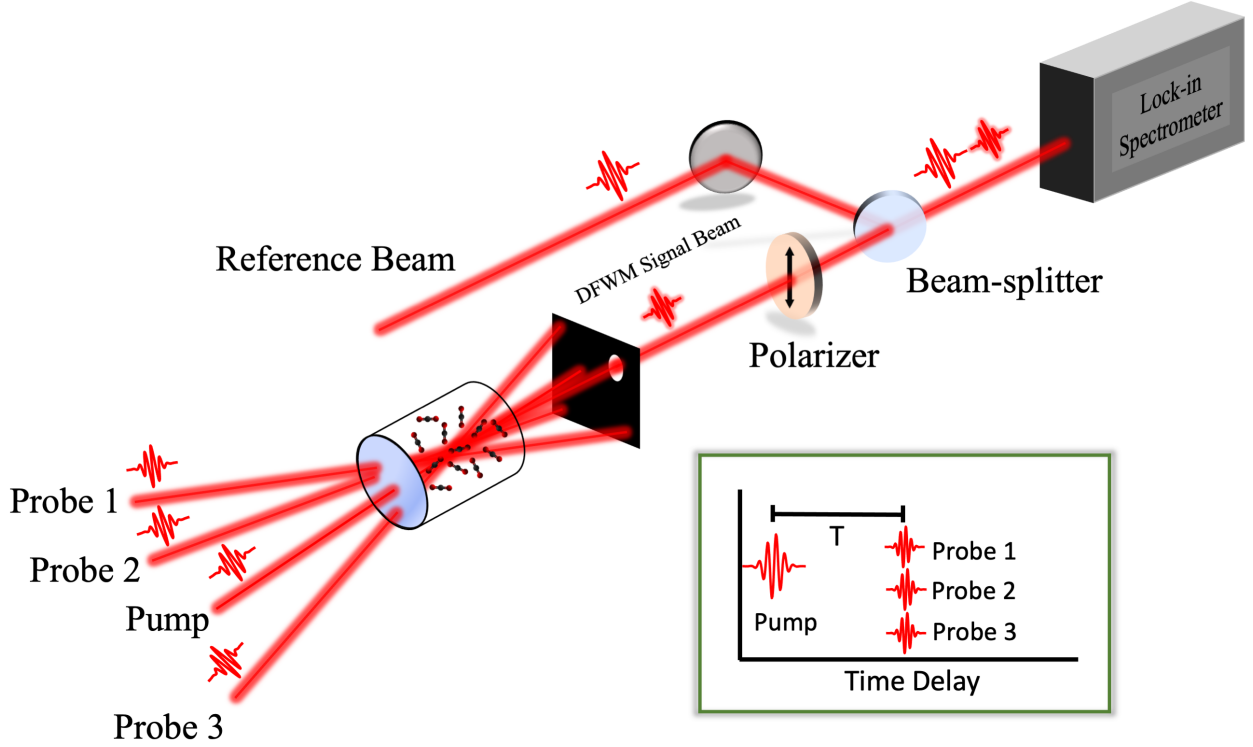


Figure 1.12. Schematic of the experimental setup. The alignment Pump and the time-delayed DFM Probe beams are focused into a gas cell containing the target gas at room temperature and a pressure of 4 bar. The emitted nonlinear signal is spatially isolated, cleaned with a polarizer, and combined with the external reference in a lock-in detection enabled spectrometer. The Reference is separately characterized using a FROG device (not shown).

as chirp), which is the dominant nonlinear fit coefficient, is extracted as a function of the pump-probe time delay (T). Experiments that measure the absolute phase shift of a weak probe passing through pumped media often measure the zeroth-order coefficient $a_0(T)$ in this expansion [24], [66]. Pump-probe studies in gases and solids have previously measured the time delay-dependent frequency shifts [64], [67], which corresponds to the linear coefficient $a_1(T)$. FWM experiments in liquids have also measured the full amplitude and phase of the signal [58], [68]. Such a complete measurement of the emitted E-field phase gives access to both the absolute phase shift and other higher-order terms, especially chirp [18], which is used as the main observable in our study involving gas-phase molecules.

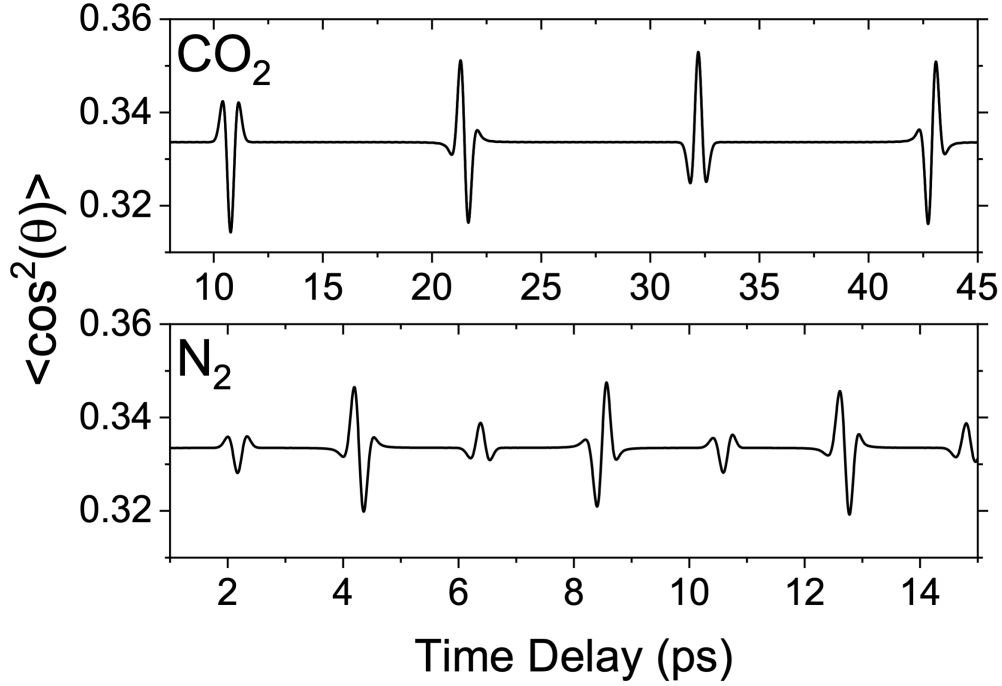


Figure 1.13. Calculated $\langle \cos^2(\theta) \rangle$ of the rotational wavepacket for CO₂ and N₂ molecules. The calculation is done using experimentally determined parameters, and the rotational constants of the molecules available in the literature.

Previous studies have shown that by measuring the photoionization or high-harmonic generation (HHG) yield from a molecular wavepacket as a function of alignment pump-probe time delay, the yield can be retrieved as a function of the relative angle between the pump pulse polarization and the symmetry-axis of the molecule [33], [34], [69]–[73]. This deconvolution method can improve angular resolution when working with molecular ensembles having low degree of alignment, as in our experiment where $\langle \cos^2(\theta) \rangle \sim 0.35$. For obtaining the degree of alignment, we used the pulse parameters obtained from the fits of the chirp, and the rotational temperature of the gas to simulate rotational revivals (see figure 1.13). We perform such an analysis to retrieve the alignment angle-dependence of the nonlinear signal E-field chirp from time delay-dependent measurements. We assume that the chirp of the emitted nonlinear signal is a function of the molecular alignment angle θ . For

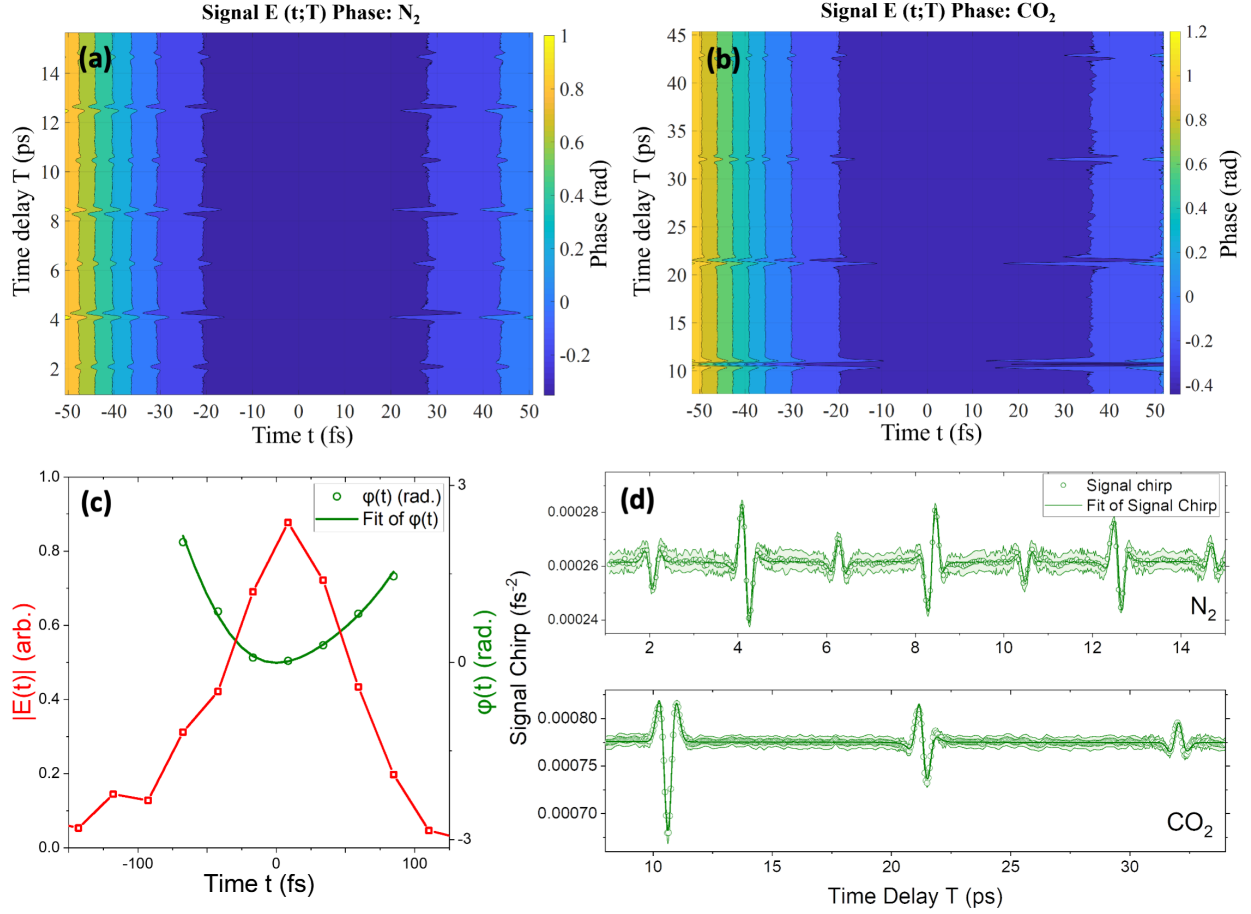


Figure 1.14. (a) Temporal phase of the nonlinear signal E-field from pre-aligned N₂ molecules and (b) from pre-aligned CO₂ molecules, as a function of pulse time (t) and time delay (T). (c) A representative plot of E-field amplitude and phase along with a polynomial fit of the phase. (d) For each pump-probe time delay T , the measured E-field phase is fit with a polynomial in pulse time t . The second-order fit coefficient (chirp) is plotted as a function of T for N₂ and CO₂. The error band represents standard error. The chirp of the input probe pulses is 0.00017 fs^{-2} .

linear molecules interacting with a one-color pulse, inversion symmetry implies $\theta \equiv \pi - \theta$, so we can expand $a_2(\theta)$ in Legendre polynomials as

$$a_2(\theta) = \sum_l c_l P_l(\cos(\theta)) \quad (1.36)$$

with l taking only even values. On taking the expectation value of this equation with the pump-excited rotational wavepacket, the left-hand side becomes the experimentally measured chirp

$$a_2(T) = \sum_j c_j \langle P_j \rangle(T) \quad (1.37)$$

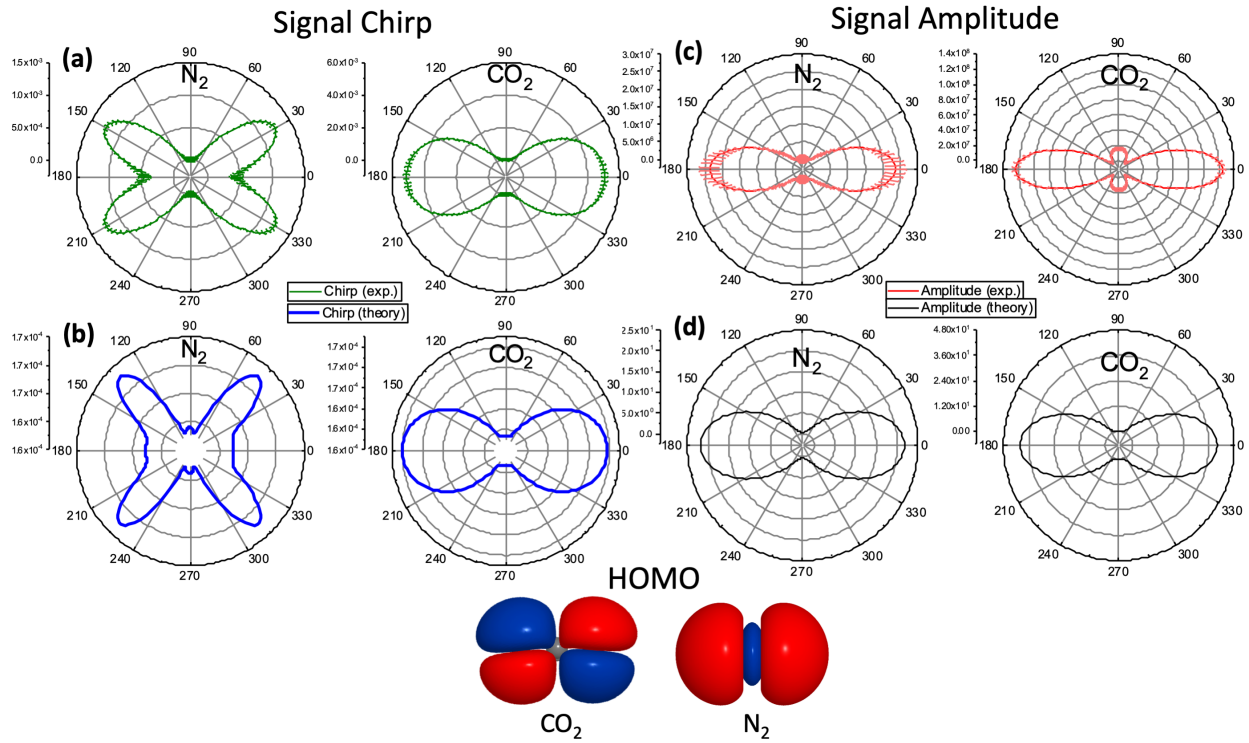


Figure 1.15. (a) Alignment angle-dependent molecular-frame nonlinear signal E-field chirp retrieved from the experimental data, for N_2 and CO_2 . (b) Theoretical calculations of the alignment angle-dependent E-field chirp for N_2 and CO_2 . (c) alignment angle-dependent molecular-frame E-field amplitude (pulse time-integrated). (d) same as (c) from theoretical calculations. Highest occupied molecular orbitals (HOMO) for N_2 and CO_2 molecules, showing their distinct σ and π bonding character, respectively, are shown in the bottom panel for reference. While the molecular frame chirp does not directly correspond to the shape of the HOMOs, the chirp is seen to be distinctly different for the two molecules.

Using a suitable set of pulse parameters for the alignment pump, we simulate the time evolution of the excited rotational wavepacket and calculate the expectation value of the Legendre polynomials on the right-hand side of equation 1.37 which can then be inverted to

find the expansion coefficients c_j (see reference [33], [70] for more details). The rotational temperature of the gas is the same as its thermal temperature (295 K), and the pump pulse duration is measured to be 60 fs using a commercial FROG device. In the fitting procedure, the intensity of the pump pulse in the focal region was allowed to vary within reasonable bounds, from 5 to 40 TW cm⁻². To account for collisional dephasing of the excited rotational wavepacket, we also include a single-exponential decay parameter in the fitting procedure [74]. The measured signal E-field phase, as a function of pulse time (t) and pump-probe time delay (T), is shown in figure 1.14 (a) for N₂ molecules and in figure 1.14 (b) for CO₂ molecules, as contour plots. Figure 1.14 (c) shows a representative plot of the pulse time (t) dependent amplitude and phase of the nonlinear signal for a fixed time delay (T).

In the experiment, 25 independent measurements of the E-field amplitude and phase are made for all time delays (T). For each time delay, the E-field phase is fit with a polynomial in time (t), weighted by the normalized E-field intensity ($|E(t)|^2$). Each measurement then gives a T -dependent chirp ($a_2(T)$), which is averaged over all measurements to get T -dependent mean and standard error values for the chirp. This is then converted to angle-dependent chirp, using the aforementioned fitting procedure. A similar procedure is used for the E-field amplitude integrated over the pulse time (t). To estimate the uncertainty in the chirp we use a Monte Carlo approach. Starting with the mean T -dependent chirp, we generate noisy instances of the T -dependent chirp. The noise is assumed to be normally distributed, with a standard deviation equal to the standard error of the experimentally measured mean chirp. The fitting procedure is repeated for 1000 such noisy instances, from which the mean and standard deviation of the angle-dependent chirp are calculated and plotted. Figure 1.16 graphically shows this error analysis procedure.

Figure 1.14 (d) shows the extracted chirp as a function of T for both N₂ and CO₂ molecules. The alignment angle-dependent chirp in the molecular frame is retrieved by using a fitting and inversion procedure that provides coefficients c_j , as described above. Figure 1.15 (a) shows the molecular-frame chirp of the nonlinear optical signal for N₂ and CO₂ molecules. These experimental chirp plots show distinct angular dependence of the chirp for the two molecules which have different ground state electronic symmetries. The

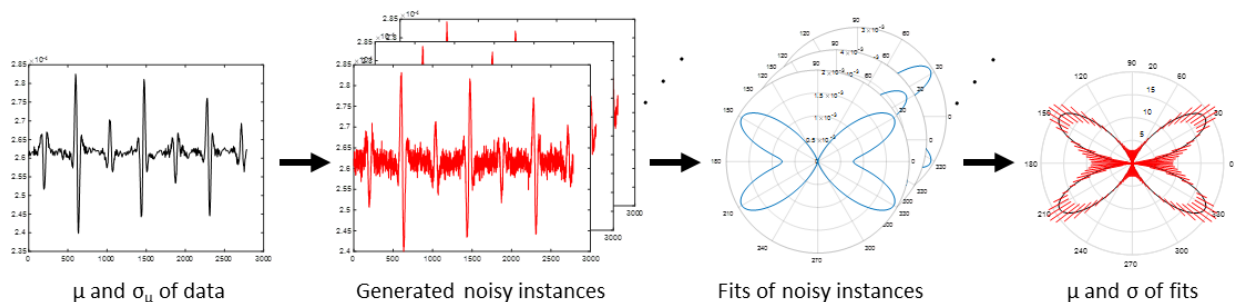


Figure 1.16. Representation of the Monte Carlo uncertainty analysis: For each delay step, the mean and standard error of the experimental data (chirp or integrated amplitude) is used to generate random noisy instances of the T-dependent data. These instances are fit individually, and the retrieved angle-dependence from all these fits are used to generate the mean and uncertainty of the angle-dependence.

corresponding highest occupied molecular orbital (HOMO) for the two molecules are shown in the bottom panel of figure 1.15.

To investigate the origin of the angle-dependent chirp, the nonlinear electronic response of N_2 and CO_2 molecules was calculated using the DFWM pulse sequence used in the experiment. From the calculated signal E-fields, the phase was fit similar to the experimental data, to obtain the calculated molecular-frame angle-dependent chirp for a single molecule. The details of the calculation are provided in Appendix A. The chirp of the calculated signal field, as shown in figure 1.15 (b), shows good agreement with the experimentally determined angle-dependent chirp (figure 1.15 (a)), with minor deviations in the maximal angle likely arising from the coupled-cluster electronic structure methodology (see Appendix A). These calculations support the interpretation that the angle-dependence of the signal chirp observed in our experiment is electronic in origin and that propagation effects of the weak nonlinear signal in the dense target medium are negligible. The low-intensity, non-resonant probe pulses used in this experiment interact perturbatively with the target molecules and the signal predominantly originates from valence electrons. The angular dependence of molecular-frame chirp of the nonlinear signals from N_2 and CO_2 are thus sensitive to the differences in their valence electronic character. Multiple previous studies have measured

and calculated angular dependence of photoionization signals [35], [75]–[78], or emission of HHG light [79]–[81] in aligned molecules. Establishing direct correspondence between the measured angular distribution and the HOMO wavefunction is non-trivial in these studies though molecular orbital tomography has been successful in some cases [82], [83]. In our measurement, we observe sensitivity of the molecular-frame chirp to differences in electronic symmetry in a perturbative all-optical probing scheme, even though a direct correspondence to the shape of the HOMO for the two molecules is not seen.

We perform a similar analysis to retrieve the alignment angle-dependence of the (pulse time-integrated) amplitude of the emitted signal E-field. Figure 1.15 (c) shows that the amplitude of the measured signal is not sensitive to electronic character differences between the two molecules. The corresponding single-molecule theoretical calculations of the amplitude agrees well with the experimental data. This demonstrates that electric field measurement in nonlinear spectroscopy offers new observables such as the chirp that are sensitive to the electronic character and offer information beyond measurement of the intensity of the signal.

Below, we briefly provide an explanation for the difference in sensitivity to electronic symmetries for the chirp and amplitude observables. We start with 1.13 (frequency dependence is not shown), and express all tensor components as complex numbers,

$$|\chi_{zzzz}^{(3)}|e^{i\varphi} = |\gamma_{zzzz}^{(2)}|e^{i\varphi_{zzzz}} \cos^4(\theta) + \frac{3}{2}|\gamma_{zzxx}^{(2)}|e^{i\varphi_{zzxx}} \sin^2(2\theta) + |\gamma_{xxxx}^{(2)}|e^{i\varphi_{xxxx}} \sin^4(\theta) \quad (1.38)$$

which for small phase angles ($e^{i\varphi} \approx 1 + i\varphi$) becomes

$$\begin{aligned} |\chi_{zzzz}^{(3)}| &= |\gamma_{zzzz}^{(2)}| \cos^4(\theta) + \frac{3}{2}|\gamma_{zzxx}^{(2)}| \sin^2(2\theta) + |\gamma_{xxxx}^{(2)}| \sin^4(\theta) \\ |\chi_{zzzz}^{(3)}|\varphi &= |\gamma_{zzzz}^{(2)}|\varphi_{zzzz} \cos^4(\theta) + \frac{3}{2}|\gamma_{zzxx}^{(2)}|\varphi_{zzxx} \sin^2(2\theta) + |\gamma_{xxxx}^{(2)}|\varphi_{xxxx} \sin^4(\theta) \end{aligned} \quad (1.39)$$

In linear molecules, the magnitude of $\gamma_{zzzz}^{(2)}$ is generally larger than any other component of the second-hyperpolarizability tensor, and therefore, the amplitude and phase of the probed third-order response in the frequency domain may be approximated as

$$|\chi_{zzzz}^{(3)}(\theta)| \approx |\gamma_{zzzz}^{(2)}| \cos^4(\theta)$$

$$\varphi(\theta) \approx \varphi_{zzzz} + 6 \left| \frac{\gamma_{zzxx}^{(2)}}{\gamma_{zzzz}^{(2)}} \right| \varphi_{zzxx} \tan^2(\theta) + \left| \frac{\gamma_{xxxx}^{(2)}}{\gamma_{zzzz}^{(2)}} \right| \varphi_{xxxx} \tan^4(\theta) \quad (1.40)$$

It is seen from equations 1.40 that the magnitude of the frequency-domain lab-frame nonlinear response, which is proportional to the amplitude of the measured nonlinear signal, contains only the predominant second hyperpolarizability ($\gamma^{(2)}$) tensor component. Whereas, the frequency dependent phase, which is required to obtain the time-dependent phase (and hence chirp), contains additional terms with multiple tensor components of $\gamma^{(2)}$. This provides a possible explanation for the sensitivity of the molecular-frame nonlinear signal chirp to the valence electronic character while the amplitude shows the same angular behavior for the two linear molecules. Although the amplitude of this nonlinear optical response is well understood, more work is needed to better understand the origins of the phase of these tensor components, and their relation to electronic symmetries.

1.5 Conclusions

Field-resolved ultrafast spectroscopy is emerging as a sensitive approach to measure ultrafast dynamics on femtosecond and sub-femtosecond time scales in various systems. While recent studies have used field-resolved ultrafast measurement in solids [17] and liquids [84], to our knowledge, no previous work has demonstrated temporal phase-resolved perturbative nonlinear spectroscopy in laser excited pre-aligned molecules in the gas phase. In this work, we have shown that the angle-dependence of the measured E-field chirp corresponding to the perturbative electronic nonlinear response in molecules can act as a probe of changes in their valence electronic symmetry, even though a direct correspondence to the shape of the HOMO is not observed. By comparing the angle-dependence of the measured E-field chirp and amplitude, we have found that the phase of the emitted nonlinear E-field can be more

sensitive than the amplitude of the emitted signal, to the electronic symmetry of molecules. Further, we have demonstrated sensitivity of the nonlinear E-field chirp to the electronic character in molecules with poor degree of alignment ($\langle \cos^2(\theta) \rangle \sim 0.35$) at room temperature, in a perturbative interaction not involving ionization, which has not been previously possible. Our experimental data are well-supported by theoretical calculations on the single molecule nonlinear response. A more detailed mechanistic understanding of the heightened sensitivity of E-field chirp to electronic nonlinearities is still needed.

The experiment presented here is a first step towards applying femtosecond electric field measurements to study electronically excited states in atoms, molecules and solids, which opens up the possibility to disentangle complex quantum dynamics in real-time with high temporal resolution. Additionally, the sensitivity of the E-field phase to differences in electronic symmetry, as demonstrated in the present work, provides a tool to study the transient changes in symmetry of electronic states in molecules as they evolve on excited potential energy surfaces. The ability to measure ultraweak fields with zeptojoule energies without delay scanning makes spectral interferometry [47] a suitable candidate for E-field metrology in experiments involving a low-intensity pump, such as a pulse from a HHG source, although direct field sampling has recently been demonstrated at the sub-femtojoule level [84]. In the future, measurement of temporal phase-resolved nonlinear optical signals from electronic states excited by a HHG source could offer new observables not previously accessible for the study of ultrafast dynamics.

2. MEASURING ULTRAFAST DYNAMICS OF VUV-EXCITED MOLECULES

2.1 Introduction

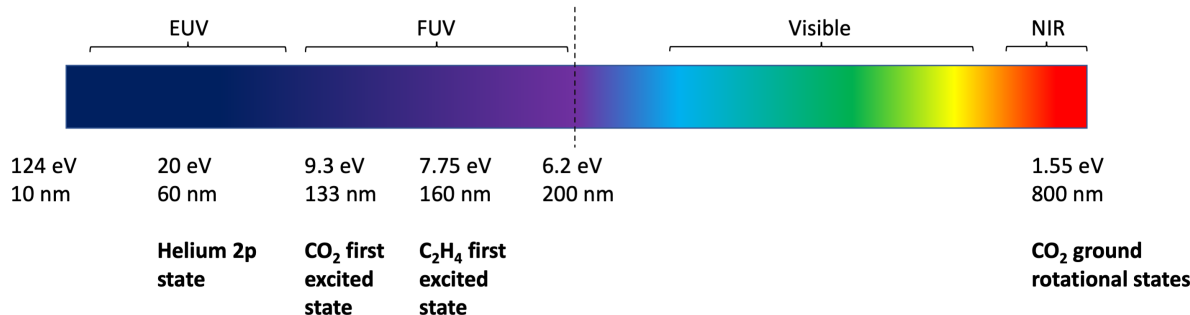


Figure 2.1. UV/Visible spectra showing the resonant wavelengths for a few molecular transitions. Note how some of the most common molecules need vacuum-ultraviolet light for optical excitation.

As we saw in chapter 1, the timescale for rotational dynamics is on the order of many picoseconds, owing to the small energy separation (< 1 meV) between rotational states. Naturally, even faster dynamics involve states separated by a few eV. Typical first excitation energies for some common gases, shown in figure 2.1, put in context the wavelengths of light that are required to excite some common diatomic/polyatomic gases. Polyatomic molecules, like ethylene, when excited to an electronic state with vacuum-ultraviolet (VUV) or extreme-ultraviolet (EUV) light, often relax back to the ground state through radiationless pathways. This generally involves the redistribution of electronic energy to the nuclear degrees of freedom, and only occurs under certain special conditions. Although the field of high-harmonic spectroscopy is well-established, direct measurement of emitted nonlinear E-fields from VUV/EUV-excited molecules is a relatively unexplored direction, ripe with surprises. Extension of our E-field resolved nonlinear spectroscopy techniques to the study of VUV-excited molecules will give new insights into the ultrafast dynamics of such relaxation pathways, where theoretical calculations become computationally intractable. Attosecond/femtosecond EUV/VUV pulses based on nonlinear high-harmonic generation (HHG) form an ideal tool for exciting electronic wavepackets on excited electronic manifolds, and

probing their ensuing ultrafast dynamics. We begin this chapter with a detailed description of the VUV/EUV source that we have developed for studying excited-state dynamics.

2.2 Theory of High-Harmonic Generation

High-harmonic generation can be thought of as a generalization of second-harmonic generation where two photons, say of wavelength 800 nm each, are converted into a single photon of wavelength 400 nm. As we saw in chapter 1, the nonlinear response of a system can be expanded in a perturbative series. Perturbative harmonic generation (for small n), where n^{th} -harmonic generation can be understood as an n^{th} -order process, occurs when the laser intensity is $< 10^{12}$ W cm⁻². However, when the magnitude of the involved electromagnetic fields is large ($\sim 10^{14}$ W cm⁻²), perturbation theory is no longer applicable [85]. This strong-field regime is the birthplace of (non-perturbative) HHG. A heuristic, semi-classical model of HHG was first proposed by Corkum [86]. In this 'three-step model', a very strong linear electric field, from a laser, distorts the binding potential of an atom enough that a bound electron can tunnel out. The now free electron is then accelerated by the laser field. After half a cycle, the electric field switches direction, and the electron is brought back, where it recombines with the parent ion, emitting the excess kinetic plus ionization energies as higher-frequency radiation. For a 35 fs NIR driving laser pulse, focused down to a 200 μ m spot, a minimum pulse energy of ~ 1 mJ is required for HHG to take place.

Since tunneling is a probabilistic event, an electron can tunnel out of the atomic potential at different times, during the laser cycle. So different electrons travel different trajectories, and gain different amounts of kinetic energy before recombining with the parent ion. Thus, a typical HHG spectrum has multiple discrete frequencies in it. Figure 2.2 shows the possible trajectories of an electron in the presence of a linear driving field. Note that only electrons ionized within a small time window actually make it back to the parent ion, and result in HHG. These electrons are the ones that tunnel out of the parent atom close to a zero-crossing of the electric field, and then recombine at the next zero-crossing. Thus, the temporal profile of a typical HHG pulse consists of short bursts synchronized with the driving laser field. We

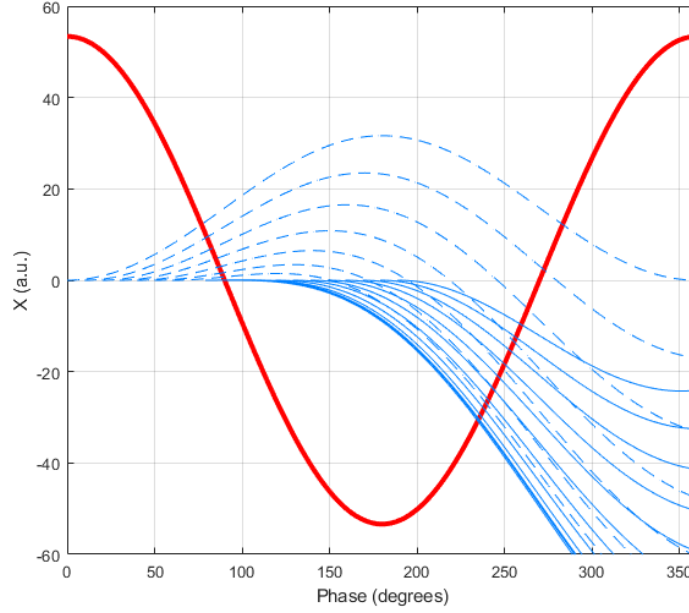


Figure 2.2. Trajectories of electrons after tunneling out of the parent atom. Dotted curves represent trajectories that result in recombination with the parent ion and subsequent HHG, while solid curves show trajectories that do not. A full cycle of the drive laser electric field (red) is superposed.

can see this more clearly by writing the generated radiation as a superposition of higher-order harmonics as

$$E(t) = \sum_{q=q_L}^{q_H} E_q e^{i(q\omega t + \phi_q)} \quad (2.1)$$

where ω is the fundamental (drive laser) frequency, and q_H, q_L are the highest and lowest generated harmonic orders respectively. Assuming w.l.o.g. that their phases and amplitudes are constant

$$E(t) = E e^{i(q_L \omega t + \phi)} \sum_{q=0}^{q_H - q_L} e^{iq\omega t} \quad (2.2)$$

This summation is trivial, and we can get the intensity profile by squaring the electric field

$$I(t) = I_0 \frac{\sin^2 \left(\left(\frac{q_H - q_L}{2} + 1 \right) \omega t \right)}{\sin^2(\omega t)} \quad (2.3)$$

Equation 2.3 is plotted in figure 2.3 for $q_H - q_L = 10$, and clearly shows the attosecond pulse train (APT) that is generated through HHG.

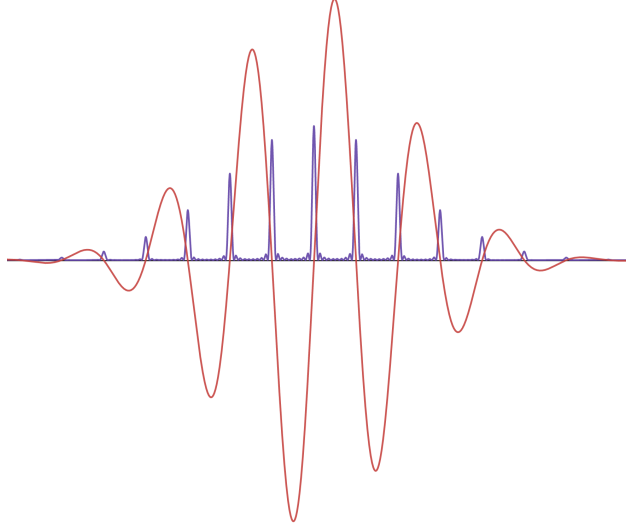


Figure 2.3. Schematic of an attosecond pulse train generated during high-harmonic generation. The radiation is emitted when the accelerated electron recombines with the parent ion, which happens near a zero-crossing of the drive laser electric field.

2.3 Design of High-Harmonic Generation Beamline

In this section, we will discuss the construction of the HHG beamline for producing VUV radiation. A schematic of the beamline is shown in figure 2.4. A Ti:sapphire laser amplifier (Coherent Legend Elite Duo) provides 5 mJ, 35 fs pulses at a laser repetition rate of 1 kHz. A portion of the pulse energy (1 mJ) is split off to form additional NIR beams. The remaining laser power is used for driving HHG. The HHG drive beam hits a mirror with a hole drilled at the center (holey mirror), such that the reflected beam has an annular intensity profile. This intensity profile is useful for subsequent separation of the NIR drive from the generated high-harmonic radiation [87], [88]. The drive beam is focused into a 1" path length gas cell containing argon gas (see figure 2.6), whose Kapton windows are drilled through by the drive beam. The HHG cell is mounted on a motorized linear stage and can be moved along the focus of the drive beam.

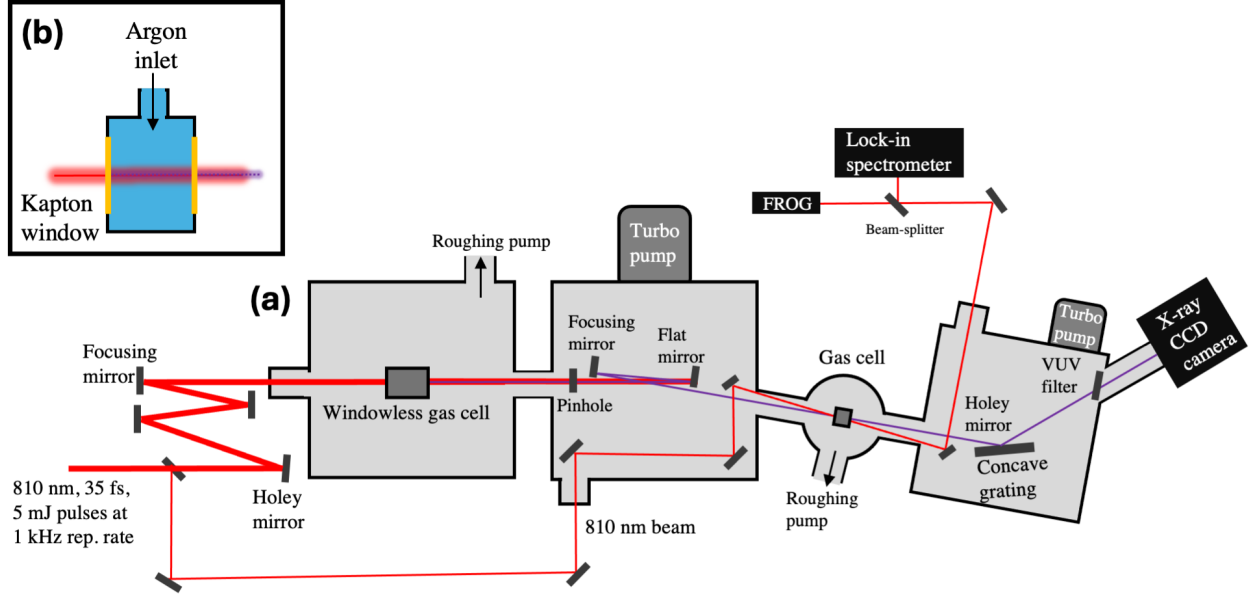


Figure 2.4. (a) Schematic of the HHG beamline. 35 fs wide pulses at a wavelength of 810 nm are derived from a Ti:Sapphire laser amplifier system and focused into an argon gas cell in the first vacuum chamber. The design of the gas cell is shown in (b). In the second vacuum chamber the generated HHG radiation is isolated from the NIR drive using an aperture and special mirrors. Additional NIR beams are combined with the HHG beam, and focused onto the target in the third vacuum chamber. After interaction the HHG beam travels to the last vacuum chamber, where it is dispersed on an X-ray CCD camera using a diffraction grating. The NIR beams are out-coupled from vacuum, and measured using a spectrometer.

Since gas constantly leaks through the laser-drilled holes, good pumping is needed to maintain decent vacuum conditions in the chamber, under gas load. The throughputs of the vacuum pump and the leaking gas cell are

$$\begin{aligned}
 Q_{pump} &= P_{chamber} S_{pump} \\
 Q_{cell} &= (P_{cell} - P_{chamber}) C_{hole}
 \end{aligned}
 \tag{2.4}$$

The P are the pressures of the gas cell and the vacuum chamber. S_{pump} is the flowrate of the vacuum pump, assuming the conductance of the tube connecting the chamber to the pump is infinite. The conductance of the laser-drilled holes in the gas cell are $C_{hole} = 0.1156A$

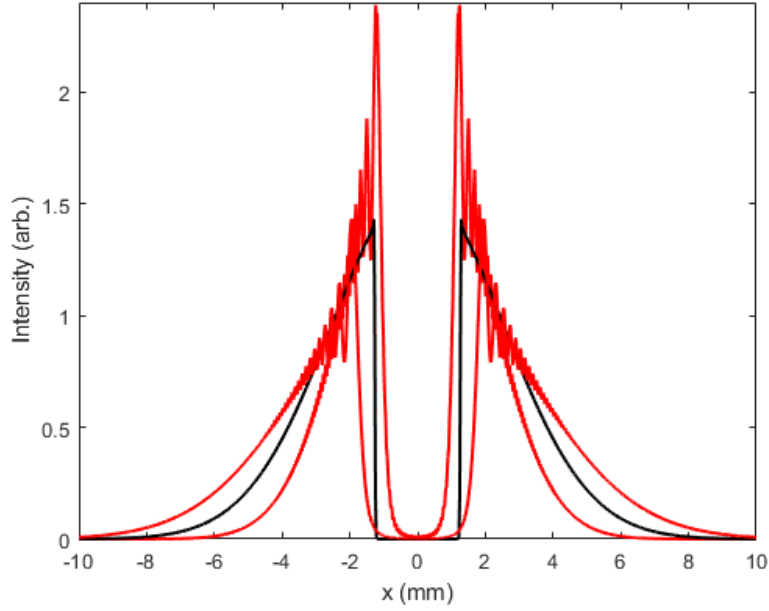


Figure 2.5. Intensity profile of the annular drive beam at the image plane (black) and 200 mm before/after the image plane (red). As a result of diffraction, the central part of the beam starts to gain intensity away from the image plane, making it essential to place the aperture close to the image plane, for optimally rejecting the drive laser.

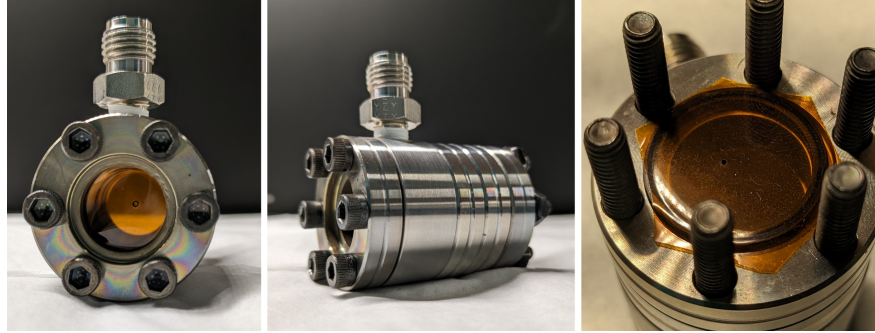


Figure 2.6. Pictures of the argon gas cell, with 0.002" Kapton windows, that are drilled through by the drive beam. Rubber o-rings are used to seal the Kapton windows. The cell is 1" long, and can hold gas at up to 150 torr of differential pressure.

liter/sec, where A is the area of the hole in mm^2 [89]. At equilibrium, the two throughputs are equal, and $P_{\text{chamber}} \approx 0.1156A P_{\text{cell}}/S_{\text{pump}}$.

We can estimate the ambient chamber pressure, for various pumping speeds (in liter-s/sec), assuming 500 μm laser-drilled holes, and a cell pressure of 50 torr:

- $S_{\text{pump}} = 10 \text{ l/s} \rightarrow P_{\text{chamber}} \approx 300 \text{ mTorr}$
- $S_{\text{pump}} = 50 \text{ l/s} \rightarrow P_{\text{chamber}} \approx 60 \text{ mTorr}$
- $S_{\text{pump}} = 100 \text{ l/s} \rightarrow P_{\text{chamber}} \approx 30 \text{ mTorr}$
- $S_{\text{pump}} = 500 \text{ l/s} \rightarrow P_{\text{chamber}} \approx 6 \text{ mTorr}$

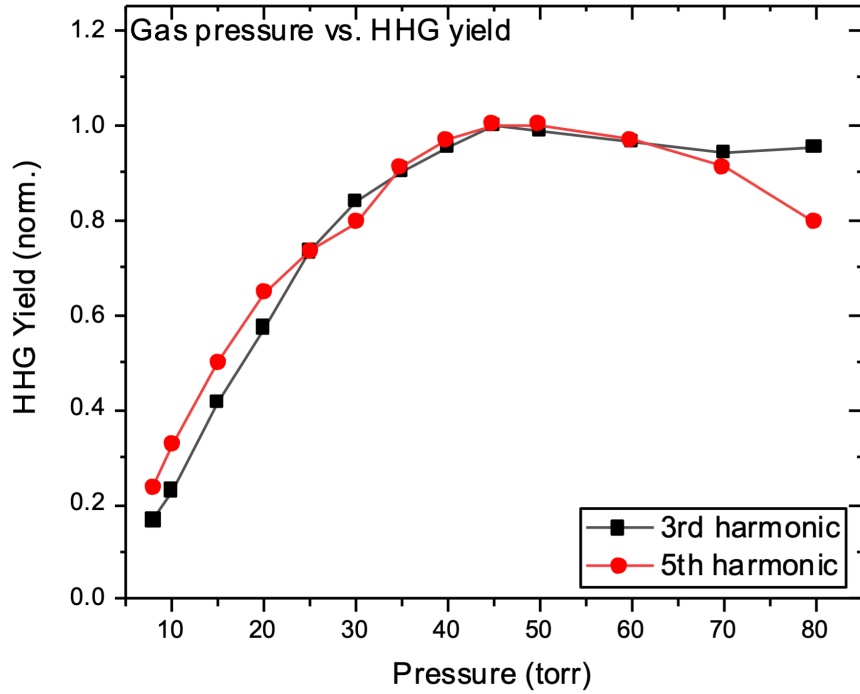


Figure 2.7. VUV and UV harmonic yield as a function of backing pressure in the argon gas cell. The yield reaches a maximum value, after which propagation effects start to affect yield.

HHG yield is maximized when harmonics generated at different points along drive propagation in the generation medium add up coherently. This 'phase-matching' is achieved by optimizing several experimental parameters, such as HHG gas pressure, Guoy phase of the drive beam near the focus, mode quality and intensity of the drive beam, path length in the generation medium etc [85]. Figures 2.7 and 2.8 show the dependence of low-order harmonic

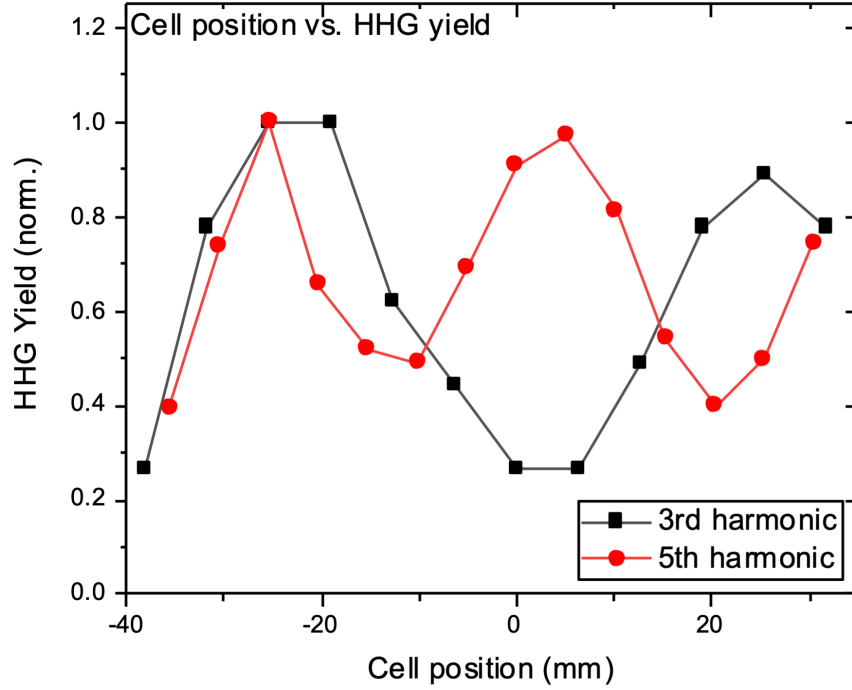


Figure 2.8. VUV and UV harmonic yield as a function of the position of the argon gas cell, relative to the focus of the drive beam. There are two distinct maxima, for when the focus of the drive is either upstream or downstream of the gas cell centre. We use the -25 mm position, to avoid possible drive pulse distortion before harmonic generation occurs.

yield on argon pressure and the cell position relative to the focus of the drive beam (which controls both the drive intensity and the Gouy phase in the focus). Note that the effect of Gouy phase is already reduced in our loose drive focusing ($f = 1.2$ m) geometry. We have found that $\sim 1''$ is the optimal path length for 5th- and 3rd-harmonic generation in our set up.

A differential pumping stage after the first chamber helps reduce the gas load in the rest of the beamline. After the focus, the drive beam expands with an annular intensity profile. The generated high-harmonic radiation has a smaller divergence than the NIR drive, and therefore, is spatially localized at the center of the annular drive beam [90]. The generated high-harmonic radiation travels with the NIR drive to the second vacuum chamber, where a steel aperture blocks most of the drive laser, but allows the high-harmonic beam to pass.

The aperture is placed at the distance where the image of the holey mirror is formed by the focusing mirror. This minimizes the amount of NIR leakage caused by the diffraction spot that develops in the middle of the annular beam as the beam propagates [87]. Figure 2.5 shows the intensity profile of the annular beam at the image plane, and at distances away from it. Additionally, the amount of NIR leakage deviates from ideal conditions due to scattering from the Kapton windows (4x more leakage), and needs to be further filtered.

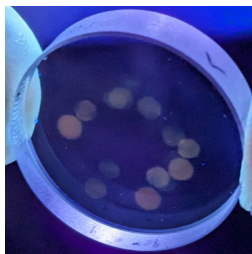


Figure 2.9. Multilayer dielectric mirror that selectively reflects 5th-harmonic, and transmits other frequencies, showing damage from prolonged UV/IR irradiation.

After spatial filtering, the high-harmonic radiation is spectrally filtered using mirrors that have high reflection for a given harmonic order, and high transmission ($> 95\%$) for all other wavelengths. For experiments with VUV, we use (multilayer) dielectric mirrors by Layertec GmbH, to filter and focus the VUV beam onto the target. The mirrors are arranged in a z-fold configuration, with the first mirror flat and the second mirror concave. The angle of incidence at the curved mirror is kept as small as possible to reduce spherical aberration. Over time, these mirrors develop burnt spots due to UV/IR irradiation (see figure 2.9), which leads to reduced reflectivity. However, plasma cleaning successfully cleans the mirrors and restores their performance.

The design of the beamline also allows for use of a grazing incidence toroidal mirror instead of the z-fold configuration, when multiple harmonic orders with energies up to 400 eV are required. Figure 2.10 shows the reflectivity of a grazing incidence mirror coated with bare Nickel, for a 5° angle of incidence. In both the geometries, the harmonic beam gets deflected at a small angle and is focused onto the target. For probing HHG-excited molecules, an additional NIR probe beam is focused and overlapped with the VUV beam at

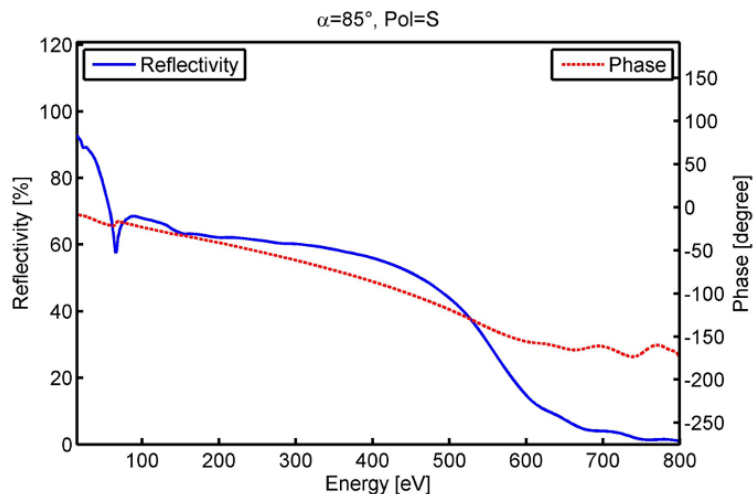


Figure 2.10. Frequency-dependent reflectivity of bare Nickel for 5° angle of incidence. The reflectivity is even higher for smaller incidence angles.

the target position using a frosted YAG crystal (MSE Supplies). A camera equipped with a 400 nm filter is used to image the fluorescence produced by the harmonic (resonant) and NIR (multiphoton) beams for spatial overlap. Temporal overlap between the NIR probe beam and the residual NIR leakage in the drive beam are done using a BBO crystal in the focus.

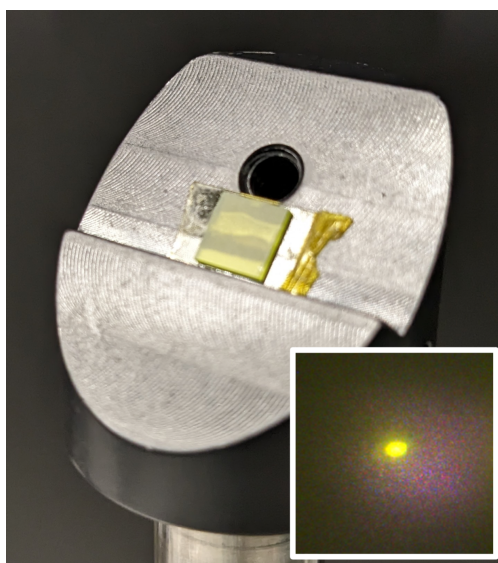


Figure 2.11. Frosted YAG crystal used for spatially overlapping the VUV and NIR beams in the focus. Inset shows fluorescence from the focal spot of the 5th-harmonic beam.

The target in the experiments can either be a solid sample or a gas cell with Kapton windows that are drilled-through by the strong NIR probe beam (see figure 2.12). We use a home-built vacuum feed-through to move the solid sample or a gas cell in and out of the target position. After interaction with the gas, the NIR beams are picked off using a holey mirror, while the harmonic beam passes through the hole in the mirror. The out-coupled NIR beams can be used for NIR measurements out of vacuum, as discussed in chapter 1. The harmonic beam is dispersed by a diffraction grating, and the resulting spectrum is imaged on an X-ray CCD camera (PIXIS XO 400B). In the spectrometer chamber, the CCD camera is mounted at a total deflection angle of 120° relative to the direction of the incoming beam. To calibrate the spectrometer, we start with the grating equation

$$\sin(\alpha) + \sin(\beta) = -mN\lambda \quad (2.5)$$

where m is the diffraction order (commercial gratings are optimized for $m = 1$), N is the groove density in lines/mm, λ is the wavelength in mm.

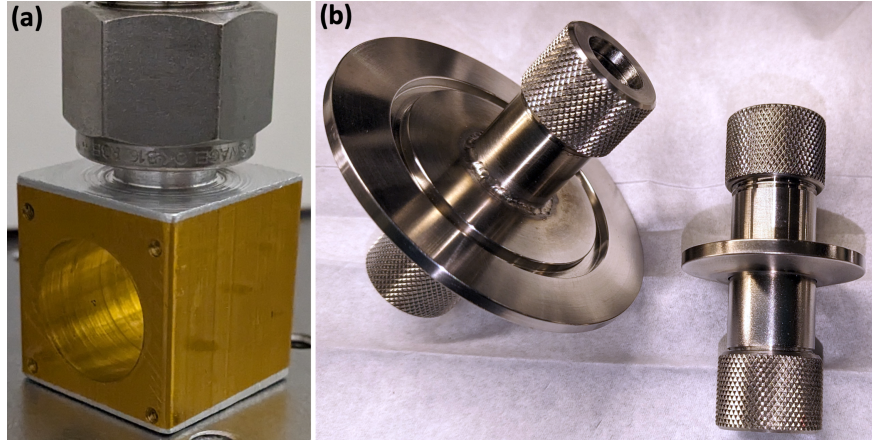


Figure 2.12. (a) Target gas cell with thin Kapton windows. (b) Two custom-made vacuum feed-throughs consisting of two $\frac{1}{2}$ inch quick-connect couplings welded on either side of KF flanges.

For our diffraction grating with groove density $N = 2400$, we can solve the grating equation for $\lambda = 162$ nm, by setting $\alpha + \beta = 120^\circ$. This gives $\beta = 37.1^\circ$.

The spectral dispersion of the grating can be found by differentiation

$$dx \approx f d\beta = \frac{-f N d\lambda}{\cos(\beta)} \quad (2.6)$$

where dx is the linear dispersion on the CCD, and f is the distance from the grating to the CCD, both in mm.

Additionally, wavelength (in nm) and energy (in eV) are related by $E = 1240/\lambda$, and we can get an analogous expression by differentiation

$$dE = \frac{-1240 \cdot d\lambda}{\lambda^2} \quad (2.7)$$

Finally,

$$dE = \frac{1240 \cdot 10^6 \cdot dx \cos(\beta)}{f N \lambda^2} \quad (2.8)$$

where dE is in eV, and λ is in nm. This equation allows us to map pixel number on the CCD to energy, for our spectrometer configuration

$$E [\text{eV}] = 7.66 - 0.028 \Delta x \quad (2.9)$$

The calibrated spectrum of the generated VUV (5th-harmonic) is shown in figure [2.13](#) and gives an estimated (bandwidth-limited) pulse duration of 18 fs. To collect the maximum amount of VUV on the CCD, the spectrometer is used without an entrance slit. To estimate the spectral resolution we can use the criterion that the minimum linear distance between two resolvable wavelengths equals the e^{-2} spot size of the VUV beam on the CCD, which is $\sim 60 \mu\text{m}$. The estimated resolution is 1.68 meV.

2.4 Results and Discussion

Most molecular dynamics are assumed to be amenable to the Born-Oppenheimer approximation, where the nuclear degrees of freedom (DoF) are assumed to be frozen on the

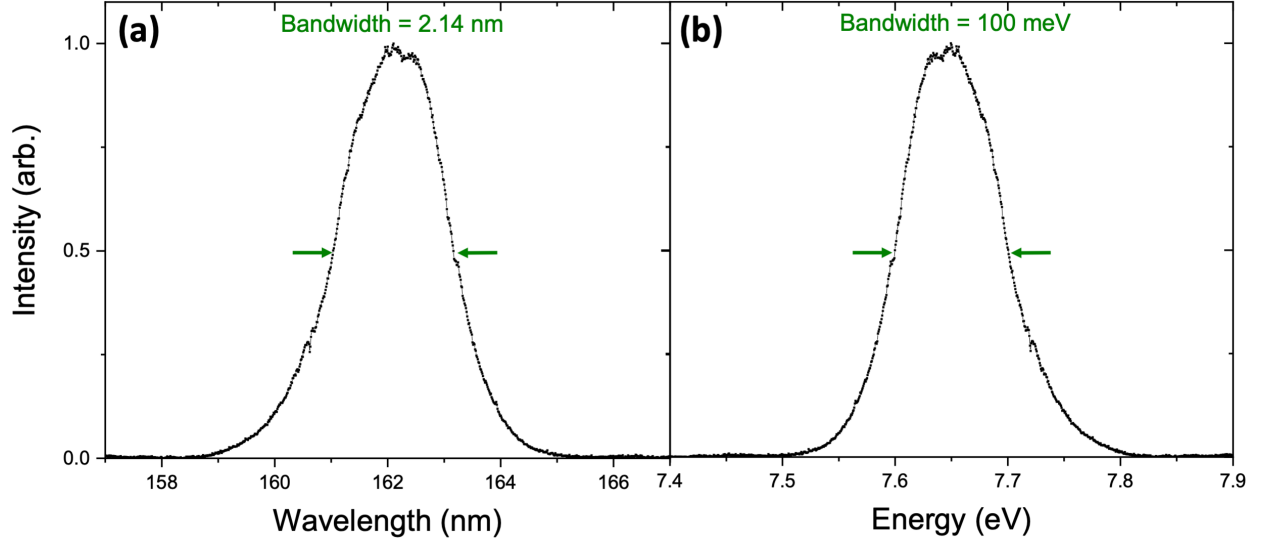


Figure 2.13. Calibrated 5th-harmonic spectrum, as a function of (a) wavelength, and (b) energy. The center wavelength (energy) of the harmonic is about 162 nm (7.66 eV).

timescales of electronic motion. The wavefunction is assumed to be separable in the nuclear and electronic coordinates

$$\Psi(\vec{x}) = \psi(\vec{r}; \vec{R}) \cdot \chi(\vec{R}) \quad (2.10)$$

and satisfies the full Schrodinger's equation

$$H\Psi = \left[H_{nuc}(\vec{R}) + H_e(\vec{r}; \vec{R}) \right] \Psi = E\Psi \quad (2.11)$$

One then simply treats the nuclear DoF as a static parameter and solves the electronic part of the Hamiltonian, with the electronic DoF as dynamic variables

$$H_e(\vec{r}; \vec{R})\psi(\vec{r}; \vec{R}) = E_e(\vec{R})\psi(\vec{r}; \vec{R}) \quad (2.12)$$

and the nuclear wavefunction is solved using

$$\left[H_{nuc}(\vec{R}) + E_e(\vec{R}) \right] \chi(\vec{R}) = E \cdot \chi(\vec{R}) \quad (2.13)$$

This leads to the concept of potential energy surfaces (PES) as usually seen in the literature. This is a very simplified picture, however, and to accurately model molecular dynamics one needs to consider a linear combination of such wavefunctions

$$\Psi(\vec{x}) = \sum_I \psi_I(\vec{r}; \vec{R}) \cdot \chi_I(\vec{R}) \quad (2.14)$$

When a non-separable wavefunction of this form is plugged into the full Schrodinger equation, additional 'vibronic coupling' terms emerge that mix the various electronic states

$$\left[H_{nuc}(\vec{R}) + E_e^I(\vec{R}) \right] \chi_I(\vec{R}) - \frac{1}{\mu} \sum_{I \neq J} \vec{f}_{IJ}(\vec{R}) \cdot \nabla \chi_J(\vec{R}) = E \cdot \chi_I(\vec{R}) \quad (2.15)$$

As two PES come closer and closer, the characteristic timescale of the electronic dynamics get longer and longer, until it becomes comparable to the slower nuclear dynamics. The vibronic coupling term can be written as [91]

$$\vec{f}_{IJ}(\vec{R}) = \frac{\langle \psi_I | \nabla H_e | \psi_J \rangle}{E_e^J - E_e^I} \quad (2.16)$$

and becomes stronger near electronic level crossings. The Born-Oppenheimer approximation then starts to fail, and electronic dynamics start to affect nuclear dynamics. One classic example is the Jahn-Teller distortion, where electronic energy is minimized when the molecular geometry is slightly distorted, due to coupling of the vibrational normal modes to the electronic Hamiltonian [92]. The Jahn-Teller distortion results in two degenerate electronic states having a level crossing. This coupling between electrons and nuclei may lead to the formation of a conical intersection (CI) between PES, which provides an efficient pathway for radiation-less decay between electronic states [93].

For a CI to occur, the energies of two electronic states must become equal. Therefore, in some basis, the Hamiltonian governing this subspace (say with states $|1\rangle$ and $|2\rangle$) must have vanishing off-diagonal elements ($H_{12} = H_{21} = 0$) and equal diagonal elements ($H_{11} = H_{22}$). Satisfying these conditions requires two constraints to be satisfied, and therefore CI can only occur in polyatomic molecules. For instance, CO_2 has two C-O bond lengths and one O-C-O

Table 2.1. Magnitude of the $\gamma_{xxyy}^{(2)}$ in CO₂ for the ground and excited states, calculated using DALTON software package [94]. The values are tabulated as a function of one of the C-O bond lengths, while the other C-O bond length is kept fixed at 2.2 a.u. This corresponds to an asymmetric stretch of the molecule, with $C_{\infty v}$ symmetry. Blank cells indicate that the calculation did not converge.

C-O bond length (a.u.)	Σ^+	Δ	Π
2.3	13	178	746
2.5	13	160	1296
2.7	13	1767	13346
2.85		499660	
2.9	13		3155
3.1	12	2506	4806
3.3	10	24	109

bond angle, leading to a 1-dimensional CI as depicted in figure 2.14. Table 2.1 shows the magnitude of the second-hyperpolarizability component $\gamma_{xxyy}^{(2)}$ for the CO₂ molecule, calculated as a function of the C-O bond length. The calculation was done using the DALTON software package [94]; further details are discussed in Appendix B. Note that when the C-O bond length is close to 2.85 a.u., the calculation diverges or does not converge, indicating the presence of a CI.

The probability that a wavepacket travelling on an excited state $|1\rangle$ decays to a lower energy state $|0\rangle$ through a level crossing is given by [95]

$$1 - \frac{\tau^2}{\hbar^2} \left[\langle 1 | \bar{H}_e^2 | 1 \rangle - \langle 1 | \bar{H}_e | 1 \rangle \langle 1 | \bar{H}_e | 1 \rangle \right] \quad (2.17)$$

where \bar{H}_e is the time-averaged electronic Hamiltonian, and τ is the time the wavepacket takes to traverse across the CI. Note that the states $|0\rangle$ and $|1\rangle$ are the initial (time-independent) states, and can be expressed in terms of a time-dependent basis that diagonalizes the (time-dependent) Hamiltonian

$$\begin{aligned} |0\rangle &= \cos \alpha |-\rangle + \sin \alpha |+\rangle \\ |1\rangle &= -\sin \alpha |-\rangle + \cos \alpha |+\rangle \end{aligned} \quad (2.18)$$

where α is a function of $\vec{R}(t)$. Then, the probability of radiation-less decay becomes

$$1 - \frac{\tau^2}{\hbar^2} (E_1 - E_0)^2 (\overline{\cos \alpha})^2 (\overline{\sin \alpha})^2 \quad (2.19)$$

where $\overline{\cos \alpha}$ and $\overline{\sin \alpha}$ are time-averaged values. Thus, as the speed of traversal increases ($\tau \rightarrow 0$), or the states become degenerate ($E_1 \rightarrow E_0$), the probability of a non-adiabatic transition approaches unity. The vibronic coupling is responsible for mixing the electronic states $|0\rangle$ and $|1\rangle$. An excited wavepacket can traverse a CI multiple times, gradually decaying to the ground state until the wavepacket has fully decayed [96].

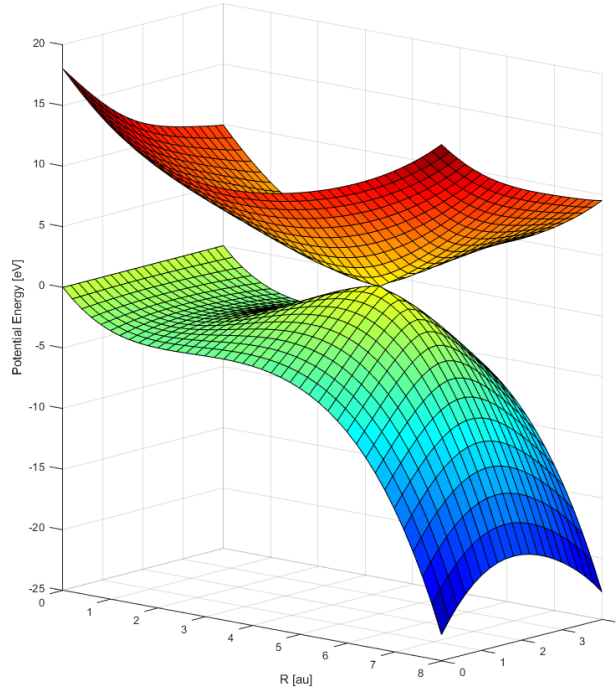


Figure 2.14. Schematic of a 1-dimensional conical intersection (CI) between two potential energy surfaces. When a wavepacket traveling on the higher-lying state traverses the CI, part of the wavepacket can disperse onto the lower-lying state, leading to radiation-less decay.

High-harmonic sources have been the favored tool for studying CIs in excited molecules [97]–[100]. Our HHG beamline was built to probe ultrafast dynamics near a CI, using both VUV/EUV transient absorption (TA) spectroscopy, and VUV-IR FWM.

2.4.1 VUV Transient Absorption Spectroscopy

We performed VUV transient absorption spectroscopy (TAS) in gas-phase CO_2 , which has an absorption cross section of 0.1 Mb at 162 nm [101]. In these experiments, the role of the pump/probe is played by either the VUV or the NIR pulse, depending on their relative time delay. Fluctuations in the VUV yield, however, are large enough that appropriate normalization is necessary to bring the signal level above the noise floor. Unlike the FWM experiments discussed in chapter 1, lock-in detection cannot be readily applied here because the harmonic flux is too low, and the acquisition window needs to be 30-70 ms long. Instead, we employ multi-shot normalization, as is usually done in TAS. We acquire the CCD spectrum for 70 ms with the NIR beam present, and for another 70 ms with the NIR beam blocked. The time delay-dependent absorbance of the VUV is then calculated as

$$OD(E, \tau) = -\log_{10} \left[\frac{I_{VUV+NIR}(E, \tau)}{I_{VUV}(E)} \right] \quad (2.20)$$

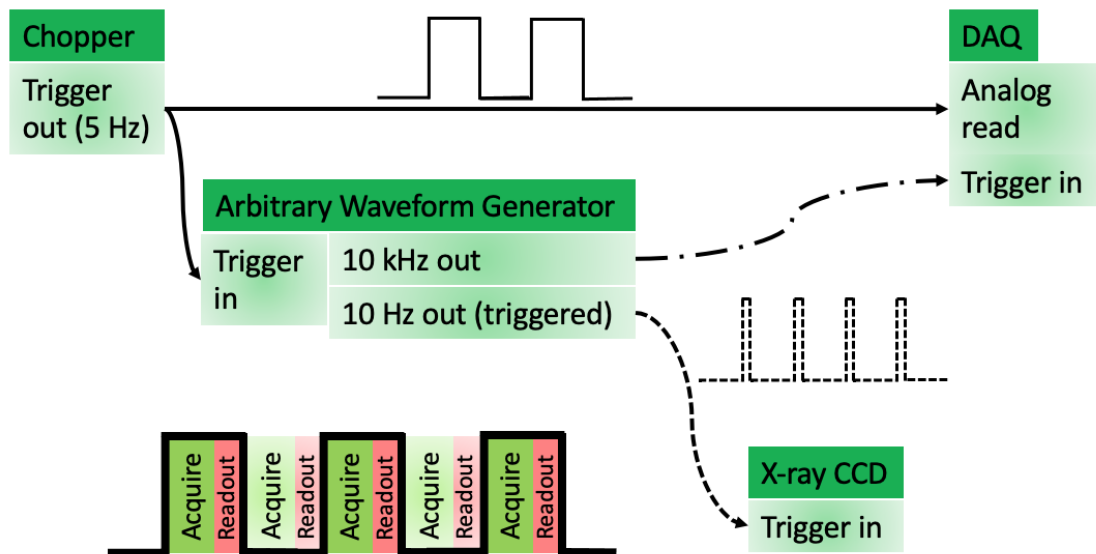


Figure 2.15. Timing diagram of transient absorption spectroscopy (TAS). The NIR beam is blocked/unblocked using an optical chopper, and consecutive NIR ON and NIR OFF frames are recorded using an X-ray CCD triggered by the chopper edge.

Usually, a fast shutter is used to block the NIR pulse to acquire the VUV-only spectrum for normalization. We use an optical chopper in the path of the NIR beam instead, to accomplish the same result. The optical chopper is set to a frequency of 5 Hz, such that the NIR beam is blocked/unblocked every 100 ms. The chopper is used to trigger the CCD camera every time the chopper trace has a rising/falling edge. The chopper trace is recorded using the DAQ to correctly label the NIR ON and NIR OFF frames, and the acquired spectra are then divided and averaged to find the absorbance according to equation 2.20. The timing diagram is shown in 2.15.

The VUV-NIR delay is controlled using an optical delay stage, and 10-20 ON/OFF frames are collected per delay step and averaged. A single experiment consists of multiple such averaged measurements, taken by scanning the entire delay range multiple times. There are two main sources of noise in the experiment – laser intensity fluctuations (σ_{laser}) and CCD read-out noise (σ_{read}). The SNR can be improved by choosing the optimal CCD exposure time and the number of frames averaged. Let SNR_1 be the signal-to-noise ratio when a single ON/OFF measurement is done by acquiring N laser shots. Let SNR_n be the signal-to-noise ratio when n ON/OFF measurements are done, each one by acquiring N/n laser shots. Then, the following relation holds true

$$\frac{SNR_n}{SNR_1} = \frac{\sqrt{n} \sigma_{laser} + \sigma_{read}/\sqrt{n}}{\sigma_{laser} + \sigma_{read}} \quad (2.21)$$

Thus, when harmonic yield fluctuations are the dominant noise source, multiple averages improve the SNR, but when read-out noise is the dominant source, a longer CCD exposure time is better. We conducted TAS experiments in gas phase CO_2 , by measuring VUV absorption as a function of the relative time delay between the VUV and NIR pulses. In the focus, the peak NIR intensity was 30 TW cm^{-2} , and the estimated peak VUV intensity was $\sim 0.1 \text{ GW cm}^{-2}$. The VUV and NIR beams were co-polarized. Figure 2.16 and ?? show the results of these experiments. The time delay is positive when the NIR pulse comes before the VUV pulse, and negative when the VUV pulse comes before the NIR pulse.

Figure 2.16 (b) shows the TA spectrum, around VUV-NIR temporal overlap. There are two distinct absorption features at 7.6 eV and 7.73 eV. Time delay-dependent cuts at these

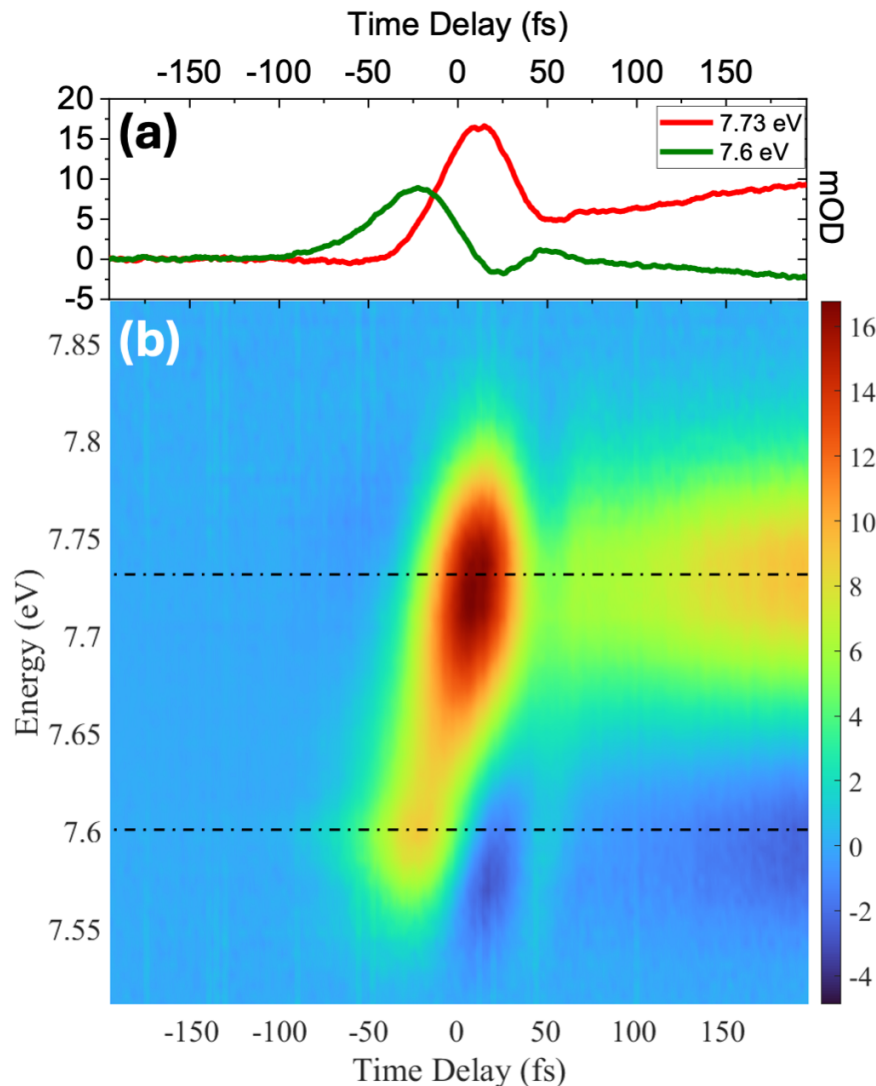


Figure 2.16. (b) VUV transient absorption (TA) spectrum, in CO_2 , around VUV-NIR temporal overlap. About zero time delay, the absorption maximum shifts from 7.6 eV to 7.73 eV. (a) Time delay-dependent cuts at 7.6 eV and 7.73 eV.

energies are shown in 2.16 (a). At 7.73 eV, there is strong absorption (around ~ 10 fs) when the NIR pulse comes first. At the same time delay, absorption at 7.6 eV is suppressed. On the other hand, absorption at 7.6 eV is stronger (around ~ -25 fs) compared to that at 7.73 eV, when the VUV pulses comes first. Possibly, the strong NIR pulse excites CO_2 to a rovibrational level on the ground electronic manifold, from which absorption at 7.6 eV is

prohibited by selection rules. Additionally, as we have seen in figure 1.6, CO₂ develops a strong rotational response that peaks around 175 fs after NIR pumping. For time delays > 100 fs, a similar behaviour can be seen in figures 2.16 (a, b). There is increased absorption at 7.73 eV, and decreased absorption at 7.6 eV for these time delays. This suggests that the transition at 7.73 eV is a parallel transition, while the one at 7.6 eV is a perpendicular transition.

To further understand the symmetry of these states better, we can also study TA of a rotational wavepacket. Figure 2.17 (c) shows the TA spectrum, when the NIR pulse comes much early, and initiates a rotational wavepacket. The time delays correspond to a half revival in CO₂. Again, there are two distinct absorption features at 7.6 eV and 7.73 eV. Time delay-dependent cuts at these energies are shown in 2.17 (b), and the calculated degree of alignment for CO₂ is shown in figure 2.17 (a). Note how absorption at 7.73 eV is increased when the molecule is aligned along the VUV polarization, but decreased at 7.6 eV. Similar results have been previously reported [102], where they were attributed to parallel and perpendicular electronic transitions.

Above 100 nm, CO₂ shows three dominant absorption features [105]:

1. A stronger band around 112 nm (11 eV) due to the Rydberg state $^1\Sigma_u^+$
2. A weaker band around 133 nm (9.3 eV) due to the $^1\Pi_g$ state
3. An even weaker band around 148 nm (8.4 eV) due to the $^1\Delta_u$ state

These absorption bands correspond to vertical transitions between the ground state and excited states of the linear CO₂ molecule (with $D_{\infty h}$ symmetry). Although a linear CO₂ does not have any electronic states below 8 eV, absorption can take place if the OCO bending angle decreases below 170° [105]–[109]. Due to the Renner-Teller effect, highly excited vibrational modes can lead to such a bent CO₂ geometry (with C_{2v} symmetry) [107]. A bent geometry lowers the excited electronic state energies, and the $^1\Delta_u$ and $^1\Pi_g$ states split into A' and A'' states. Figure 2.18 (a) shows the absorption cross-section of CO₂ in the 7.5-7.8 eV range. The Born-Oppenheimer and Franck-Condon approximations are expected to fail in this spectral region, possibly resulting in non-vertical transitions [107], [108]. This makes ground-to-

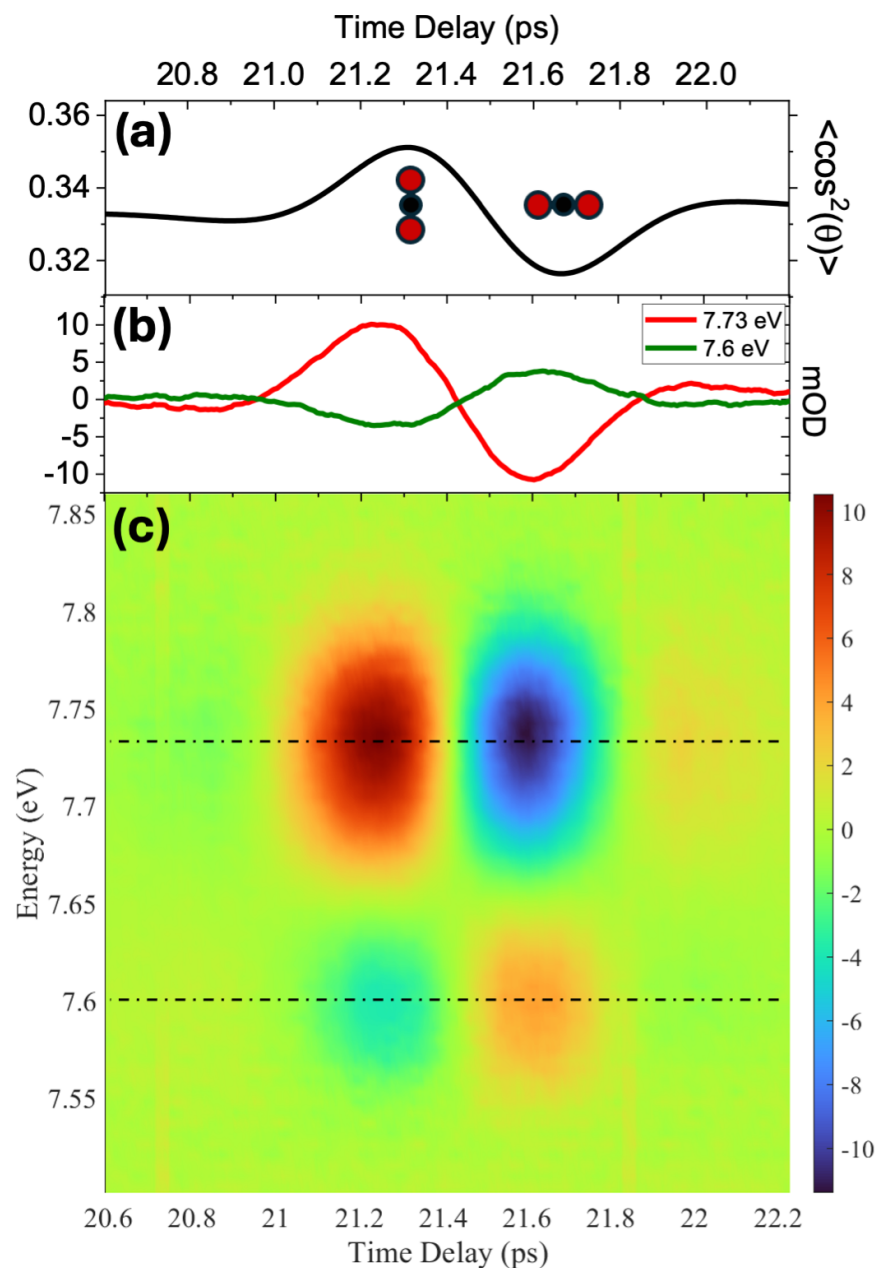


Figure 2.17. (c) VUV transient absorption (TA) spectrum around the half revival in CO_2 . (a) Calculated degree of alignment. The molecule is aligned along the VUV polarization when $\langle \cos^2\theta \rangle > 0.33$, and anti-aligned when $\langle \cos^2\theta \rangle < 0.33$. (b) Time delay-dependent cut at 7.73 eV showing that the absorption is maximized (minimized) when the molecule is aligned (anti-aligned) to VUV polarization. The cut at 7.6 eV shows the opposite trend.

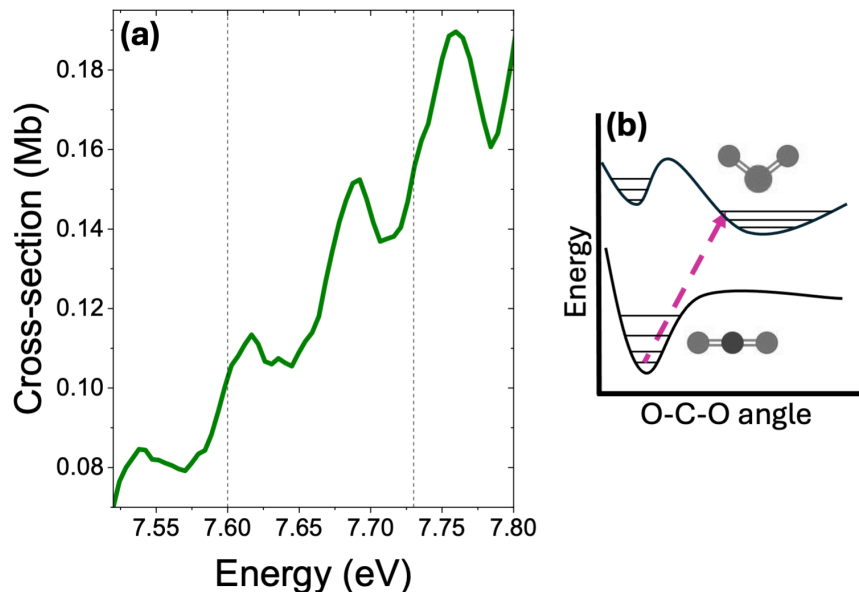


Figure 2.18. (a) Measured absorption cross-section of CO₂ from references [103], [104]. Raw data was retrieved from www.cfa.harvard.edu/amp/ampdata/co296/co2.html. (b) Schematic of a non-vertical transition from a linear to a bent CO₂ geometry.

excited transitions $^1\Sigma_g^+ \rightarrow A'$ and $^1\Sigma_g^+ \rightarrow A''$ possible which are expected to be parallel and perpendicular, respectively [105], [107], [109]. Although these could possibly explain the 7.73 eV and 7.6 eV features, detailed theoretical work is needed to correctly identify these states.

2.4.2 VUV-NIR Four-Wave Mixing

In this section, we discuss progress towards probing dynamics of VUV-excited molecules by measuring their nonlinear optical response. Recent FWM experiments involving a harmonic pump have demonstrated state-selective probing of molecular dynamics [110], [111]. In these experiments individual quantum pathways were separated, according to their specific phase-matching conditions, providing a background-free probe of nonlinear response. These experiments are parametric, in that the target molecule is left in the ground state after signal emission. Correspondingly, the emitted FWM signal is in the EUV, making advanced metrology schemes, like spectral interferometry, challenging. Alternatively, one

can devise a scheme where the nonlinear interaction leads to emission of signal in the NIR. This, if achieved, will make it possible to conduct a temporal phase-resolved measurement on emitted signals from electronically excited molecules. The energy level and double-sided Feynman diagrams illustrating such an experiment are shown in figures 2.19 (b, c). To have signal emission in the NIR, the target molecule must be left in an excited state, making this scheme non-parametric. The phase-matching condition is $k_{\text{signal}} = k_{\text{NIR}} + k_{\text{VUV}} - k'_{\text{VUV}}$. Similar to figure 1.2, two experimental geometries are possible, corresponding to $k_{\text{VUV}} = k'_{\text{VUV}}$ and $k_{\text{VUV}} \neq k'_{\text{VUV}}$.

When $k_{\text{VUV}} = k'_{\text{VUV}}$, the signal is emitted along the probe beam. When the VUV is polarized at 45° relative to the probe polarization, signal proportional to $\gamma_{xxyy}^{(2)}$ will have orthogonal polarization relative to the probe, and can be isolated using a polarizer.

When $k_{\text{VUV}} \neq k'_{\text{VUV}}$, the signal is emitted offset from the probe beam, and can be detected background-free. A mask can be put in the path of the VUV beam, before focusing, to form two collinear VUV beams that overlap on the target. The larger divergence of lower-order harmonics (VUV/UV) makes this experimentally feasible.

Preliminary measurements were done on solid samples, using an 810 nm (fundamental) + 270 nm (3rd-harmonic) + 162 nm (5th-harmonic) pump, and NIR (810 nm) probe. To distinguish excited-state dynamics resulting from the various pump wavelengths, a 500 μm CaF₂ delay window was placed in the path of the harmonic beam before interaction. The CaF₂ window has a >80% transmission for all pump wavelengths, and delays different harmonics by different amounts [112]. Figure 2.20 shows the time delay-dependent N-DFWM signal intensity from a measurement done on 500 μm thick Magnesium Oxide (MgO) bulk crystal. In the experiment, $k_{\text{VUV}} = k'_{\text{VUV}}$, and the pump polarization is set to 45° with respect to the probe polarization. The emitted signal travels along the NIR beam, with polarization orthogonal to the probe. MgO was chosen as the sample because of its large absorption cross-section for 5th-harmonic [113]. In figure 2.20 we see a strong peak at zero time delay, which we attribute to an NIR-NIR interaction. Additional features can be seen near the expected arrival times of the 3rd- and 5th-harmonic. Reliably reproducing these results is still an outstanding challenge, one that will take further improvement in detection capabilities.

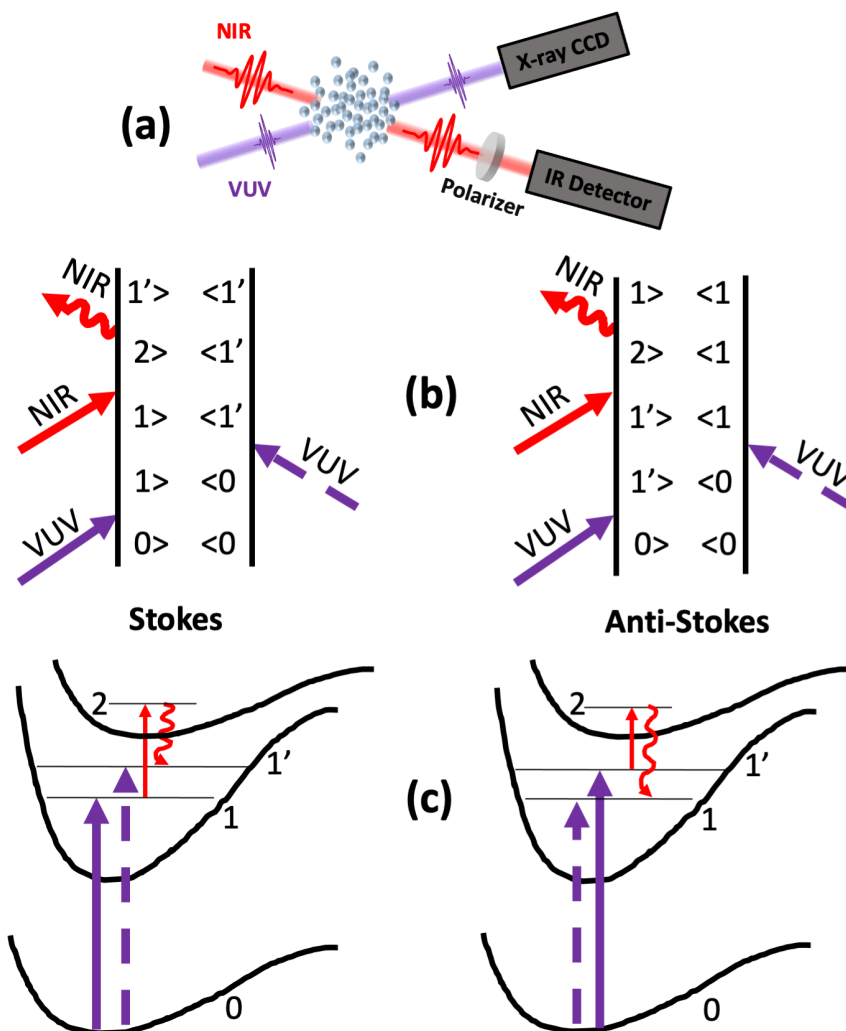


Figure 2.19. (a) Example of a possible VUV-NIR four-wave mixing scheme, where the emitted E-field is NIR. (b) Double-sided Feynman diagrams illustrating a Stokes and an Anti-Stokes pathway for signal emission. The VUV fields create a broadband coherence, which is then probed by the NIR field. (c) Energy level diagrams for the quantum pathways shown in (b). To emit signal in the NIR, the target molecule must be left in an excited state, making such an experiment non-parametric.

To better guide this pursuit, it is important to estimate the expected signal level and compare it to the shot noise limit of detection. First, we calculate the maximum shot noise per pixel. For a CMOS camera, with a typical QE of 25% at 810 nm, the minimum number of detectable photons per pixel is 4. In terms of average power, this equals $\sim 10^{-18}$ J/pulse

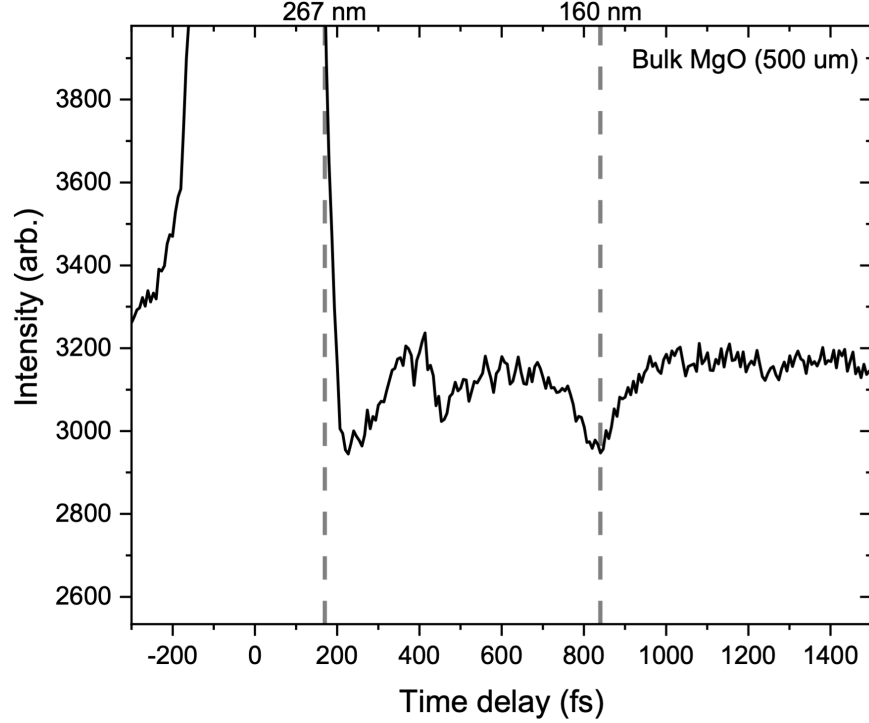


Figure 2.20. Four-wave mixing experiment in bulk MgO crystal (500 μm thick). The harmonic pump beam consists of 810 nm + 270 nm + 162 nm, and the probe is NIR (810 nm). The measured signal intensity shows distinct features near the expected arrival times of the 3rd- and 5th-harmonic. The dominant peak at zero time delay is attributed to an interaction between the probe and the residual NIR leakage of the drive.

$\times 1000$ pulses/s = 1 fW. At this power (\bar{P}), the shot noise power spectral density (/Hz) is given by [114]

$$S(f) = \frac{2h\nu}{\bar{P}} = \frac{2 \times 1.53 \times (1.6 \times 10^{-19})}{10^{-15}} = 4.9 \times 10^{-4} \quad (2.22)$$

The relative intensity (shot) noise can be calculated, for a 1s lock-in acquisition (bandwidth = 1 Hz), using [114]

$$\frac{\delta P}{\bar{P}} = \sqrt{\int S(f) df} = \sqrt{4.9 \times 10^{-4}} \sim 10^{-1.6} \quad (2.23)$$

In these FWM experiments, a high-contrast polarizer is used to suppress the probe light incident on the camera, while allowing the orthogonally-polarized FWM signal to pass

through. The extinction ratio of the polarizer was measured to be $\sim 10^{-4.8}$. Additionally, lock-in detection with a 1 Hz detection bandwidth, and 500 Hz Nyquist frequency further suppresses broadband noise by $1/500 \sim 10^{-2.7}$. Therefore, the (maximum) photon shot noise floor is $\sim 10^{-9}$ of the incident NIR probe power. Detection of signal levels below this threshold will require further improvements in the detection scheme.

2.5 Conclusions

We have discussed the design and construction of a versatile ultrafast VUV/EUV generation beamline. A dual-mode design allows both high-flux VUV generation in the 110 - 270 nm wavelength range, and low-flux EUV generation in the 13 - 110 nm wavelength range. To generate and use EUV harmonics, the leaky gas cell can be replaced with an effusive gas jet, and the z-fold dielectric mirrors can be replaced with a grazing incidence toroidal mirror. The spectrometer chamber has multiple exit ports for mounting the X-ray CCD, such that a grazing incidence EUV grating can be used instead of the present configuration. The beamline can be easily adapted to incorporate electron/ion measurements in the far future.

We have presented benchmark transient absorption spectroscopy (TAS) and transient polarization spectroscopy (TPS) experiments, to demonstrate the versatility of the beamline. In the near future, spectral interferometry can possibly be extended to the VUV range by generating a pair of time-delayed VUV pulses [115]. The time delay between the VUV pulses will result in spectral interference fringes on the CCD. When a strong NIR pulse is temporally overlapped with the first VUV pulse, absorption of the VUV pulse will modulate due to VUV-NIR interaction. Assuming that this type of interaction lasts only for a few tens of femtoseconds, the second VUV pulse will travel through the sample uninteracted. The spectral interference on the CCD will have the form

$$|E_{VUV} + E'_{VUV}|^2 = I_{VUV} + I'_{VUV} + E_{VUV} E'_{VUV} \cos[\Delta\varphi_{VUV} + \omega\tau] \quad (2.24)$$

from which we can possibly measure the temporal phase shift of the first VUV pulse, due to interaction with the overlapped NIR pulse. Experiments are currently underway to

implement all these, and other ideas that are made possible with a coherent light source like this.

3. ATTOSECOND SCIENCE WITH EUV ENTANGLED PHOTONS

3.1 Introduction

He found that he could not secure a derivation for his magic formula for the radiation distribution unless he made an assumption which, from a philosophical standpoint, he found all but unacceptable. - Roy J. Galuber (100 Years of Light Quanta).

In chapter 1 and 2, the discussion of nonlinear spectroscopy assumed light to be a purely classical electromagnetic wave, that interacts with a quantum mechanical system. However, at very low levels, the quantum nature of light can start to affect experiments, and even open new avenues for exploration [116]. Let us first see how to quantize the electromagnetic field. In canonical quantization, the electric field is promoted to an operator

$$\vec{E}(\vec{r}, t) = \sum_{\alpha} \vec{\epsilon}_{\alpha} \int \frac{d\vec{k}}{(2\pi)^{3/2}} E_{\alpha}(\vec{k}, t) e^{i\vec{k} \cdot \vec{r}} \quad (3.1)$$

where the summation is over all the polarizations $\vec{\epsilon}_{\alpha}$, and both $\vec{E}(\vec{r}, t)$ and $E_{\alpha}(\vec{k}, t)$ are operators. Plugging this into Maxwell's wave equation gives

$$\partial_t^2 E_{\alpha}(\vec{k}, t) = -(kc)^2 E_{\alpha}(\vec{k}, t) \quad (3.2)$$

with the general solution

$$\begin{aligned} E_{\alpha}(\vec{k}, t) &= a_{\vec{k}, \alpha} e^{-i\omega_k t} + b_{\vec{k}, \alpha} e^{+i\omega_k t} \\ \omega_k &= |\vec{k}|c \end{aligned} \quad (3.3)$$

Since the electric field is real, $A_{\alpha}(-\vec{k}, t) = A_{\alpha}^{\dagger}(\vec{k}, t)$, and thus $b_{\vec{k}, \alpha} = a_{-\vec{k}, \alpha}^{\dagger}$, giving the final expression

$$\vec{E}(\vec{r}, t) = \sum_{\alpha} \vec{\epsilon}_{\alpha} \int \frac{d\vec{k}}{(2\pi)^{3/2}} \left[a_{\vec{k}, \alpha} e^{-i(\omega_k t - \vec{k} \cdot \vec{r})} + a_{-\vec{k}, \alpha}^{\dagger} e^{i(\omega_k t - \vec{k} \cdot \vec{r})} \right] \quad (3.4)$$

We have now expressed the field in terms of new operators $a_{\vec{k},\alpha}, a_{\vec{k},\alpha}^\dagger$. Let us now introduce the field momentum

$$\vec{E}(\vec{r}, t) = \sum_{\alpha} \vec{\epsilon}_{\alpha} \int \frac{(-i\omega_k) d\vec{k}}{(2\pi)^{3/2}} \left[a_{\vec{k},\alpha} e^{-i(\omega_k t - \vec{k} \cdot \vec{r})} - a_{\vec{k},\alpha}^\dagger e^{i(\omega_k t - \vec{k} \cdot \vec{r})} \right] \quad (3.5)$$

In the absence of charges and currents, the magnetic field is related to the electric field by Maxwell's equation (in CGS units)

$$\vec{\nabla} \times \vec{B}(\vec{r}, t) = \dot{\vec{E}}(\vec{r}, t)/c \quad (3.6)$$

If we expand $\vec{B}(\vec{r}, t)$ in terms of operators $c_{\vec{k},\alpha}, c_{\vec{k},\alpha}^\dagger$ and polarization vectors $\vec{\eta}_{\alpha}$ akin to the expansion of $\vec{E}(\vec{r}, t)$, we find that

$$c_{\vec{k},\alpha} \vec{\eta}_{\alpha} = a_{\vec{k},\alpha} (\hat{k} \times \vec{\epsilon}_{\alpha}) \quad (3.7)$$

We can now calculate the operator analog of energy for the electromagnetic field (in CGS units) as

$$\begin{aligned} H &= \frac{1}{8\pi} \int d\vec{r} (|\vec{E}|^2 + |\vec{B}|^2) \\ &= \frac{1}{4\pi} \sum_{\alpha} \int d\vec{k} \left(a_{\vec{k},\alpha}^\dagger a_{\vec{k},\alpha} + a_{\vec{k},\alpha} a_{\vec{k},\alpha}^\dagger \right) \\ &= \frac{1}{4\pi} \sum_{\alpha} \int d\vec{k} \left(2 a_{\vec{k},\alpha}^\dagger a_{\vec{k},\alpha} + [a_{\vec{k},\alpha}, a_{\vec{k},\alpha}^\dagger] \right) \end{aligned} \quad (3.8)$$

Let us now redefine the operators as $a_{\vec{k},\alpha} \rightarrow a_{\vec{k},\alpha} \sqrt{2\pi\hbar\omega_k}$, and impose canonical commutation relations

$$\begin{aligned} [a_{\vec{k},\alpha}, a_{\vec{k}',\alpha'}^\dagger] &= \delta(\vec{k} - \vec{k}') \delta_{\alpha,\alpha'} \\ [a_{\vec{k},\alpha}, a_{\vec{k}',\alpha'}] &= [a_{\vec{k},\alpha}^\dagger, a_{\vec{k}',\alpha'}^\dagger] = 0 \end{aligned} \quad (3.9)$$

which finally gives

$$H = \sum_{\alpha} \int d\vec{k} \hbar\omega_k \left(a_{\vec{k},\alpha}^\dagger a_{\vec{k},\alpha} + \frac{1}{2} \right) \quad (3.10)$$

The Hamiltonian now looks similar to that of the quantum harmonic oscillator, with each unique \vec{k} corresponding to a unique oscillator mode. The zero-point energy term is divergent, and usually ignored. We can now define a one-photon state of this field as $|\vec{k}, \alpha\rangle = \sqrt{\hbar\omega_k} a_{\vec{k},\alpha}^\dagger |0\rangle$, where the vacuum state $|0\rangle$ is defined via $a_{\vec{k},\alpha}|0\rangle = 0$ and $\langle 0|0\rangle = 1$. The multiplicative factor $\sqrt{\hbar\omega_k}$ ensures that the normalization of these states is Lorentz invariant [117]. These states obey the relations

$$\begin{aligned}\langle \vec{k}, \alpha | \vec{k}', \alpha' \rangle &= \hbar\omega_k \delta(\vec{k} - \vec{k}') \delta_{\alpha,\alpha'} \\ H|\vec{k}, \alpha\rangle &= \hbar\omega_k |\vec{k}, \alpha\rangle\end{aligned}\tag{3.11}$$

A simple calculation now shows that

$$\langle 0 | \vec{E}(\vec{r}, t) | \vec{k}, \alpha \rangle = \left(\frac{\hbar\omega_k}{2\pi} \right) e^{-i(\omega_k t - \vec{k} \cdot \vec{r})} \vec{\epsilon}_\alpha\tag{3.12}$$

and we can draw an analogy between $\vec{E}(\vec{r}, t)|0\rangle$ and $|\vec{r}\rangle$, the eigenstates of the position operator. Equation 3.12 measures the value of the electric field at the position \vec{r} and time t , for the mode $|\vec{k}, \alpha\rangle$.

Quantum entanglement is a general feature of any quantum mechanical system, and carries over to this quantized description of light. A two-photon state may be written as

$$|\Psi_{2ph}\rangle = \int \int d\vec{k} d\vec{k}' F(\vec{k}, \alpha; \vec{k}', \alpha') |\vec{k}, \alpha\rangle |\vec{k}', \alpha'\rangle\tag{3.13}$$

If the coefficient $F(\vec{k}, \alpha; \vec{k}', \alpha')$ cannot be factored as $G(\vec{k}, \alpha) \cdot H(\vec{k}', \alpha')$, then the two photons are said to be entangled. We shall refer to the quantum state with such a non-separable wavefunction as a bi-photon.

3.2 Generating bi-photons using $1s2s\ ^1S_0$ metastable helium

Typical sources of entangled photons use the process of spontaneous parametric down-conversion (SPDC) in nonlinear crystals in the visible and infrared region of the spectrum [118]. These sources generate energy-time entangled photons with correlation times on the

femtosecond time scale which has been only recently directly measured [119]. SPDC has also been demonstrated in the hard X-ray regime where the correlation times are expected to be attoseconds or smaller [120]. Recent experiments using nanophotonic chips for SPDC have demonstrated entangled photon generation with broad bandwidth of 100 THz (0.41 eV) with a high generation efficiency of 13 GHz/mW [121]. Here we propose a method to generate entangled photon pairs in the extreme-ultraviolet (EUV) regime with energy bandwidth large enough to create correlation times on the attosecond scale.

It is well known that the $1s2s\ ^1S_0$ metastable state of helium atom, its isoelectronic ions and the $2s\ ^2S_{1/2}$ metastable state of the helium ion decay predominantly by two-photon emission [122]–[126]. The emitted photons are energy-time entangled with a correlation time related to the energy spacing between the $2s$ and $1s$ levels which is 20.62 eV and 40.81 eV for the helium atom and ion respectively. This large energy bandwidth of the emitted entangled photons corresponds to correlation times in the attosecond domain, thus opening up the possibility of attosecond time scale pump-probe experiments using these photons.

We can better understand this correlation time by studying the decay of an excited atom via two-photon emission. Assume that the excited state has energy ω_0 and a narrow linewidth, which we will model using a Dirac delta function. Without loss of generality, we will consider only one spatial dimension and assume that both the photons are emitted in one direction (say along $+\hat{z}$). Additionally, we will consider only one polarization (say $\vec{\epsilon}$).

With these assumptions, the two-photon state has the simpler form

$$|\Psi_{2ph}\rangle = \int_0^\infty \int_0^\infty dk_1 dk_2 F(k_1; k_2) |\vec{k}_1\rangle |\vec{k}_2\rangle \quad (3.14)$$

where \vec{k}_1 and \vec{k}_2 both are along $+\hat{z}$. To achieve an analytic expression, we will make the additional assumption that the emitted photons have a total bandwidth $\omega_1 - \omega_2 = \pm\Omega$. This can be easily understood as an experimental constraint, for instance, when the maximum detectable energy of the detector is $(\omega_0 + \Omega)/2$, or when the transmission window of some optic in the experiment is $(\omega_0 \pm \Omega)/2$. Then, the momentum-space wavefunction is given by

$$F(k_1; k_2) = \frac{\delta(k_1 + k_2 - \omega_0/c)}{2\Omega/c} \Pi\left(\frac{k_1 - k_2}{2\Omega/c}\right) \quad (3.15)$$

and Π is the rectangular function defined as

$$\Pi\left(\frac{x}{a}\right) = \begin{cases} 1, & |x| \leq a/2 \\ 0, & |x| > a/2 \end{cases} \quad (3.16)$$

A two-point field correlation can be defined analogous to equation 3.12 as $\langle \Omega | \vec{E}_1(\vec{r}_1, t_1) \otimes \vec{E}_2(\vec{r}_2, t_2) | \Psi_{2ph} \rangle$. Here, $|\Omega\rangle = |0\rangle_p \otimes |0\rangle_q \otimes \dots$ is the tensor product of the vacuum states corresponding to each single-particle operator a_p, a_q, \dots , and thus represents the many-particle vacuum state of the electromagnetic field. Operators $E_1(\vec{r}_1, t_1)$ and $E_2(\vec{r}_2, t_2)$ act on particles 1 and 2, respectively. For $\vec{r}_1 = \vec{r}_2 = 0$, this two-point correlation can be calculated as

$$\begin{aligned} \langle \Omega | \vec{E}_1(0, t_1) \otimes \vec{E}_2(0, t_2) | \Psi_{2ph} \rangle &= \int_0^\infty \int_0^\infty dk_1 dk_2 F(k_1; k_2) \langle 0 | \vec{E}_1(0, t_1) | \vec{k}_1 \rangle \langle 0 | \vec{E}_2(0, t_2) | \vec{k}_2 \rangle \\ &= \frac{\hbar^2}{c^2} \int_0^\infty \int_0^\infty d\omega_1 d\omega_2 F(\omega_1/c; \omega_2/c) \omega_1 \omega_2 e^{-i(\omega_1 t_1 + \omega_2 t_2)} (\vec{\epsilon} \otimes \vec{\epsilon}) \\ &= \frac{\hbar^2}{2\Omega c} \int_0^\infty \int_0^\infty d\omega_1 d\omega_2 \delta(\omega_1 + \omega_2 - \omega_0) \Pi\left(\frac{\omega_1 - \omega_2}{2\Omega}\right) \omega_1 \omega_2 e^{-i(\omega_1 t_1 + \omega_2 t_2)} (\vec{\epsilon} \otimes \vec{\epsilon}) \\ &= \frac{\hbar^2}{2\Omega c} \int_0^\infty \int_{-\infty}^\infty d\omega_+ d\omega_- \delta(\omega_+ - \omega_0) \Pi\left(\frac{\omega_-}{2\Omega}\right) (\omega_+^2 - \omega_-^2) e^{-i\omega_+ \frac{(t_1+t_2)}{2}} e^{-i\omega_- \frac{(t_1-t_2)}{2}} (\vec{\epsilon} \otimes \vec{\epsilon}) \\ &= e^{-i\omega_0 T} \frac{\hbar^2}{2\Omega c} \int_{-\Omega}^\Omega d\omega_- (\omega_0^2 - \omega_-^2) e^{-i\frac{\Delta T}{2}\omega_-} (\vec{\epsilon} \otimes \vec{\epsilon}) \end{aligned} \quad (3.17)$$

where $T = (t_1 + t_2)/2$ and $\Delta T = t_1 - t_2$, and we introduced $w_\pm = (\omega_1 \pm \omega_2)$ to solve the integral. Finally, if we consider $\Omega \ll \omega_0$, the above expression simplifies to

$$\frac{(\hbar\omega_0)^2}{c} e^{-i\omega_0 T} \text{sinc}\left(\frac{\Omega\Delta T}{2}\right) (\vec{\epsilon} \otimes \vec{\epsilon}) \quad (3.18)$$

Thus, the temporal correlation of the emitted photon pair is controlled by the two-photon bandwidth Ω , and not by the linewidth of the excited to ground transition. The linewidth of the excited state can be extremely narrow, and still lead to the emission of bi-photons that have strongly correlated arrival times.

For this experiment, we chose helium for the robustness of its metastable state, and the simplicity of its electronic structure. Another candidate for generating entangled photon pairs could be the hydrogen atom. Two-photon emission in hydrogen would give entangled photons of wavelength 243 nm, which can propagate in free space, and would not require high vacuum for propagation. However, calculations of the Stark shift in the $n = 2$ level of hydrogen (see figure 3.1) show that even in the presence of very weak electric fields, the state with predominantly 2s character has enough 2p character to decay to the ground state through single photon emission. Such a quenching, for helium, will require much higher electric fields because of the larger energy gap between the 2s and 2p states in helium.

Femtosecond laser pulses with a central wavelength of 240 nm (5.16 eV) can be used to excite helium atoms to the $1s2s$ excited state (20.61 eV) via a four-photon transition (see figure 3.2 (a)). However, the $1s2s$ metastable state has a narrow linewidth of ~ 50 Hz, and multiphoton excitation to this state requires intense lasers with a linewidth smaller than 50 Hz. For comparison, typical femtosecond pulses have a bandwidth of ~ 20 THz. While excitations of multiphoton metastable states with narrow linewidth lasers have been previously demonstrated [127], achieving a significant fraction of metastable atoms with a 240 nm laser is currently challenging. With a 240 nm femtosecond laser, with a typical bandwidth of ~ 5 THz, a bi-photon generation rate of $\sim 10^{11} \text{ s}^{-1}$ can be expected (see section 3.3).

An alternative scheme using a lambda-type transition between the $1s^2$, $1s2p$, and $1s2s$ states could be used to achieve significant excitation. The energy levels of the latter two are 21.22 eV and 20.62 eV above the ground state, respectively. A two-step sequential excitation to first excite the $1s^2 \rightarrow 1s2p$ transition and then the $1s2p \rightarrow 1s2s$ transition could be used. To achieve this two-step sequential excitation, a high photon flux helium lamp source can be used in the first step to excite $1s2p$ and a 2059 nm laser can transfer population to the $1s2s$ state (see figure 3.2 (b)). The ~ 1 GHz linewidth of the $1s2p$ state makes transitions to the $1s2s$ state using a broadband laser more feasible in comparison to direct multiphoton excitation. Currently available helium lamp sources are capable of generating $\sim 10^{15}$ photons s^{-1} . Using a high pressure helium target, nearly all of these photons could be absorbed to generate helium atoms in the $1s2p$ state. A high repetition-rate pulsed laser source at 2059

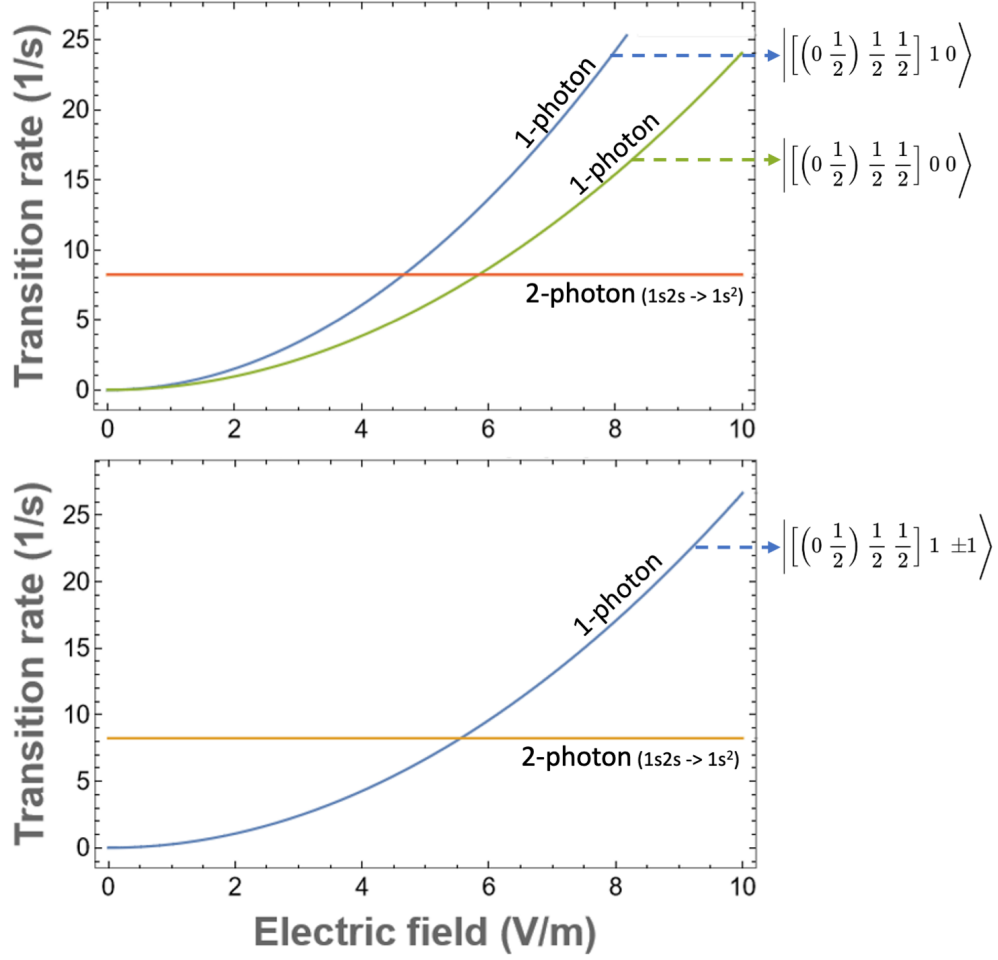


Figure 3.1. One-photon decay rates for the DC Stark-shifted $2S_{1/2}$ state with $m_F = 0, \pm 1$, as a function of the applied electric field. The Stark-shifted states are labelled using the $\left| \left[(L S) J I \right] F m_F \right\rangle$ convention. The two-photon decay rate of the unperturbed $2S_{1/2}$ state is also shown for comparison. Since the one-photon decay rate of the $2P_{1/2}$ and $2P_{3/2}$ states is $6 \times 10^8 s^{-1}$, even a small amount of mixing quenches the metastable $2S_{1/2}$ state.

nm, could transfer nearly all these excited helium atoms to the $1s2s$ state. Using this method, a bi-photon generation rate of $\sim 10^{13} s^{-1}$ can be expected (see section 3.3).

Another alternative approach to achieve significant population of the $1s2s$ singlet metastable state is to use Stark-chirped rapid adiabatic passage (SCRAP), previously proposed to excite the $2s$ metastable state in a hydrogen atom [128], [129]. In this technique, a pump pulse

excites the metastable state via a multiphoton transition in the presence of a Stark pulse that Stark shifts the $1s2s$ state across the bandwidth of the pump pulse (see figure 3.2 (c)). The combined effect of the two pulses results in a Landau-Zener-type adiabatic passage that can significantly populate the $1s2s$ state.

A simple to follow description of rapid adiabatic passage for a two-level system is as follows. Let us assume a two-level system with states $|0\rangle$, $|1\rangle$. The presence of an electric field mixes the two states, giving the new eigenbasis

$$\begin{aligned}\Psi_- &= \cos \Theta(t)|0\rangle - \sin \Theta(t)|1\rangle \\ \Psi_+ &= \sin \Theta(t)|0\rangle + \cos \Theta(t)|1\rangle \\ \tan 2\Theta(t) &= \Omega(t)/2\Delta(t)\end{aligned}\tag{3.19}$$

where $\Omega(t)$ is the Rabi coupling between the two states, and $\Delta(t)$ is the detuning (including Stark shifts) of the excitation laser with the frequency of the transition. On adiabatically sweeping $\Delta(t)$, from a large negative value to a large positive value through the resonance, the eigenstate Ψ_- adiabatically evolves into the state Ψ_+ , leading to complete population transfer from the $|0\rangle$ to the $|1\rangle$ state. At the intensities required for a four-photon transition, multiphoton ionization will reduce the amount of $1s2s$ excited helium atoms created. The SCRAP technique [129] can also suppress ionization loss by laser-induced continuum structure (LICS) [128], [130], [131]. If we ignore ionization loss, for a typical femtosecond laser pulse-width of 50 fs with a bandwidth of 8.8 THz, rapid-adiabatic passage can excite nearly all atoms in the focal volume. At a femtosecond pulse repetition rate of 100 kHz currently available, this results in a bi-photon generation rate of 10^{16} s^{-1} (see section 3.3). Among the three methods discussed here to excite helium to the singlet $1s2s$ state, the SCRAP method is expected to provide the highest excitation rate and hence the highest bi-photon generation rate.

3.3 Excitation rates for the helium $1s2s \ ^1S_0$ state

In this section, we give estimates for the rate of bi-photon generation from the helium $1s2s$ state under realistic experimental conditions, for the aforementioned schemes. For a

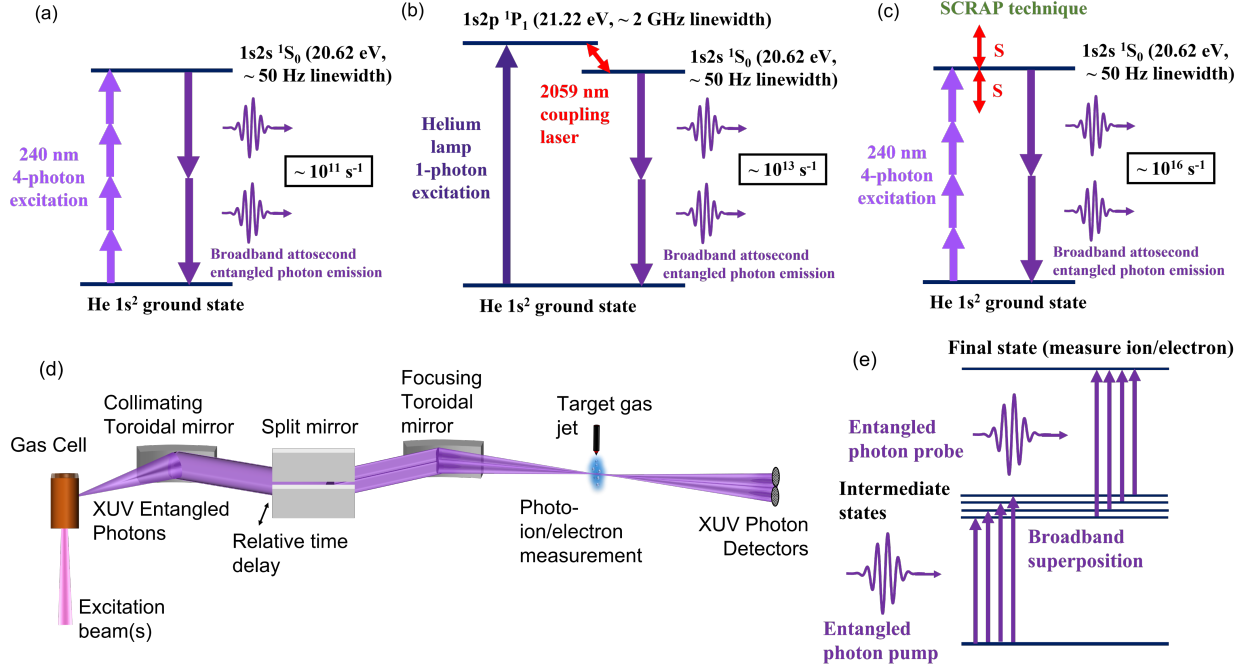


Figure 3.2. (a) Generation of bi-photons in the EUV via two-photon decay of the $1s2s\ ^1S_0$ state excited by four-photon excitation using a broad band 240 nm laser. (b) Two-step sequential excitation of the $1s2s$ state via the $1s2p$ state using a high photon flux helium lamp and a 2059 nm coupling laser. (c) The SCRAP technique to populate the $1s2s$ state using a multiphoton pump pulse and a Stark shifting pulse which enable rapid adiabatic passage and ionization suppression by LICS (LICS not shown). The estimated bi-photon generation rate is also shown for each scheme in (a) - (c). (d) Proposed experimental scheme to generate EUV entangled photons and utilize them in an attosecond pump-probe photoionization experiment. (e) An attosecond pump-probe photoionization scheme in molecules using bi-photons.

helium gas pressure of 1 bar, the number density $N \sim 10^{19}$ atoms/cm³. Such gas densities are easily achievable in static gas cells. In the following calculations, we will assume a pump focal spot diameter $d \sim 10$ μ m (unless specified otherwise), and interaction length $L \sim 1$ mm.

3.3.1 Four-photon excitation using a 240 nm broad-band laser

The multiphoton absorption coefficient is related to the transition rate by the relation

$$\alpha^{(n)} = \frac{n\hbar\omega R^{(n)}N}{I^n} \quad (3.20)$$

where I is the intensity of the incident radiation, $R^{(n)}$ the n -photon transition rate, and N is the number density in atoms/cm³. The variation in the intensity of radiation with distance is then given by

$$I(z) = I_0 e^{-\alpha^{(1)}z} \quad (3.21)$$

for single-photon absorption, and

$$I(z) = \frac{I_0}{\left(1 + (n-1)\alpha^{(n)}zI^{n-1}(0)\right)^{\frac{1}{n-1}}} \quad (3.22)$$

for multiphoton absorption. The per atom four-photon transition rate for the 1s2s state in helium at 240 nm can be calculated as

$$R^{(4)} = 2\pi \delta(\Delta_{eg} - 4\omega_0) \left| \left(\frac{e\mathcal{E}_0}{2\hbar} \right)^4 D_{eg}^{(4)} \right|^2 \quad (3.23)$$

where $D_{eg}^{(4)} = 149$ a.u. [132]. For a pump intensity $I_0 = 10^{14}$ W cm⁻² (electric field strength of 0.053 a.u.) in the focus and a narrow laser bandwidth of < 50 Hz (width of the helium 1s2s ¹ S_0 state), the excitation rate is $\sim 4 \times 10^6$ a.u., or $\sim 10^{23}$ s⁻¹ per atom. For the case of a broadband laser, equation 3.23 needs to be integrated over the spectrum of the laser and can be written as

$$R_{br}^{(4)} = \int d\omega_0 \rho(\omega_0) 2\pi \delta(\Delta_{eg} - 4\omega_0) \left| \left(\frac{e\mathcal{E}_0}{2\hbar} \right)^4 D_{eg}^{(4)} \right|^2 \quad (3.24)$$

where $R_{br}^{(4)}$ is the four-photon excitation rate with a broadband laser and $\rho(\omega_0)$ is the normalized spectrum. For a broadband 240 nm laser with a bandwidth of 5 THz, an excita-

tion rate $R_{br}^{(4)} \sim 10^{12} s^{-1}$ per atom is obtained. The absorption coefficient (in S.I. units) is given by

$$\alpha_{br}^{(4)} = \frac{4\hbar\omega_0 R_{br}^{(4)} N}{I^4} = 3.3 \times 10^{-43} W^{-3} cm^5 \quad (3.25)$$

and the absorption fraction is given by

$$\frac{I_0 - I(L)}{I_0} = 1 - \frac{1}{(1 + 3\alpha_{br}^{(4)} L I_0^3)^{1/3}} \sim 0.031 \quad (3.26)$$

Typical femtosecond lasers at 240 nm are composed of $\sim 10^{12}$ photons per pulse. Using the above absorption fraction, $\sim 10^{10}$ excited helium atoms per pulse are expected. At a laser repetition rate of 100 kHz currently available, ignoring ionization loss, an excitation rate and hence a bi-photon rate of $\sim 10^{15} s^{-1}$ is obtained. Under realistic conditions of multiphoton ionization loss, it is reasonable to expect a bi-photon generation rate of $\sim 10^{11} s^{-1}$.

3.3.2 Sequential excitation using helium lamp and 2059 nm laser

We consider a two-step sequential excitation to first excite $1s^2 \rightarrow 1s2p$ and then $1s2p \rightarrow 1s2s$. The oscillator strengths for one-photon excitation processes are $f_{1s^2 \rightarrow 1s2p} = 0.28$ and $f_{1s2p \rightarrow 1s2s} = -0.36$ for the two steps [132]. The corresponding transition rates can be calculated using

$$R^{(1)} = \frac{\pi f}{\hbar\omega_0\mu} e^2 \mathcal{E}_0^2 \delta(\Delta_{eg} - \omega_0) \quad (3.27)$$

where f is the oscillator strength, μ is the reduced mass, ω_0 is the photon angular frequency, \mathcal{E}_0 is the electric field, and the delta function is to be replaced by the lifetime of the excited state. Incoherent lamp sources that can generate $\sim 10^{15}$ photons/s, resonant with the $1s^2 \rightarrow 1s2p$ transition, and with a spot size of 100 μm are commercially available (SPECS GmbH, $\mu S I R I U S$). For the 2059 nm excitation laser, we assume a realistic photon flux of 10^{20} photons/s. Assuming a 100 μm spot size for both the beams, the intensities are $\sim 40 W cm^{-2}$ and $10^5 W cm^{-2}$ for the lamp and the laser, respectively. The transition rates are $R_{1s^2 \rightarrow 1s2p} \sim 10^9$ and $R_{1s2p \rightarrow 1s2s} \sim 10^{21}$ per second per atom.

If we denote the lifetime of the $1s2p$ state by τ , we can calculate the steady-state number density of excited atoms after the first excitation step using [133]:

$$\frac{N_{exc}}{N} = \frac{1}{2} \left(1 - \frac{1}{1 + (2\sigma^{(1)}\tau/\hbar\omega_0)I} \right) = \frac{1}{2} \left(1 - \frac{1}{1 + 2R_{lamp}^{(1)}\tau} \right) \sim 0.4 \quad (3.28)$$

where N_{exc} and N are the number of excited atoms and total number of atoms in the focal volume, $\sigma^{(1)}$ is the one-photon absorption cross section, I is the photon flux density and $R_{lamp}^{(1)}$ is the excitation rate for a lamp source. At a pressure of 1 bar, the focal volume contains $\sim 10^{14}$ neutral atoms, 40% of which are excited to the $1s2p$ state. Note that the number of 2059 nm photons is much larger than the number of excited atoms in the focal volume. It is possible to saturate the $1s2p \rightarrow 1s2s$ transition and all the atoms in the $1s2p$ state could be promoted by the 2059 nm laser to the $1s2s$ state. This gives a bi-photon generation rate of $\sim 10^{13}$ per second. Note that for a sufficiently strong pulsed 2059 nm laser at high repetition rates, both the number of photons per second in the focal volume and the excitation rate per atom will satisfy the above mentioned criteria, and thus, give a similar rate of bi-photon generation.

3.3.3 Four-photon excitation using SCRAP

We consider a scenario where rapid adiabatic passage is used to transfer population from the $1s^2$ to the $1s2s$ state via a four-photon coupling. Neglecting ionization leakage from the $1s2s$ state, the transfer efficiency is limited only by non-adiabatic transitions between the adiabatic states, which will be estimated in this section. The single-photon Rabi frequency $\Omega_{eg} = \langle \vec{\mu}_{eg} \cdot \vec{E} \rangle / \hbar$ can be generalized for a four-photon transition as

$$\Omega_{eg} = \left(\frac{e\mathcal{E}_0}{2\hbar} \right)^4 D_{eg}^{(4)} \quad (3.29)$$

for linearly polarized light. If we consider the $1s^2, 1s2s$ (1S_0) subspace as a two-level system, the four-photon Rabi frequency at a 240 nm laser intensity of 10^{14} W cm⁻² becomes

$$\Omega_{eg} = 7.35 \times 10^{-5} a.u. = 1.9 \times 10^{13} s^{-1} \quad (3.30)$$

Let us assume that a Stark pulse sweeps the transition energy across the entire bandwidth of a pump pulse of duration τ seconds and bandwidth δ Hz. We will further assume a static detuning $\delta/2$ for the four-photon pump pulse, such that the Rabi frequency $\Omega = \sqrt{\Omega_{eg}^2 + \delta^2/4}$. The rate of leakage due to non-adiabatic transitions can be calculated using the Landau-Zener formula [134]:

$$\Gamma(t) = \Omega^2 \frac{\gamma}{\Delta^2 + \gamma^2/4} \quad (3.31)$$

where $\gamma \sim \sqrt{\dot{\Delta}/4\pi}$. Assuming a linear Stark sweep, $\Delta(t) = t(\delta/\tau)$ Hz ($-\tau/2 \leq t \leq \tau/2$), and $\gamma = \sqrt{\delta/4\pi\tau}$. The corresponding transition rate is

$$\Gamma(t) = \frac{\Omega^2 \sqrt{\delta/4\pi\tau}}{t^2 (\delta/\tau)^2 + \delta/16\pi\tau} \quad (3.32)$$

For a pulse of duration $\tau = 50$ fs and bandwidth $\delta = 8.8$ THz, the probability of population transfer to the excited state, neglecting ionization leakage, is

$$1 - \exp \left[- \int_{-\tau/2}^{\tau/2} \Gamma(t) dt \right] = 1 - \exp(-10.1) = 0.99996 \quad (3.33)$$

This shows that nearly all atoms in the focal volume can be excited. The SCRAP technique also involves ionization suppression by laser-induced continuum structure (LICS). Thus it is reasonable to assume that when ionization loss and LICS are considered, at least 0.1% of the atoms in the focal volume are excited to the singlet $1s2s$ state for every pair of pump and Stark pulses. With $\sim 10^{14}$ atoms in the focal volume corresponding to a $100 \mu\text{m}$ spot size and 1 mm path length at 1 bar target pressure, this results in $\sim 10^{11}$ atoms excited per pulse. At a femtosecond pulse repetition rate of 100 kHz currently available, this results in a bi-photon generation rate of 10^{16} s^{-1} .

3.4 Detecting attosecond entangled bi-photons

The excited helium atoms relax by emitting correlated photons with a lifetime of ~ 19.7 ms [135]. The correlation time of the emitted entangled photons is ~ 200 attoseconds, corresponding to a bandwidth of 20.61 eV [132]. This correlation can be experimentally

measured using a Hanbury Brown-Twiss setup, where the two entangled photons are sent to two separate detectors with a controllable mutual delay τ . The width of their intensity correlation, $g^{(2)}(\tau)$, should then give access to their correlation time, provided that the experimental accuracy is sufficient [136].

Let the rate of bi-photon generation be λ . And let the probability that a pair of arbitrarily chosen photons reach separate detectors be p . Assuming a detection window of duration τ , the number of entangled photon pairs that reach separate detectors in coincidence will be

$$p \cdot \lambda \tau \quad (3.34)$$

On the other hand, the number of random (not entangled) photon pairs, emitted from two different atoms, that reach separate detectors in coincidence will be

$$p \cdot \lambda^2 C_2 = p \cdot (\lambda \tau)(\lambda \tau - 1) \quad (3.35)$$

for $\lambda \tau \geq 2$. Thus, the ratio of coincidence counts from entangled photons to background coincidence counts will be

$$\frac{1}{\lambda \tau - 1} \quad (3.36)$$

This coincidence-to-accidental ratio (CAR), as a function of detection window τ , is plotted in figure 3.3 for different excitation rates λ . By lowering the number of helium atoms excited per pulse, the CAR can be increased for detection of the bi-photons.

The bi-photons from the decay of the $1s2s$ state are emitted in all directions with an approximate distribution given by $1 + \cos^2(\theta)$ [126], where θ is the relative angle between the entangled photons. The photons that are emitted in a direction orthogonal to the excitation laser propagation direction can be collected within a large solid angle and sent along independent time-delayed paths towards a pump-probe target. Figure 3.2 (d) shows a schematic of a proposed experimental setup for generation of these entangled photons and their utilization in an attosecond pump-probe experiment. In this scheme, a grazing incidence toroidal mirror collimates the emitted photons which are then split into two halves using a grazing incidence split mirror that introduces a controllable time-delay between the

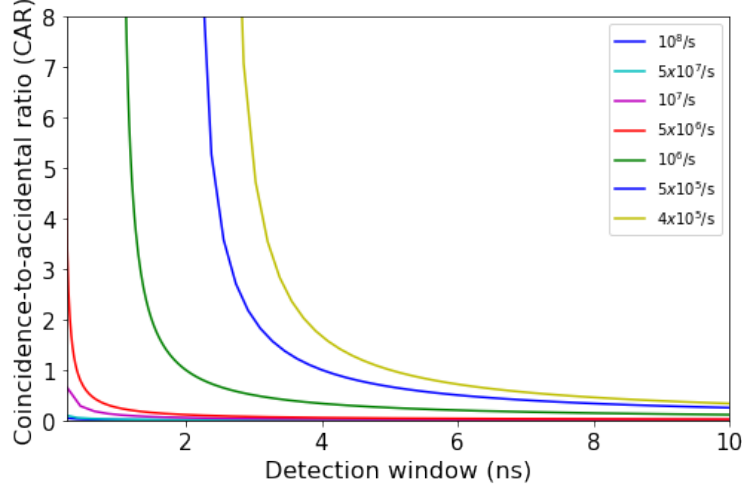


Figure 3.3. Coincidence-to-accidental ratio (CAR), as a function of detection window τ , for various bi-photon excitation rates. CAR measures the number of true coincidence counts, compared to the number of background coincidence counts, and is a form of SNR.

two halves of the beam. Collecting bi-photons emitted along the same direction within a large solid angle (as opposed to those emitted in opposite directions), ensures that no time-smearing is introduced in the arrival times of the bi-photons. The split beams are then focused using a second toroidal mirror onto the target gas jet. A pump-probe experiment with attosecond time resolution can be performed by measuring a photo-ion or photo-electron signal arising from the absorption of bi-photons by an atom or molecule (see figure 3.2 (e)). Such entangled photon pump-probe experiments will extend the capabilities of attosecond science, where currently attosecond pulses from high-order harmonic generation [137] or free electron laser [138] sources are used.

3.5 Conclusions

In conclusion, an unconventional approach is presented here for generating attosecond entangled bi-photons in the EUV using two-photon decay in helium atoms. Multiple alternative schemes can be used to excite the $1s2s\ ^1S_0$ metastable state in helium for which excitation rates have been estimated and an experimental scheme is suggested to collect and

use the emitted EUV bi-photons in attosecond pump-probe experiments. The entangled photon generation scheme discussed here can be extended to the soft X-ray (SXR) regime using helium-like ions. In one possible scheme, strong laser field ionization could generate Ne^{8+} ions in the ground state and an FEL could excite them to the $1s2s\ ^1S_0$ state by two-photon excitation which then generate highly broadband bi-photons at SXR energies. This approach can open doors to using EUV/SXR entangled photons in quantum imaging and attosecond quantum spectroscopy of atomic, molecular and solid-state systems.

REFERENCES

- [1] J. Jankunas, M. Sneha, R. N. Zare, *et al.*, “Is the simplest chemical reaction really so simple?” *Proceedings of the National Academy of Sciences*, vol. 111, no. 1, pp. 15–20, 2014.
- [2] F. Krausz and M. Ivanov, “Attosecond physics,” *Reviews of Modern Physics*, vol. 81, no. 1, p. 163, 2009.
- [3] R. Geneaux, H. J. Marroux, A. Guggenmos, D. M. Neumark, and S. R. Leone, “Transient absorption spectroscopy using high harmonic generation: A review of ultrafast x-ray dynamics in molecules and solids,” *Philosophical Transactions of the Royal Society A*, vol. 377, no. 2145, p. 20170463, 2019.
- [4] J. Li, J. Lu, A. Chew, *et al.*, “Attosecond science based on high harmonic generation from gases and solids,” *Nature Communications*, vol. 11, no. 1, p. 2748, 2020.
- [5] M. Nisoli, P. Decleva, F. Calegari, A. Palacios, and F. Martín, “Attosecond electron dynamics in molecules,” *Chemical reviews*, vol. 117, no. 16, pp. 10760–10825, 2017.
- [6] J. Itatani, F. Quéré, G. L. Yudin, M. Y. Ivanov, F. Krausz, and P. B. Corkum, “Attosecond streak camera,” *Phys. Rev. Lett.*, vol. 88, no. 17, p. 173903, 2002.
- [7] E. Goulielmakis, M. Uiberacker, R. Kienberger, *et al.*, “Direct measurement of light waves,” *Science*, vol. 305, no. 5688, pp. 1267–1269, 2004.
- [8] P. Eckle, M. Smolarski, P. Schlup, *et al.*, “Attosecond angular streaking,” *Nature Physics*, vol. 4, no. 7, pp. 565–570, 2008.
- [9] Y. Liu, S. Gholam-Mirzaei, J. E. Beetar, *et al.*, “All-optical sampling of few-cycle infrared pulses using tunneling in a solid,” *Photonics Research*, vol. 9, no. 6, pp. 929–936, 2021.
- [10] Y. Liu, J. E. Beetar, J. Nesper, S. Gholam-Mirzaei, and M. Chini, “Single-shot measurement of few-cycle optical waveforms on a chip,” *Nature Photonics*, vol. 16, no. 2, pp. 109–112, 2022.
- [11] M. R. Bionta, F. Ritzkowski, M. Turchetti, *et al.*, “On-chip sampling of optical fields with attosecond resolution,” *Nature Photonics*, vol. 15, no. 6, pp. 456–460, 2021.

- [12] S. B. Park, K. Kim, W. Cho, *et al.*, “Direct sampling of a light wave in air,” *Optica*, vol. 5, no. 4, pp. 402–408, 2018.
- [13] D. Hui, H. Alqattan, S. Yamada, V. Pervak, K. Yabana, and M. T. Hassan, “Attosecond electron motion control in dielectric,” *Nature Photonics*, vol. 16, no. 1, pp. 33–37, 2022.
- [14] A. Schiffrin, T. Paasch-Colberg, N. Karpowicz, *et al.*, “Optical-field-induced current in dielectrics,” *Nature*, vol. 493, no. 7430, pp. 70–74, 2013.
- [15] T. Paasch-Colberg, A. Schiffrin, N. Karpowicz, *et al.*, “Solid-state light-phase detector,” *Nature Photonics*, vol. 8, no. 3, pp. 214–218, 2014.
- [16] A. Sommer, E. Bothschafter, S. Sato, *et al.*, “Attosecond nonlinear polarization and light–matter energy transfer in solids,” *Nature*, vol. 534, no. 7605, pp. 86–90, 2016.
- [17] S. Sederberg, D. Zimin, S. Keiber, *et al.*, “Attosecond optoelectronic field measurement in solids,” *Nature communications*, vol. 11, no. 1, pp. 1–8, 2020.
- [18] F. Walz, S. Pandey, L. Z. Tan, and N. Shivaram, “Electric field measurement of femtosecond time-resolved four-wave mixing signals in molecules,” *Optics Express*, vol. 30, no. 20, pp. 36 065–36 072, 2022.
- [19] X. Ren, V. Makhija, and V. Kumarappan, “Measurement of field-free alignment of jet-cooled molecules by nonresonant femtosecond degenerate four-wave mixing,” *Physical Review A*, vol. 85, no. 3, p. 033 405, 2012.
- [20] T. R. Dickson, “Time-resolved optical kerr effect spectroscopy by four-wave mixing,” Ph.D. dissertation, University of Toronto, 1992.
- [21] S. Palese, L. Schilling, R. D. Miller, P. R. Staver, and W. T. Lotshaw, “Femtosecond optical kerr effect studies of water,” *The Journal of Physical Chemistry*, vol. 98, no. 25, pp. 6308–6316, 1994.
- [22] D. McMorrow, W. T. Lotshaw, and G. A. Kenney-Wallace, “Femtosecond optical kerr studies on the origin of the nonlinear responses in simple liquids,” *IEEE Journal of Quantum Electronics*, vol. 24, no. 2, pp. 443–454, 1988.

- [23] J. Wahlstrand, J. Odhner, E. McCole, *et al.*, “Effect of two-beam coupling in strong-field optical pump-probe experiments,” *Physical Review A*, vol. 87, no. 5, p. 053 801, 2013.
- [24] Y.-H. Chen, S. Varma, A. York, and H. Milchberg, “Single-shot, space-and time-resolved measurement of rotational wavepacket revivals in h 2, d 2, n 2, o 2, and n 2 o,” *Optics Express*, vol. 15, no. 18, pp. 11 341–11 357, 2007.
- [25] H. Stapelfeldt and T. Seideman, “Colloquium: Aligning molecules with strong laser pulses,” *Reviews of Modern Physics*, vol. 75, no. 2, p. 543, 2003.
- [26] F. Rosca-Pruna and M. Vrakking, “Experimental observation of revival structures in picosecond laser-induced alignment of i 2,” *Physical Review Letters*, vol. 87, no. 15, p. 153 902, 2001.
- [27] V. Renard, M. Renard, A. Rouzée, *et al.*, “Nonintrusive monitoring and quantitative analysis of strong laser-field-induced impulsive alignment,” *Physical Review A*, vol. 70, no. 3, p. 033 420, 2004.
- [28] V. Renard, M. Renard, S. Guérin, *et al.*, “Postpulse molecular alignment measured by a weak field polarization technique,” *Physical review letters*, vol. 90, no. 15, p. 153 601, 2003.
- [29] T. Seideman, “Revival structure of aligned rotational wave packets,” *Physical Review Letters*, vol. 83, no. 24, p. 4971, 1999.
- [30] M. Comstock, V. Lozovoy, and M. Dantus, “Rotational wavepacket revivals for phase modulation of ultrafast pulses,” *Chemical physics letters*, vol. 372, no. 5-6, pp. 739–744, 2003.
- [31] R. N. Zare, *Angular momentum: understanding spatial aspects in chemistry and physics*. J. Wiley & Sons, 1988.
- [32] J. Heritage, T. Gustafson, and C. Lin, “Observation of coherent transient birefringence in c s 2 vapor,” *Physical Review Letters*, vol. 34, no. 21, p. 1299, 1975.
- [33] V. Makhija, X. Ren, D. Gockel, A.-T. Le, and V. Kumarappan, “Orientation resolution through rotational coherence spectroscopy,” *arXiv preprint arXiv:1611.06476*, 2016.

- [34] H. V. S. Lam, S. Yarlagadda, A. Venkatachalam, *et al.*, “Angle-dependent strong-field ionization and fragmentation of carbon dioxide measured using rotational wave packets,” *Physical Review A*, vol. 102, no. 4, p. 043 119, 2020.
- [35] C. Marceau, V. Makhija, D. Platzter, *et al.*, “Molecular frame reconstruction using time-domain photoionization interferometry,” *Physical Review Letters*, vol. 119, no. 8, p. 083 401, 2017.
- [36] M. Gregory, P. Hockett, A. Stolow, and V. Makhija, “Towards molecular frame photoelectron angular distributions in polyatomic molecules from lab frame coherent rotational wavepacket evolution,” *Journal of Physics B: Atomic, Molecular and Optical Physics*, vol. 54, no. 14, p. 145 601, 2021.
- [37] R. W. Boyd, *Nonlinear optics*. Academic Press, 2008.
- [38] T. A. Oliver, “Recent advances in multidimensional ultrafast spectroscopy,” *Royal Society open science*, vol. 5, no. 1, p. 171 425, 2018.
- [39] G. I. Stegeman and R. A. Stegeman, *Nonlinear optics: phenomena, materials and devices*. John Wiley & Sons, 2012.
- [40] H. Lessing and A. Von Jena, “Separation of rotational diffusion and level kinetics in transient absorption spectroscopy,” *Chemical Physics Letters*, vol. 42, no. 2, pp. 213–217, 1976.
- [41] T. Siebert, M. Schmitt, A. Vierheilig, *et al.*, “Separation of vibrational and rotational coherences with polarized femtosecond time-resolved four-wave mixing spectroscopy,” *Journal of Raman Spectroscopy*, vol. 31, no. 1-2, pp. 25–31, 2000.
- [42] M. Reichert, P. Zhao, J. M. Reed, T. R. Ensley, D. J. Hagan, and E. W. Van Stryland, “Beam deflection measurement of bound-electronic and rotational nonlinear refraction in molecular gases,” *Optics Express*, vol. 23, no. 17, pp. 22 224–22 237, 2015.
- [43] M. R. Ferdinandus, H. Hu, M. Reichert, D. J. Hagan, and E. W. Van Stryland, “Beam deflection measurement of time and polarization resolved ultrafast nonlinear refraction,” *Optics Letters*, vol. 38, no. 18, pp. 3518–3521, 2013.
- [44] J. S. Baskin, P. M. Felker, and A. H. Zewail, “Purely rotational coherence effect and time-resolved sub-doppler spectroscopy of large molecules. ii. experimental,” *The Journal of chemical physics*, vol. 86, no. 5, pp. 2483–2499, 1987.

- [45] C. Wieman and T. W. Hänsch, “Doppler-free laser polarization spectroscopy,” *Physical Review Letters*, vol. 36, no. 20, p. 1170, 1976.
- [46] W. T. Lotshaw, D. McMorro, C. Kalpouzos, and G. A. Kenney-Wallace, “Femtosecond dynamics of the optical kerr effect in liquid nitrobenzene and chlorobenzene,” *Chemical physics letters*, vol. 136, no. 3-4, pp. 323–328, 1987.
- [47] D. N. Fittinghoff, J. L. Bowie, J. N. Sweetser, *et al.*, “Measurement of the intensity and phase of ultraweak, ultrashort laser pulses,” *Optics letters*, vol. 21, no. 12, pp. 884–886, 1996.
- [48] X. Chen, W. J. Walecki, O. Buccafusca, D. N. Fittinghoff, and A. L. Smirl, “Temporally and spectrally resolved amplitude and phase of coherent four-wave-mixing emission from gaas quantum wells,” *Physical Review B*, vol. 56, no. 15, p. 9738, 1997.
- [49] M. Takeda, H. Ina, and S. Kobayashi, “Fourier-transform method of fringe-pattern analysis for computer-based topography and interferometry,” *JosA*, vol. 72, no. 1, pp. 156–160, 1982.
- [50] R. Trebino and D. J. Kane, “Using phase retrieval to measure the intensity and phase of ultrashort pulses: Frequency-resolved optical gating,” *JOSA A*, vol. 10, no. 5, pp. 1101–1111, 1993.
- [51] P. K. Dixon and L. Wu, “Broadband digital lock-in amplifier techniques,” *Review of scientific instruments*, vol. 60, no. 10, pp. 3329–3336, 1989.
- [52] Z. Zurich Instruments, “Principles of lock-in detection,”
- [53] C. A. Werley, S. M. Teo, and K. A. Nelson, “Pulsed laser noise analysis and pump-probe signal detection with a data acquisition card,” *Review of Scientific Instruments*, vol. 82, no. 12, 2011.
- [54] N. Tsatrafyllis, I. Kominis, I. Gonoskov, and P. Tzallas, “High-order harmonics measured by the photon statistics of the infrared driving-field exiting the atomic medium,” *Nature Communications*, vol. 8, no. 1, p. 15 170, 2017.
- [55] M. F. Emde, W. P. de Boeij, M. S. Pshenichnikov, and D. A. Wiersma, “Spectral interferometry as an alternative to time-domain heterodyning,” *Optics letters*, vol. 22, no. 17, pp. 1338–1340, 1997.

- [56] D. Uhl, L. Bruder, and F. Stienkemeier, “A flexible and scalable, fully software-based lock-in amplifier for nonlinear spectroscopy,” *Review of Scientific Instruments*, vol. 92, no. 8, 2021.
- [57] J. A. Shirley, R. J. Hall, and A. C. Eckbreth, “Folded boxcars for rotational raman studies,” *Optics Letters*, vol. 5, no. 9, pp. 380–382, 1980.
- [58] S. M. Gallagher, A. W. Albrecht, J. D. Hybl, B. L. Landin, B. Rajaram, and D. M. Jonas, “Heterodyne detection of the complete electric field of femtosecond four-wave mixing signals,” *JOSA B*, vol. 15, no. 8, pp. 2338–2345, 1998.
- [59] V. Volkov, R. Schanz, and P. Hamm, “Active phase stabilization in fourier-transform two-dimensional infrared spectroscopy,” *Optics letters*, vol. 30, no. 15, pp. 2010–2012, 2005.
- [60] N. Belabas and M. Joffe, “Visible-infrared two-dimensional fourier-transform spectroscopy,” *Optics letters*, vol. 27, no. 22, pp. 2043–2045, 2002.
- [61] T. Zhang, C. N. Borca, X. Li, and S. T. Cundiff, “Optical two-dimensional fourier transform spectroscopy with active interferometric stabilization,” *Optics Express*, vol. 13, no. 19, pp. 7432–7441, 2005.
- [62] P. F. Tekavec, T. R. Dyke, and A. H. Marcus, “Wave packet interferometry and quantum state reconstruction by acousto-optic phase modulation,” *The Journal of chemical physics*, vol. 125, no. 19, 2006.
- [63] L. Bruder, M. Mudrich, and F. Stienkemeier, “Phase-modulated electronic wave packet interferometry reveals high resolution spectra of free rb atoms and rb* he molecules,” *Physical Chemistry Chemical Physics*, vol. 17, no. 37, pp. 23 877–23 885, 2015.
- [64] R. Bartels, T. Weinacht, N. Wagner, *et al.*, “Phase modulation of ultrashort light pulses using molecular rotational wave packets,” *Phys. Rev. Lett.*, vol. 88, no. 1, p. 013 903, 2001.
- [65] C. Hauri, A. Trisorio, M. Merano, G. Rey, R. B. Lopez-Martens, and G. Mourou, “Generation of high-fidelity, down-chirped sub-10fsmj pulses through filamentation for driving relativistic laser-matter interactions at 1khz,” *Applied physics letters*, vol. 89, no. 15, 2006.

- [66] B. Lavorel, P. Babilotte, G. Karras, F. Billard, E. Hertz, and O. Faucher, “Measurement of dichroism in aligned molecules,” *Phys. Rev. A*, vol. 94, no. 4, p. 043 422, 2016.
- [67] E. Neradovskaia, B. Maingot, G. Chériaux, C. Claudet, N. Forget, and A. Jullien, “Nonlinear chirped interferometry for frequency-shift measurement and χ (3) spectroscopy,” *APL Photonics*, vol. 7, no. 11, 2022.
- [68] M. A. Hershberger, A. M. Moran, and N. F. Scherer, “New insights into response functions of liquids by electric field-resolved polarization emission time measurements,” *The Journal of Physical Chemistry B*, vol. 115, no. 18, pp. 5617–5624, 2011.
- [69] X. Ren, V. Makhija, A.-T. Le, *et al.*, “Measuring the angle-dependent photoionization cross section of nitrogen using high-harmonic generation,” *Phys. Rev. A*, vol. 88, no. 4, p. 043 421, 2013.
- [70] X. Wang, A.-T. Le, Z. Zhou, H. Wei, and C. Lin, “Theory of retrieving orientation-resolved molecular information using time-domain rotational coherence spectroscopy,” *Physical Review A*, vol. 96, no. 2, p. 023 424, 2017.
- [71] V. Makhija, J. Tross, V. Kumarappan, *et al.*, “High-order harmonic field retrieval in ethylene,” in *EPJ Web of Conferences*, EDP Sciences, vol. 205, 2019, p. 02 005.
- [72] P. Sándor, A. Sissay, F. Mauger, *et al.*, “Angle dependence of strong-field single and double ionization of carbonyl sulfide,” *Phys. Rev. A*, vol. 98, no. 4, p. 043 425, 2018.
- [73] P. Sándor, A. Sissay, F. Mauger, *et al.*, “Angle-dependent strong-field ionization of halomethanes,” *The Journal of chemical physics*, vol. 151, no. 19, 2019.
- [74] S. Ramakrishna and T. Seideman, “Dissipative dynamics of laser induced nonadiabatic molecular alignment,” *The Journal of chemical physics*, vol. 124, no. 3, 2006.
- [75] I. V. Litvinyuk, K. F. Lee, P. W. Dooley, D. M. Rayner, D. M. Villeneuve, and P. B. Corkum, “Alignment-dependent strong field ionization of molecules,” *Phys. Rev. Lett.*, vol. 90, no. 23, p. 233 003, 2003.
- [76] C. Lin and X. Tong, “Dependence of tunneling ionization and harmonic generation on the structure of molecules by short intense laser pulses,” *Journal of Photochemistry and Photobiology A: Chemistry*, vol. 182, no. 3, pp. 213–219, 2006.

- [77] D. Pavii, K. F. Lee, D. M. Rayner, P. B. Corkum, and D. M. Villeneuve, “Direct measurement of the angular dependence of ionization for n 2, o 2, and co 2 in intense laser fields,” *Phys. Rev. Lett.*, vol. 98, no. 24, p. 243 001, 2007.
- [78] I. Thomann, R. Lock, V. Sharma, *et al.*, “Direct measurement of the angular dependence of the single-photon ionization of aligned n2 and co2,” *The Journal of Physical Chemistry A*, vol. 112, no. 39, pp. 9382–9386, 2008.
- [79] C. Vozzi, F. Calegari, E. Benedetti, *et al.*, “Controlling two-center interference in molecular high harmonic generation,” *Phys. Rev. Lett.*, vol. 95, no. 15, p. 153 902, 2005.
- [80] C. Vozzi, F. Calegari, E. Benedetti, *et al.*, “Probing two-centre interference in molecular high harmonic generation,” *Journal of Physics B: Atomic, Molecular and Optical Physics*, vol. 39, no. 13, S457, 2006.
- [81] S. Haessler, J. Caillat, W. Boutu, *et al.*, “Attosecond imaging of molecular electronic wavepackets,” *Nature Physics*, vol. 6, no. 3, pp. 200–206, 2010.
- [82] J. Itatani, J. Levesque, D. Zeidler, *et al.*, “Tomographic imaging of molecular orbitals,” *Nature*, vol. 432, no. 7019, pp. 867–871, 2004.
- [83] C. Vozzi, M. Negro, F. Calegari, *et al.*, “Generalized molecular orbital tomography,” *Nature Physics*, vol. 7, no. 10, pp. 822–826, 2011.
- [84] A. Srivastava, A. Herbst, M. M. Bidhendi, M. Kieker, F. Tani, and H. Fattahi, “Near-petahertz fieldoscopy of liquid,” *arXiv preprint arXiv:2310.20512*, 2023.
- [85] Z. Chang, *Fundamentals of attosecond optics*. CRC press, 2016.
- [86] P. Corkum, “Plasma perspective on strong multiphoton ionization,” *Phys. Rev. Lett.*, vol. 71, p. 1993, 1994.
- [87] R. Klas, A. Kirsche, M. Tschernajew, J. Rothhardt, and J. Limpert, “Annular beam driven high harmonic generation for high flux coherent xuv and soft x-ray radiation,” *Optics Express*, vol. 26, no. 15, pp. 19 318–19 327, 2018.
- [88] T. Gaumnitz, A. Jain, and H. J. Wörner, “Extreme-ultraviolet high-order harmonic generation from few-cycle annular beams,” *Optics Letters*, vol. 43, no. 18, pp. 4506–4509, 2018.

- [89] R. G. Livesey, *Flow of gases through tubes and orifices*, 1998.
- [90] C. Jin, X. Tang, B. Li, K. Wang, and C. Lin, “Optimal spatial separation of high-order harmonics from infrared driving lasers with an annular beam in the overdriven regime,” *Physical Review Applied*, vol. 14, no. 1, p. 014 057, 2020.
- [91] S. Matsika, “Conical intersections in molecular systems,” *Reviews in computational chemistry*, vol. 23, p. 83, 2007.
- [92] G. Herzberg, “Molecular spectra and molecular structure. vol. 3: Electronic spectra and electronic structure of polyatomic molecules,” *New York: Van Nostrand*, 1966.
- [93] G. A. Worth and L. S. Cederbaum, “Beyond born-oppenheimer: Molecular dynamics through a conical intersection,” *Annu. Rev. Phys. Chem.*, vol. 55, pp. 127–158, 2004.
- [94] K. Aidas, C. Angeli, K. L. Bak, *et al.*, “The Dalton quantum chemistry program system,” *WIREs Comput. Mol. Sci.*, vol. 4, no. 3, pp. 269–284, 2014. DOI: [10.1002/wcms.1172](https://doi.org/10.1002/wcms.1172).
- [95] A. Messiah, *Quantum mechanics*. Courier Corporation, 2014.
- [96] R. Thurston, M. M. Brister, L. Z. Tan, *et al.*, “Ultrafast dynamics of excited electronic states in nitrobenzene measured by ultrafast transient polarization spectroscopy,” *The Journal of Physical Chemistry A*, vol. 124, no. 13, pp. 2573–2579, 2020.
- [97] H. J. Wörner, J. B. Bertrand, B. Fabre, *et al.*, “Conical intersection dynamics in no2 probed by homodyne high-harmonic spectroscopy,” *Science*, vol. 334, no. 6053, pp. 208–212, 2011.
- [98] H. Timmers, Z. Li, N. Shivaram, R. Santra, O. Vendrell, and A. Sandhu, “Coherent electron hole dynamics near a conical intersection,” *Physical review letters*, vol. 113, no. 11, p. 113 003, 2014.
- [99] H. Timmers, X. Zhu, Z. Li, *et al.*, “Disentangling conical intersection and coherent molecular dynamics in methyl bromide with attosecond transient absorption spectroscopy,” *Nature communications*, vol. 10, no. 1, p. 3133, 2019.

- [100] K. F. Chang, H. Wang, S. M. Poullain, D. Prendergast, D. M. Neumark, and S. R. Leone, “Mapping wave packet bifurcation at a conical intersection in CH_3I by attosecond xuv transient absorption spectroscopy,” *The Journal of chemical physics*, vol. 154, no. 23, 2021.
- [101] O. Venot, Y. Bénilan, N. Fray, *et al.*, “Vuv-absorption cross section of carbon dioxide from 150 to 800 k and applications to warm exoplanetary atmospheres,” *Astronomy & Astrophysics*, vol. 609, A34, 2018.
- [102] P. Peng, C. Marceau, M. Hervé, P. Corkum, A. Y. Naumov, and D. Villeneuve, “Symmetry of molecular rydberg states revealed by xuv transient absorption spectroscopy,” *Nature communications*, vol. 10, no. 1, pp. 1–8, 2019.
- [103] K. Yoshino, J. Esmond, Y. Sun, W. Parkinson, K. Ito, and T. Matsui, “Absorption cross section measurements of carbon dioxide in the wavelength region 118.7–175.5 nm and the temperature dependence,” *Journal of Quantitative Spectroscopy and Radiative Transfer*, vol. 55, no. 1, pp. 53–60, 1996.
- [104] W. Parkinson, J. Rufus, and K. Yoshino, “Absolute absorption cross section measurements of CO_2 in the wavelength region 163–200 nm and the temperature dependence,” *Chemical physics*, vol. 290, no. 2-3, pp. 251–256, 2003.
- [105] S. Y. Grebenshchikov, “Communication: Multistate quantum dynamics of photodissociation of carbon dioxide between 120 nm and 160 nm,” *The Journal of chemical physics*, vol. 137, no. 2, 2012.
- [106] S. Y. Grebenshchikov, “Photodissociation of carbon dioxide in singlet valence electronic states. i. six multiply intersecting ab initio potential energy surfaces,” *The Journal of chemical physics*, vol. 138, no. 22, 2013.
- [107] S. Y. Grebenshchikov, “Photodissociation of carbon dioxide in singlet valence electronic states. ii. five state absorption spectrum and vibronic assignment,” *The Journal of chemical physics*, vol. 138, no. 22, 2013.
- [108] S. Y. Grebenshchikov, “Photochemistry of carbon dioxide from first principles: Application to photoabsorption of hot CO_2 ,” *Journal of CO_2 Utilization*, vol. 15, pp. 32–40, 2016.
- [109] S. Y. Grebenshchikov, “Infrared spectra of neutral bent carbon dioxide,” *The Journal of Physical Chemistry A*, vol. 121, no. 22, pp. 4296–4305, 2017.
- [110] W. Cao, E. R. Warrick, A. Fidler, D. M. Neumark, and S. R. Leone, “Noncollinear wave mixing of attosecond xuv and few-cycle optical laser pulses in gas-phase atoms: Toward multidimensional spectroscopy involving xuv excitations,” *Physical Review A*, vol. 94, no. 5, p. 053846, 2016.

- [111] A. P. Fidler, S. J. Camp, E. R. Warrick, *et al.*, “Nonlinear xuv signal generation probed by transient grating spectroscopy with attosecond pulses,” *Nature communications*, vol. 10, no. 1, pp. 1–8, 2019.
- [112] T. K. Allison, J. van Tilborg, T. W. Wright, M. P. Hertlein, R. W. Falcone, and A. Belkacem, “Separation of high order harmonics with fluoride windows,” *Optics express*, vol. 17, no. 11, pp. 8941–8946, 2009.
- [113] M. Williams and E. Arakawa, “Optical properties of single-crystal magnesium oxide,” *Journal of Applied Physics*, vol. 38, no. 13, pp. 5272–5276, 1967.
- [114] R. Paschotta, “Relative intensity noise,” Nov. 2007. DOI: [10.61835/xx3](https://doi.org/10.61835/xx3). [Online]. Available: https://www.rp-photonics.com/relative_intensity_noise.html.
- [115] L.-M. Koll, L. Maikowski, L. Drescher, T. Witting, and M. J. Vrakking, “Experimental control of quantum-mechanical entanglement in an attosecond pump-probe experiment,” *arXiv preprint arXiv:2108.11772*, 2021.
- [116] K. E. Dorfman, F. Schlawin, and S. Mukamel, “Nonlinear optical signals and spectroscopy with quantum light,” *Reviews of Modern Physics*, vol. 88, no. 4, p. 045008, 2016.
- [117] M. E. Peskin and D. V. Schroeder, *An Introduction To Quantum Field Theory*, First edition. CRC Press, 2018, ISBN: 0-429-98318-2.
- [118] P. G. Kwiat, K. Mattle, H. Weinfurter, A. Zeilinger, A. V. Sergienko, and Y. Shih, “New high-intensity source of polarization-entangled photon pairs,” *Physical Review Letters*, vol. 75, no. 24, p. 4337, 1995.
- [119] J.-P. W. MacLean, J. M. Donohue, and K. J. Resch, “Direct characterization of ultrafast energy-time entangled photon pairs,” *Physical Review Letters*, vol. 120, no. 5, p. 053601, 2018.
- [120] S. Sofer, E. Strizhevsky, A. Schori, K. Tamasaku, and S. Schwartz, “Quantum enhanced x-ray detection,” *Physical Review X*, vol. 9, no. 3, p. 031033, 2019.
- [121] U. A. Javid, J. Ling, J. Staffa, M. Li, Y. He, and Q. Lin, “Ultrabroadband entangled photons on a nanophotonic chip,” *Physical review letters*, vol. 127, no. 18, p. 183601, 2021.

- [122] A. T. Bondy, D. C. Morton, and G. Drake, “Two-photon decay rates in heliumlike ions: Finite-nuclear-mass effects,” *Physical Review A*, vol. 102, no. 5, p. 052 807, 2020.
- [123] M. Lipeles, R. Novick, and N. Tolk, “Direct Detection of Two-Photon Emission from the Metastable State of Singly Ionized Helium,” *Phys. Rev. Lett.*, vol. 15, no. 17, pp. 690–693, Oct. 1965.
- [124] G. W. Drake, G. Victor, and A. Dalgarno, “Two-photon decay of the singlet and triplet metastable states of helium-like ions,” *Physical Review*, vol. 180, no. 1, p. 25, 1969.
- [125] M. Prior, “Lifetime of the 2S state of He+,” *Physical Review Letters*, vol. 29, no. 10, p. 611, 1972.
- [126] P. H. Mokler and R. W. Dunford, “Two-photon decay in heavy atoms and ions,” *Physica Scripta*, vol. 69, no. 1, p. C1, 2004.
- [127] C. G. Parthey, A. Matveev, J. Alnis, *et al.*, “Improved measurement of the hydrogen 1 s–2 s transition frequency,” *Physical review letters*, vol. 107, no. 20, p. 203 001, 2011.
- [128] L. Yatsenko, T. Halfmann, B. Shore, and K. Bergmann, “Photoionization suppression by continuum coherence: Experiment and theory,” *Physical Review A*, vol. 59, no. 4, p. 2926, 1999.
- [129] L. Yatsenko, V. Romanenko, B. Shore, T. Halfmann, and K. Bergmann, “Two-photon excitation of the metastable 2 s state of hydrogen assisted by laser-induced chirped stark shifts and continuum structure,” *Physical Review A*, vol. 71, no. 3, p. 033 418, 2005.
- [130] P. L. Knight, M. Lauder, and B. J. Dalton, “Laser-induced continuum structure,” *Physics Reports*, vol. 190, no. 1, pp. 1–61, 1990.
- [131] T. Halfmann, L. Yatsenko, M. Shapiro, B. Shore, and K. Bergmann, “Population trapping and laser-induced continuum structure in helium: Experiment and theory,” *Physical Review A*, vol. 58, no. 1, R46, 1998.
- [132] Y. Wang, S. Pandey, C. H. Greene, and N. Shivaram, “Attosecond entangled photons from two-photon decay of metastable atoms: A source for attosecond experiments and beyond,” *Physical Review Research*, vol. 4, no. 3, p. L032038, 2022.

- [133] E. W. Van Stryland and D. J. Hagan, “Nonlinear absorption,” in *Encyclopedia of Optical and Photonic Engineering, Second Edition*, CRC Press, 2015, pp. 1–7.
- [134] A. C. Vutha, “A simple approach to the landau–zener formula,” *European journal of physics*, vol. 31, no. 2, p. 389, 2010.
- [135] R. S. Van Dyck, C. E. Johnson, and H. A. Shugart, “Radiative lifetime of the 2^1S_0 metastable state of helium,” *Phys. Rev. A*, vol. 4, pp. 1327–1336, 4 Oct. 1971. DOI: [10.1103/PhysRevA.4.1327](https://doi.org/10.1103/PhysRevA.4.1327). [Online]. Available: <https://link.aps.org/doi/10.1103/PhysRevA.4.1327>.
- [136] B. Blauensteiner, I. Herbauts, S. Bettelli, A. Poppe, and H. Hübner, “Photon bunching in parametric down-conversion with continuous-wave excitation,” *Physical Review A*, vol. 79, no. 6, p. 063846, 2009.
- [137] T. Gaumnitz, A. Jain, Y. Pertot, *et al.*, “Streaking of 43-attosecond soft-x-ray pulses generated by a passively cep-stable mid-infrared driver,” *Optics express*, vol. 25, no. 22, pp. 27506–27518, 2017.
- [138] J. Duris, S. Li, T. Driver, *et al.*, “Tunable isolated attosecond x-ray pulses with gigawatt peak power from a free-electron laser,” *Nature Photonics*, vol. 14, no. 1, pp. 30–36, 2020.
- [139] L. Z. Tan, *Utps, a computational spectroscopy program*, <https://gitlab.com/mf-photonphysics/utps>, 2023.

A. THEORETICAL CALCULATION OF EMITTED NONLINEAR E-FIELD

Electronic structure models of CO₂ and N₂ molecules were constructed using coupled-cluster singles and doubles (CCSD) method, with the 6-31G(d,p) Gaussian basis set, and solved using the DALTON software package [94]. These models were constructed by selecting "bright" states which have finite transition dipole moments to the ground state, and energetically low-lying states which have finite transition dipole to those bright states. All the bright states in these models have B_u symmetry. The CO₂ model consists of the ground state together with the excited state singlet molecular orbitals of following symmetries: B_{1g} (13.38 eV), B_{2g} (10.69 eV), B_{3g} (10.69 eV), B_{2u} (15.33 eV), B_{3u} (15.33 eV), two B_{1u} orbitals (9.26 and 13.14 eV), and two A_u orbitals (9.18 and 9.26 eV). The N₂ model consists of the ground state together with the excited state singlets: B_{2g} (9.74 eV), B_{3g} (9.74 eV), B_{1u} (17.07 eV), B_{2u} (14.01 eV), B_{3u} (14.01 eV). Since we do not expect significant ionization at the laser intensities used in the experiment, higher-lying ionic states were not included in the model.

The input files used to calculate all the dipole moments for CO₂ are reproduced below:

Content of the .mol file

BASIS

6-31G**

CO2 using 6-31G**

Using automatic symmetry detection

Atomtypes=2

Charge=6.0 Atoms=1

C .0000000000 .0000000000 .0000000000

Charge=8.0 Atoms=2

O_a .0000000000 .0000000000 2.1977

O_b .0000000000 .0000000000 -2.1977

Content of the .dal input file

```
**DALTON INPUT
.RUN WAVEFUNCTIONS
**INTEGRALS
.DIPLEN
**WAVE FUNCTIONS
.CC
*CC INPUT
.CCSD
.NSYM
8
*CCEXCI ! calculate excitation energies
.NCCEXCI
1 1 1 2 2 2 2 2
*CCFOP ! ground state moments/properties
.NONREL
.DIPMOM
*CCEXGR ! excited state moments/properties
.DIPOLE
*CCLRSD ! ground-excited state transition moments and OS
.DIPOLE
*CCQR2R ! ground-excited state transition moments and OS
.DIPOLE
**END OF DALTON INPUT
```

We performed theoretical calculations of the emitted signal E-field using Lindblad equation simulations in the time-domain, solving

$$\dot{\rho}(t) = -\frac{i}{\hbar}[H(t), \rho(t)] + \mathcal{L}_D \rho(t) \quad (\text{A.1})$$

with the Hamiltonian

$$H(\vec{r}, t) = \Omega + \vec{\mu} \cdot (\vec{E}_1(\vec{r}, t) + \vec{E}_2(\vec{r}, t) + \vec{E}_3(\vec{r}, t)) \quad (\text{A.2})$$

In these simulations, we use DFWM pulses $\vec{E}_1(\vec{r}, t)$, $\vec{E}_2(\vec{r}, t)$, $\vec{E}_3(\vec{r}, t)$ with frequencies, durations, intensities, chirp, and polarizations that are the same as the experiment. The alignment pump is not included in the simulations as its only purpose was to align the molecules; alignment effects were captured in the simulations by rotating the DFWM pulses in the molecular frame. Excited state energy levels Ω and transition dipole moments $\vec{\mu}$ are obtained from CCSD calculations. We included population relaxation and dephasing times of 1 ps in the Lindbladian \mathcal{L}_D , however, the results were insensitive to these values as the signal is non-zero only during the duration of pulse overlap, which is much shorter than the dephasing and relaxation times. The Lindblad equation was numerically solved using the Euler method with fixed time step of 0.1 fs, using the UTPS simulation package [139].

The result of solving equation A.1 is the time domain polarization $\vec{P}(\vec{r}, t) = \text{Tr}[\vec{\mu}\rho(\vec{r}, t)]$. To extract the third-order signal E-field, we impose phase matching conditions by selecting only wavevectors parallel to the signal propagation direction

$$\vec{P}_{\text{sig}}(t) = \int d^3r \, e^{-i\vec{k} \cdot \vec{r}} \vec{P}(\vec{r}, t) \quad (\text{A.3})$$

with $\vec{k} = \vec{k}_1 - \vec{k}_2 + \vec{k}_3$ being the signal wavevector corresponding to the phase matching conditions of equation 1.12. These calculations were repeated for 100 alignment angles of the molecules between 0° and 180°. Signal amplitude and chirp from these simulations were fit using the same methodology as for the experimental data.

B. NUMERICAL CALCULATION OF SECOND-HYPERPOLARIZABILITIES

To calculate excited-state second-hyperpolarizabilities using DALTON [94], we need to first calculate the desired excited state of the molecule. There are multiple methods of varying capability and complexity to accomplish this:

Hartree-Fock (HF)

HF is a standard method for calculating wave functions in multi-electron systems. The wave function is expressed as a Slater determinant of atomic orbitals (in some chosen basis). The interaction between electrons is handled using a mean-field approximation. But we can do better with other post-HF methods. In DALTON, we need to specify the number of doubly occupied orbitals of each symmetry at the HF level. These HF levels are then used as the starting orbitals for other post-HF methods. Sometimes the results of HF calculations can be improved by accounting for interactions using perturbation theory (Møller-Plesset).

Configuration Interaction (CI)

CI builds on top of the molecular orbitals (MOs) calculated using HF. Instead of using a single Slater determinant as in HF, configuration-interaction accounts for electron-electron correlation using a linear expansion in Slater determinants

$$|\Psi\rangle = c_0|\phi_0\rangle + \sum_{a,r} c_a^r|\phi_a^r\rangle + \sum_{a,b,r,s} c_{ab}^{rs}|\phi_{ab}^{rs}\rangle + \dots \quad (\text{B.1})$$

where $|\phi_0\rangle$ is the usual HF Slater determinant, and $|\phi_a^r\rangle$ is the Slater determinant formed by replacing orbital a in $|\phi_0\rangle$ with orbital r , and so on with double and other higher excitations. The coefficients $c_{abc\dots}^{rst\dots}$ are then found variationally. When the expansion is truncated after double excitation terms, it is denoted as 'configuration interaction singles and doubles' (CISD). The states included in the sets $[a,b,c,\dots]$ and $[r,s,t,\dots]$ are picked from a subset of accessible MOs. This subset is called the complete active space (CAS).

Table B.1. Calculated second-hyperpolarizability $\gamma_{zzzz}^{(2)}$ for the potassium atom $[1s^2 2s^2 2p^6 3s^2 3p^6 4s^1]$, for various complete active spaces (CAS). Note how the calculated values can change drastically for different CAS.

CAS	$\gamma_{zzzz}^{(2)}$
3p 4s 3d 4p	222.8764
4s	222.8764
3s 3p 4s 3d 4p	-11.7369
2p 3s 3p 4s 3d 4p	3.0449
2s 2p 3s 3p 4s 3d 4p	-0.0127

One might think that the CAS should only include the HOMO and LUMO, since the core orbitals are doubly occupied. This however is not true. In multi-electron systems, the core electrons are also correlated (among themselves and) to the valence electrons. Thus, to fully account for Fermi/Coulomb correlations, the CAS should include most of the core orbitals. The following table shows how including the core orbitals drastically changes the calculated second-hyperpolarizability $\gamma^{(2)}$ for the potassium atom $[1s^2 2s^2 2p^6 3s^2 3p^6 4s^1]$.

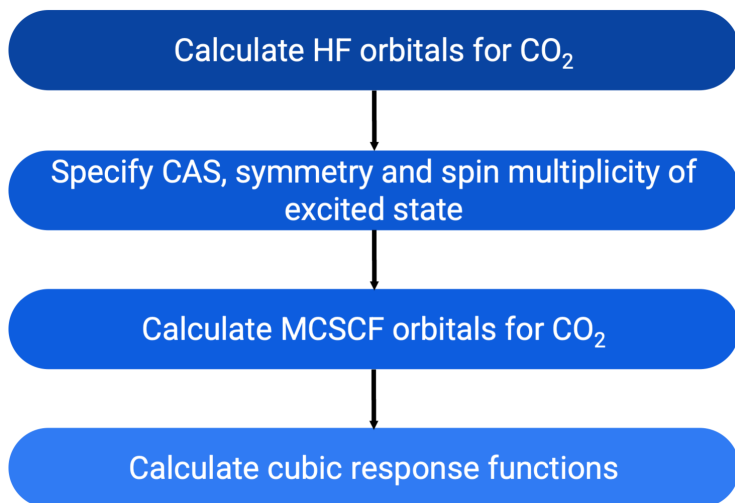


Figure B.1. Flowchart showing the order of steps for calculating excited-state properties in DALTON, using MCSCF.

Multi-Configurational Self-Consistent Field Theory (MCSCF)

MCSCF can be considered a combination between configuration interaction (where the MOs are fixed and the expansion coefficients are varied) and HartreeFock (where the MOs are varied). The orbitals and coefficients are both calculated variationally. In this appendix we will use MCSCF to calculate the second-hyperpolarizabilities of excited states of CO_2 . The progression of such a calculation is shown in figure [B.1](#).

In all these methods, we need to first specify a basis set. The various basis sets differ in the number and properties of the basis functions used. For instance, the following basis sets grow in size successively: STO-nG, 3-21G, 6-31G, 6-311G. Details about these basis functions can be found in the literature. The additional * and ** in front of a 6-31G basis indicates improved accuracy variants (by adding polarization functions). A single asterisk adds more atomic orbitals at each heavy atom, whereas two asterisks add more atomic orbitals at both heavy and light atoms.

For calculating excited-state properties, we also need to specify the symmetry and spin multiplicity of the desired state. Spin multiplicity of a given state can be found as follows:

1. One doubly-occupied orbital $\rightarrow 1$
2. One singly-occupied orbital $\rightarrow 2$
3. Two singly-occupied orbitals $\rightarrow 1$ or 3

For instance, the ground state in a molecule is usually a $^1\Sigma_g^+$ state. This state is completely symmetric and has a spin multiplicity of 1. Similarly, the state for a molecule with the configuration $(1\sigma_g)^2 \dots (1\pi_u)^1 (1\pi_g)^1$ can be any of $\Pi_u \times \Pi_g = \Sigma_u^+ + \Sigma_u^- + \Delta_u$, with multiplicity either 1 (paired e^-) or 3 (unpaired e^-). Core orbitals that are to be excluded from the CAS are denoted as *inactive* in DALTON.

Example DALTON calculations

The atomic constituents of CO_2 , and their geometric arrangement are specified in the DALTON *.mol* file.

Content of the .mol file

BASIS

6-31G*

CO2 using the 6-31G* basis

Using automatic symmetry detection

Atomtypes=2

Charge=6.0 Atoms=1

C .0000000000 .0000000000 .0000000000

Charge=8.0 Atoms=2

O_a 2.2109794066 .0000000000 .0000000000

O_b -2.2109794066 .0000000000 .0000000000

We have specified two atomic species, and their relative positions in atomic units. For this calculation we will use the 6-31G* basis. The MOs of linear CO_2 can be easily found in the literature. In DALTON, we need to specify every MO according to its symmetry. Although linear molecules like CO_2 have a $D_{\infty h}$ symmetry, DALTON can at maximum handle D_{2h} symmetry. DALTON therefore breaks the symmetry artificially, without lifting any degeneracy.

We first need to classify all orbitals according to their corresponding irreps. For instance, σ -bonds belong to A, and π -bonds belong to B. Once the molecular geometry has been specified, we need to specify the details of the calculation in the *.dal* file. The code is segmented into three blocks:

1. ****INTEGRALS:** All atomic integrals that might be used in the response calculations are numerically evaluated in this block. In our calculation, these will be the dipole length operator integrals.
2. ****WAVE FUNCTIONS:** By default, DALTON calculates all response functions for the ground state. For calculating excited-state response functions, we need to first explicitly calculate the excited-state wave functions. We do this by first doing a HF calculation, then using those orbitals as starting orbitals for MCSCF.
3. ****RESPONSE:** Here we specify the property that we wish to compute. In our case, we are calculating the third order non-linear optical response with a 800 nm laser excitation.

Let's focus on asymmetric bond stretching in (linear) CO_2 . The relevant symmetry group now is $C_{2\infty}$, which is artificially reduced to C_{2v} inside DALTON. The decomposition of irreducible representations (irreps.) of $C_{2\infty}$ into those of C_{2v} can be found in standard references on group representation theory. In DALTON, the irreps. of C_{2v} need to be listed in the following order: A_1, B_1, B_2, A_2

Content of the .dal input file

```

**DALTON INPUT           must start all input files
.RUN RESPONSE            run integrals , wave function and response
**INTEGRALS
.DIPLN                  dipole length integrals for the chosen basis
**WAVE FUNCTIONS        wave function input
.HF
.MCSCF
*SCF INPUT              HF input
.DOUBLY OCCUPIED
7 2 2 0                 A1 includes 3 1s AO, 2 2s AO, 2 sigma MO
*OPTIMIZATION
.STATE
2                        choose second (first excited) state of symmetry 1
*CONFIGURATION INPUT
.SYMMETRY
1                        symmetry of the desired state
.SPIN MULTIPLICITY
1                        multiplicity of the desired state
.INACTIVE
3 0 0 0                 A1 includes only 3 1s AO
.CAS SPACE
5 2 2 0                 irrep. ordering: A1 B1 B2 A2

```

.ELECTRONS	
16	no. of valence (2s & 2p) electrons in CO2
**RESPONSE	
*CUBIC	cubic response function calculation
.DIPLN	
.BFREQ	frequency of the 1st field
1	
0.00908	frequency in a.u.
.CFREQ	frequency of the 2nd field
1	
0.00908	
.DFREQ	frequency of the 3rd field
1	
0.00908	
**END OF DALTON INPUT	

For comparison, let us now see how the same calculation is done for linear and symmetric CO_2 in its ground state. Now, the relevant symmetry group is $D_{\infty h}$. The *.mol* file remains unchanged, but since the symmetry is now changed, we need to modify the *.dal* file. The irreps. of D_{2h} need to be listed in the following order: $A_g, B_{3u}, B_{2u}, B_{1g}, B_{1u}, B_{2g}, B_{3g}, A_u$

Note that the total number of doubly occupied orbitals is the same as in the asymmetric case.

Content of the *.dal* input file

```

**DALTON INPUT           must start all input files
.RUN RESPONSE            run integrals , wave function and response
**INTEGRALS
.DIPLN                  dipole length integrals for the chosen basis
**WAVE FUNCTIONS        wave function input
.HF
.MCSCF
*SCF INPUT              HF input
.DOUBLY OCCUPIED
5 1 1 0 2 1 1 0        irrep. ordering: Ag B3u B2u B1g B1u B2g B3g Au
*OPTIMIZATION
.STATE
1                        choose the first (ground) state of symmetry 1
*CONFIGURATION INPUT
.SYMMETRY
1                        symmetry of the desired state
.SPIN MULTIPLICITY
1                        multiplicity of the desired state
.INACTIVE
3 0 0 0 0 0 0 0        Ag includes only 3 1s AO
.CAS SPACE

```

3 2 2 0 3 1 1 0	all 16 non-core MOs included
.ELECTRONS	
16	no. of valence (2s & 2p) electrons in CO2
**RESPONSE	
*CUBIC	cubic response function calculation
.DIPLN	
.BFREQ	frequency of the 1st field
1	
0.00908	frequency in a.u.
.CFREQ	frequency of the 2nd field
1	
0.00908	
.DFREQ	frequency of the 3rd field
1	
0.00908	
**END OF DALTON INPUT	